THE UNIVERSITY OF HULL

Increasing the Capacity of an Ultrasonic Communication Systems using Variable Structure Control

being a Thesis submitted for the Degree of Doctor of Philosophy

in the University of Hull

by

Shaodong Ma, BEng

December 2011

To my grandfather

Abstract

Narrow bandwidth transducers used in existing ultrasonic (US) data communication systems are known to be devices with a high Q resonant response and low coupling to both the electrical drive and acoustic interfaces. These features limit the speed of phase change when phase modulation (PM) is used. This thesis studies the design of a Variable Structure Controller (VSC)-based transmitter and receiver with the aim of increasing the capacity of a PM-based US communications system. Simulation results are presented to demonstrate that a VSC controller can be employed in combination with US transducers to achieve the control of transducer dynamics to deliver the required transient response to allow PM symbols with a duration of three carrier periods in comparison with standard transducers. A low frequency prototype system has been constructed to demonstrate the feasibility and potential of this approach.

Acknowledgements

I would like to give my earnest thankfulness to Dr. Antony Wilkinson for his significant supports and honest advices throughout my research study. His encouragements and motivations helped me develop a strong personality and overcome challenges in adversities.

I would also like to express my heartiest gratitude to Dr. Kevin Paulson for his enthusiasm, insightful questions as well as all the expenses on the instruments.

My appreciation goes to Mr. Nicholas Riley for leading me into the research; my grateful thanks are given to Xiaoyu Sun for proof-reading and to Dr. Sabine Hünerbein and Dr. James Gilbert for their times to assess this thesis.

Last but by no means the least; my special thank is owed to my entire family and friends who has been supportive financially and morally for the last 3 years.

Table of Contents

List of Figures

List of tables

Chapter 1.

Introduction

The research works presented in this thesis investigates the feasibility of increasing the bandwidth of ultrasound (US) communication systems based on narrow band US transducers. The research on acoustic data transmission was initiated to assess the large potential benefits to be accrued from applying encoding concepts used in radio communication to the US systems. As the existing electromagnetic spectrum management is strictly regulated, the allocation of radio spectrum for wireless communications becomes more restricted as increasing numbers of systems generate interference. Furthermore, radio systems are not appropriate in some environments. Improper use of radio systems in the inflammable atmosphere of petro-chemical plants [1], or mines leads to serious accidents. Radio interference in hospitals can lead to the malfunction of life-critical systems. The US spectrum is minimally regulated and is an alternative to wireless systems for data or voice transfer over short distances.

A small number of US systems utilise the encoding and modulation schemes common in radio systems but only achieve limited data transmission rates of a few kilo bits per second (kbps). The primary constraint identified in Section 3.3 is the narrow bandwidth of the US transducers used in existing communication systems. This limits the speed that the transducers can respond to the modulated drive signal, for example phase reversals imposed on the carrier wave. This problem is associated with the electro-mechanical inertia of the transducers, which leads to a delayed response to an instantaneous phase switching. This occurs at both transmitting and receiving transducers and constrains the transmitted pulse width.

An US communication system with increased capacity could be achieved if the transient response time of the transducer could be shortened. Generating a faster phase transition requires higher bandwidth from the transducers. In this project, the possibility of broadening the bandwidth will be explored using Variable Structure Control dynamical feedback compensation.

1.1. Aims and Methodology

The principal objective of this research is to design and evaluate a transient control system to compensate US transmitting and receiving transducer dynamic responses. To apply a compensatory drive signal to the transducer, it is necessary to obtain some knowledge about transducer dynamic characteristics.

- Experimental determination of the transducer dynamic will be conducted by stimulating a transmitting transducer with pulsed drive and observing the received transducer electrical output waveform.

- Dynamic system models will be selected to simulate the transducer system responses. The comparison between simulated and measured transducer response will be used to understand the impact of the transducer resonance characteristics.

A non-linear switching control mechanism known as Variable Structure Control (VSC) will be applied to adaptively compensate the US transducer responses. The construction of experiments can be split into two phases:

- The transient compensation system based on the transducer models will be first simulated in a computer programme to validate the feasibility of the control approach.

- A physical VSC transient compensation prototype will be implemented according to the system structure used in simulation, and used to examine the practicalities of the transient compensation.

1.2. Thesis Organisation

The following chapters document the procedures to analyse and design a VSC-based US transient compensator except for the Chapters 2, 3 and 7.

Chapter 2 provides a thorough literature survey of the relevant research and applications of US (acoustic) air-coupled systems using narrow band resonant transducers. The survey indicates that little effort has been made on reducing the transducer transient time and the potential to

improve the capacity of the surveyed systems if the transient can be attenuated quickly.

Chapter 3 presents a preliminary investigation regarding the capability of a phase modulation (PM)-based US transducer system to follow an anti-phase stimulus. The investigation begins with a practical measurement to characterise the transducers. An equivalent circuit model of the transducer is chosen and parameters are identified from experimental measurements. Furthermore, the information capacity of the constructed system was also examined through transmitting and decoding of a known pulse sequence.

Chapter 4 presents the design of a discrete VSC transient reducer for the US transmitting transducer. The early sections in this chapter describe the control system structure which contains two proportional feedback control loops. The *Root-locus* technique is used to assess each loop to ensure that combination of these two feedback system dynamics will produce the anticipated feedback results. The system performance is evaluated and compared with an uncompensated version to demonstrate the effectiveness of the VSC approach.

The behaviour of a VSC controlled receiver, when it is configured to receive a similar acoustic resonance as the waveform produced by the VSC transmitter introduced in Chapter 4, is analysed and simulated in Chapter 5. Detailed transfer function and *root-locus* analyses provide a theoretical verification of the compensated receiving system. Effects of modifying the controlled transient speed by tuning critical parameters are demonstrated.

Chapter 6 presents a physically realised VSC prototype system used to investigate the practicalities for system implementation.

Chapter 7 concludes the thesis and suggests future work and potential application fields. An estimate is made of the maximum information capacity achievable from a VSC-based US communication system.

Finally the thesis ends with concluding remarks which summarise the contributions made by this project to new knowledge.

Chapter 2.

Literature Review

This chapter will review US technologies with respect to the ultrasonic (US) transducer system structure and applications.

2.1. The Fundamentals of an Acoustic Transducer

The transducer is the means by which electrical energy is converted to and from kinetic energy [2]. The transmitting transducer converts electrical power into a movement of the propagation medium. The receiving transducer absorbs energy from the movement of the medium and converts it back to electrical energy, often simply reversing the process in the transmitter.

Acoustic transducers can be made to resonate around audio and US frequencies. A *piezoelectric* transducer [3], is an electro-acoustic device that employs a *piezoelectric* material, such as a crystal or ceramic, which is deformed by the application of an electrical stimulus. The *piezoelectric* effect is reversible [4]. Applying an electrical drive signal will stimulate the transducer to vibrate the surrounding medium and propagate the kinetic energy in the form of sound wave. Transducers can be made for applications in a variety of propagation media. Each medium has a different acoustic characteristic impedance that will modify the propagation of a acoustic or US wave. Material properties such as density, Young's modulus and elasticity, modify the sound speed, energy attenuation and damping of the kinetic movement.

An alternative electro-mechanical coupling mechanism uses the *magnetostrictive* properties of some materials. *Magnetostrictive* transducers [5] are composed primarily of ferromagnetic materials and can be differentiated from *piezoelectric* transducers through the mechanism used to generate US energy. The *Magnetostrictive* transducer deforms as the ferromagnetic material is magnetised.

To produce significant coupling between electrical and acoustic signals, oscillations should be close to the resonant frequency of the transducer. The resonant frequency is determined by the

geometry, material and electrical properties of the transducer and the medium in which it is immersed. Transducers are designed to resonate at prescribed frequencies for their target propagation medium. These media are typically either air or a fluid such as water.

This research will focus on the *piezoelectric* transducer designed to produce acoustic US waves in air. The following section will consider the applications of such transducers.

2.2. US Communication Systems

Interest in ultrasonic (US) techniques for communication has recently grown due to developments in digital encoding of communications and the advent of readily available, high performance digital signal processing. This approach has been considered as an alternative to wireless techniques to exchange data or voice messages over a short distance, around 10 to 20 metres, for indoor environments [6]. Indoor data communications using ultrasound has been demonstrated and shown to convey information with limited data rates, typically around 1 kbps [6-7]. Previous research has demonstrated that it is possible to use an air-coupled transducer with a centre frequency below 100 kHz. Conventional US systems are able to transmit an amplitude-modulated US wave with a carrier frequency in the range of 25 to 100 kHz [8]; this was used for television remote control [9-11]. Broadband transducers using thin film (polymer membrane) [12], electromechanical film (EMFi) [13] and micro-machined transducer [14], with a frequency range from 100 kHz to 1 MHz, and a 500 kHz bandwidth are also used in the applications where short pulse width and high resolution are required [8], over shorter paths. All these three types of transducers are similar in their constructions in that an electric field is applied across them through contact electrodes. These electrodes by their nature form a capacitive electrical coupling to the transducer.

2.2.1. Improving US Communication System Capacity using Wide Band Transducer

Li *et al.* [8] demonstrated US communication in the air for digital data over a few metres. Modulation is based on binary encoding and uses a polymer membrane transducer with the central frequency of 250 kHz with an approximate useable bandwidth of 200 kHz [8]. Li also investigated the applicability of quadrature modulation principle on micro-machined US

transducers centralised around 350 kHz with wider band width [15]. Currently this technology is regarded as impractical for general use due to its low energy electromechanical conversion efficiency. Experiments in [15] demonstrated that a 200 V peak-to-peak electrical stimulus merely results in a received signal with magnitude of 5 mV over 1.2 metres.

Li's experiment identified the following problems related to the US phase modulation system. It was found that multipath interference caused by a reflected path will shift the received Binary Phase Shift Keying (BPSK) signal phase. To deal with reflected paths, Li suggests solutions such as time-gating [16] can be applied. Li conducted frequency sweep tests which indicated that to achieve BPSK transmission, at least 20 kHz bandwidth is required as well as a coherent carrier reference. Also, the phase transitions at symbol boundaries require much more bandwidth than smooth transitions. Li also found that the demodulation process for BPSK was quite delicate, because a strictly synchronised reference carrier is needed for coherent demodulation. This may involve complex and expensive circuitry to track and lock onto the carrier wave.

2.3. Distance Measurement

The same principles that are used for an US communication system can be modified to achieve distance measurement. The acoustic sounder works in either pulse-echo or continuous wave (CW) mode. The transmitting transducer, excited by a mono-pulse or pulse sequence, emits an acoustic signal. A receiving transducer collects the reflected acoustic energy [17]. The travel time between the emission and reception of the sound, combined with knowledge of the phase velocity in the medium, is used to estimate the distance to the remote reflector. Systems based on this measurement principle have been developed for gas flow measurement [18], automotive safety [19], tank level monitoring [20], Earth observation [21] and mobile robot control [22].

2.3.1. Improving US Ranging Systems by Sensory Compensation

Microprocessor-based acoustic range measurement systems are capable of compensation to minimise the uncertainties in the measurement process. Carallo *et al*. [19] evaluated US sensors applied in a vehicular suspension system to measure the distance between the ground and vehicle body. Two environmental factors dominate range uncertainty in this application: variation in

phase velocity and propagation path distortion due to movement of the vehicle. A temperature variation in the range of 0 to 40 ºC leads to an average uncertainty of ±1 mm for a measurement range of 0.3 m above ground. [19].

2.3.2. Correlation-based Methods

To improve system performance, more complex signal processing techniques using continuous (or carrier) wave (CW) techniques have been applied to US ranging. CW systems can broadcast more power without the distortion potentially caused by large amplitudes. Marioli *et al.* [23] investigated digital algorithms based on cross-correlation to determine the time-of-flight (ToF). Although measurement based on the continuous wave approach may achieve better range estimation performance, it requires increased hardware complexity [23]. Therefore, the following two improvements were made to strengthen the capacity of the existing system: The threshold used to identify the presence of US energy becomes variable to increase resolution where echoed signals encounter serious attenuation. Secondly, the received echo was discretised and processed within a digital signal processor to reduce hardware complexity and to compute cross-correlations between transmitted and returned signals.

Cross-correlation or matched filter-based ToF measurement proposed by Eriksson *et al*. [24] was designed to obtain an optimised estimate of the reflected US pulse envelope waveform without shape distortion. However, according to maximum likelihood criteria, the optimal estimate can only be achieved in the presence of additive, white Gaussian noise with zero mean [24].

In automotive applications, there are many potential sources of interference from neighbouring acoustic distance measurement systems, [25]. For example, an US proximity sensor resonating in proximity to a neighbouring acoustic distance measurement system may potentially interfere with its ranging. This jamming signal is difficult to distinguish from its own without the transmissions being encoded. In addition, the echoed US pulses for ranging from other vehicles are regarded as undistinguishable interference because they are resonant at the same frequency. Horsky *et al.* [25] offers a possible solution to these problems, where the transducer is excited with a pulse modulated electrical stimulus. The encoded signal follows a chosen modulation scheme that is

used to distinguish it from interfering signals. The detected echo with distinct coding pattern will be demodulated and then correlated with the stimulus that was recorded before emission. Signal strength against noise and interference will be maximised as a result of the correlation between an encoded reflection and matched drive signal pattern. The pattern matching between the received echo and the drive signal permits not only immunity to ambient interference, but a more accurate range measurement [25].

2.3.3. Kalman Filtering-based Pulse Identification

To avoid shape distortion, Angrisani *et al.* [26-28] incorporated the use of a Discrete Extended Kalman Filter (DEKF) to estimate the shape of the reflected US pulse envelope. The signal phase becomes non-periodic as its magnitude attenuates with time due to transducer inertia. This kind of uncertainty will cause phase-dependent ranging system malfunctions. The approach adopted aims to obtain an approximate envelope for the US pulse which is contaminated by noise. Thus, the range calculation is based on a reconstructed pulse shape derived from the transmitted signal and can offer range estimates independent of these problems.

2.3.4. Inertia Delay Compensation

Wang *et al*. [29] considered the inertia delay error in US ranging systems caused by the US transducer and designed a novel self-interference driver. This driver uses the measured transducer transient response. An amplitude and phase modulated drive signal is distorted to compensate for the under-damped resonance response of the transducer.

2.3.5. Phase Shift Method

Time delay estimation is not the only approach to achieve remote ranging. US range measurement is also achievable through measuring the phase shift of a travelling US signal [30]. The operating principle may be stated as follows: a continuous sinusoidal wave around the resonant frequency is selected to excite the US transducer. The stimulus is also stored digitally and used in comparison with the received echo. The range information can be deduced from the linear relationship between measured phase shift and the distance of wave propagation. However, the measurement

range is limited by the wavelength ambiguities in ranging, although range changes can be tracked for greater ranges. For a typical 40 kHz US air system, the theoretical distance that the proposed method can unambiguously determine is 4.25 mm [31]. Other researchers [32] explored a combined ToF and phase-shift algorithm. ToF of the travelling wave is approximated using cross-correlation and the carrier phase is compared to refine the estimated ToF information. This method can be extended to more applications if multiple frequencies are used in order to improve accuracy and to expand the range limit. Huang *et al.* [31] provided a solution using Binary Frequency Shift Keyed (BFSK) signals so that ToF could be estimated using both frequencies. Experimental results illustrated an accuracy enhancement to ±0.05mm over a range of 6 m could be obtained by measuring the phases of two frequencies [31].

2.4. US Indoor Localisation System

Localisation systems are applications that estimate the location of equipment and people within an area covered by a sensor network. The approach used is dependent upon the required specification for the particular application [33]. US localisation systems are usually deployed in indoor environments and aim to provide physical location estimation. Location-based services supported with data from US localisation systems are seen as a way of adding value to communication systems [34]. A study of lost luggage in airport systems, decomposed Location-based Systems into three main elements: fixed equipment, mobile handsets and a dynamic network that should have the following features [35]:

- Location-aware system needs to dynamically acquire position information to some predefined precision.
- It should be capable of tracking many items and provide location information selectively to a number of users [35].

A location-aware system would solve many problems in a wide range of application scenarios. Among those scenarios, the one that presents one of the largest challenges is in the medical environment. A brief report showed a laptop theft in Nottinghamshire hospital. The stolen laptop contains data on 11,000 children between the ages of eight months and eight years old [36]. An

American press release reported that the theft of valuable high-tech facilities in Pennsylvanian hospitals was a serious issue with over $USD 200,000 worth of equipment stolen within a week [37]. Often professional thieves pass themselves off as hospital workers to steal medical apparatus [37]. Furthermore, US systems have an advantage over radio systems which may cause interference with life-critical electronic systems in a hospital.

Airports would also benefit from asset localisation services. A Chinese study found that 30,000,000 pieces of baggage are lost annually [38]. Although systems are in place for the automatic identification and handling of luggage, usually via RFID tagging or optical barcodes, these systems could be expanded to yield the location of a specific item of luggage.

Hospitals and airports are two examples of complex environments where asset tracking and localisation can prevent theft; greatly improve the management of assets, and ultimately save money and lives.

2.4.1. Challenges in Location Determination

As introduced previously, it is not unusual for hospital staff to spend large amounts of time searching for equipment [34, 39]. It is also common for this to cause financial problems when assets are stolen [34, 39]. Assets are often idle and cannot be located when needed [34, 40]. Location-based services (LBS) in hospital management systems are critically important to the success of many health interventions [39]. However, there are serious technological hurdles to the development of systems to localise and track hospital equipment due to the topological complexity of a hospital environment and compatibility problems with the wide range of medical equipment present. For systems based on the propagation of electromagnetic or acoustic waves, hospitals are a highly irregular environment with a large number of reflecting, refracting and diffracting surfaces with little line-of-sight (LOS). Multiple propagation paths lead to severe time delay and delay spread causing low data rates and faulty position detection [41].

LOS propagation in free space is the simplest possible communication process in both outdoor and indoor environments [42]. However in practical situations it is common for many reflected paths to contribute to the received signal. Medical devices, people and various building structures

are obstacles that block the LOS link between transmission and reception (more than 50% area of Fresnel zone is shadowed [43]). The challenges that non-line-of-sight (NLOS) transmission faces are weakened signal amplitude and periodicity as well as scattering caused by multiple paths [44]. However, it is recorded that iterative measurements or equalisation is capable of reducing the effects of multiple paths [45].

Many research papers report that localisation systems relying on various wireless ranging approaches have been studied and implemented in the real application scenarios [46-51]. These systems can be categorised depending on whether they are based on ToF or angle of arrival (AoA). Acoustic systems using these two techniques will be introduced in the following section.

2.4.2. Acoustic Techniques based on Arrival Time

The range information derived using *time delay* techniques can be used directly to triangulate target positions [52]. However, this is based on three assumptions. One is that the positions of reference units are known. The second is that the transponder must simultaneously interact with at least three reference ranging units at the same time. Thirdly, LOS must exist between the mobile unit and the three reference units. The calculation of *time delay* or ToF requires transponder and reader synchronisation. A possible solution is to measure the difference in arrival time between two different types of signal (for instance acoustic and electromagnetic); this has been used to achieve ToF estimation [53]. A known *time delay* is required between the triggering of the radio and acoustic sounding systems. Due to the different phase velocity, the radio signal arrives earlier than acoustic signal and will activate the range measurement devices and enable their internal timers. Once the pulsed acoustic signal is received the ranger will cease timing. The ToF difference is converted into a path length. If more than three ranges are available, room coverage in 3 dimensions is possible. For time difference of arrival (TDOA) systems using ultrasound, the range is limited to between 10 to 30 metres, depending upon the frequency, due to considerable atmosphere absorption of the sound energy [54]. The requirement of LOS paths further constrains the system ranging performance [41].

Massachusetts Institute of Technology (MIT) implemented a system known as *Cricket*, using

concurrent radio and US signal transmission [55]. Empirical testing showed that the indoor localisation granularity of the *Cricket* system was bounded by 4×4 feet cell. (approximately 1.486 m^2) [56]. Other systems such as *Active Bat* [57] and *Dolphin* [58] have been designed and implemented based on similar principles.

2.4.3. Acoustic Techniques based on Arrival Angle

An alternative method of obtaining target position is by the use of AOA-based systems [59]. This method uses a transducer array that measures the propagation direction of the incident signal. This is estimated using the difference in arrival times, or phases, at each transducer in the receiving array. The approach can be thought of as the inverse of beam-forming [59]. Some US systems have managed to implement triangulation using measured angular data. A modified version of the *Cricket* system attempts to estimate both the arrival orientation and time of the received signals [60].

2.4.4. Limitations of AOA Method caused by Low Bandwidth

Tong *et al*. [61] describe how general purpose 40 kHz US transducers with a bandwidth of 3 kHz can be used to automatically guide a material transportation vehicle to achieve precision docking, based on triangulation. Tong claims that low bandwidth US transducers only offer limited ranging accuracy. This feature will seriously lower the capacity of an angular measurement-based positioning system. Correlation or direct de-convolution based US *time delay* rangers are also impacted by the resonant property of the transducer. To resolve the problems caused by transducer band-limitation, Tong suggests cascading a filter with the complementary transducer transfer function and has shown that this can be an effective solution to obtain a compensated but time-delayed response, with a narrow pulse width in the time domain. Iterative adaptation algorithms are chosen to tune the weights of the complementary filter (a finite impulse response filter), so that the filtered output can converge to the required signal. After training, the acquired US output will be de-convolved to recover the expected (rectangular) pulse shape. Measured results suggest that a resolution of an order of ± 3 mm resolution and a bearing resolution of 6 degrees bearing can be achieved.

An indoor environment contaminated by acoustic noise significantly degrades the performance of a location system with narrow band US transducers. Hazas *et al.* [62] applied and evaluated a broadband thin film transducer with a central frequency of 50 kHz used in an existing *Dolphin* system. The selected transducer was a piezo-film and was measured to have 30 kHz bandwidth in a range from 1m to 5.76m [62]. It was reported that this piezo-film transducer was designed for proximity detection of around 40 cm [62]. In order to reach sufficient signal coverage for indoor localisation, the driver module in the *Dolphin* system was replaced with a customised power amplifier. The corresponding receiver front-end was re-configured to match the transducer output impedance and to enhance the received signal level. Experimental tests illustrated that the frequency spectrum of the 50 kHz piezo-film transducer were spread up to 20 kHz by employing Gold code and Binary Phase Shift Keying (BPSK) [63]. However, the power spectral density magnitude was markedly decreased. The localisation experiments also demonstrate an enhanced capacity in the presence of noise and simultaneous multiple signal transmissions.

Hashizume *et al.* [64-65] argue the installation of stationary sounders as an issue that restricts the way to deploy the static US distance sensors. A system prototype based on the described principle was physically implemented to validate the idea of integrating TOA and AOA using single receiver [64].

2.4.5. Received Signal Strength (RSS) based US Location System

The attenuation over the propagation path, estimated from knowledge of the transmission power and RSS, may be used to estimate the range. This method is commonly used for the coarse estimation of the location of a tagged object in indoor areas [66]. If multiple receivers are used, the overlap of range estimates from each receiver is indicative of the transmitting sensor location. Although the RSS method is easy and low-cost, its performance is limited by many factors. For example, echo and reverberation in indoor environments could overwhelm the original transmitted signal causing faulty location estimates. The repeatability of output power and receiver sensitivity has a significant impact on the received signal level. Moreover, a RSS positioning system does not measure absolute position. Therefore, it has to rely on a room map to fit with the geographic position [67]. Some authors have attempted to develop estimation

algorithms to achieve a fine-grid localisation by combining RSS with other positioning techniques [68].

2.5. Sonic Detection and Ranging (SODAR)

The acoustic equivalent to a radar is known as a sodar. Vertical pointing sodars are used to measure spatial-temporal fluctuations of atmospheric dynamics i.e. wind profiler and equipment used to detect layer boundaries in atmosphere, [69-72]. Sodars use the same operating principles as radars and can operate in either pulse-echo or CW mode.

Turbulence in the atmosphere causes mixing of air with different characteristic impedance due to temperature or humidity differences. Boundaries between these air masses reflect acoustic waves. Using this phenomena, sodars can be used to image natural turbulence [70, 73], and that caused by manmade structures e.g. airplanes [74-75] and wind farms. Typical wind sounders operate at 1 to 5 kHz and have ranges up to several kilometres. The use of higher frequencies reduces the risk of hearing damage but also reduces the range due to acoustic energy absorption by the atmosphere. These frequencies allow sodars to measure rain parameters such as rain intensity [76-77] and drop size distributions [78].

2.5.1. Applications of Radio Techniques in SODAR

Much of the technology that has been developed for radio systems can be applied to sodars. Increasingly, sodar systems broadcast coded CW signals rather than pulses. These systems yielded higher signal-to-noise ratio (SNR) after processing due to coding gain. They also avoid the non-linearities associated with high amplitude pulses, and the risk of hearing impairment [79]. Often bi-static systems are used i.e. separate transmitter and receiver, to maximise the acoustic isolation between transmitted and reflected signal. Increasingly, phased arrays of transducers are used to steer acoustic beams without physically moving the sodar system.

Variation in acoustic phase velocity leads to range errors in sodar systems. Where temperature, pressure and humidity are measured on the ground, this information can be used to partially compensate for this systematic error. The range and signal level resolution are limited by the

transient response of the transducers. Increasing the decay rate of the transient response allows shorter pulses to be broadcast, and hence shorter spatial averaging intervals in the range dimension. Alternatively, CW systems can broadcast longer codes over the same interval leading to higher coding gain, and hence better SNR, with the same temporal resolution.

2.6. Summary

Air-coupled US transducer systems currently utilise narrow bandwidths around the resonant frequency, as the electro-mechanical inertia within the transducers leads to transients with long decay times. This narrow bandwidth limits the capacity of US communications system, the spatial resolution of localisation and ranging systems, and the parameter resolution of sodar systems. The development of a feedback control system that effectively increases the transient decay rate has immediate application in improving the performance of all these US systems. The ambition of this research will impact most readily on a US range measurement system. Subsequent chapters will address the development of such a control system.

Chapter 3.

Information Capacity of an Ultrasonic Transducer System

As noted in Chapter 2, the challenging problem identified was that of the generation of an acoustic signal with rapid transition between symbols. This requires a broad bandwidth transducer to achieve the rapid phase transitions required for phase encoding such as Binary Phase Shift Keying (BPSK). However, narrow bandwidth ultrasonic (US) transducers are more common and cheaply available. Consequently, the present US applications that employ them are constrained in spatial resolution and modulation rate. This chapter aims to explore the limitations of a phase modulation-based US system using frequency selective US transducers.

Section 3.1 studies the transducer dynamical characteristics through a pulse response experiment. Lumped-parametric circuit models are selected to simulate the transducer output responses.

Section 3.2 describes the numerical simulation of transmitting and receiving subsystems using the transducer models determined in Section 3.1. The simulations are modified to demonstrate the encoding and decoding of digital information.

A trial platform, designed to match the architecture of the simulated US system, was physically implemented. Experimental results are provided to compare the information capacity of the real system with that of the simulations.

The trial platform that was built and simulated was a point-to-point communication system. Before formulating the experiment, it was necessary to make the following two assumptions:

- For the trial platform, the distance between transmitting and receiving transducers was small. This ensured propagation loss, multipath and scattering effects had minimal impact on the experiments.

- The simulations assumed that the data transmission was through a single direct path. An attenuation factor of 0.2 is set to represent channel loss.

3.1. US Transducer Pulse Response

The following experiments were conducted with the intention of investigating the fundamental limitations caused by the transducer resonant properties.

Figure 3-1 references a conceptual diagram of the devices under test. A pair of commercial US transducers was configured to emit and receive US resonant signals at 40 kHz. The transmitting transducer is stimulated by a pulsed signal, repeating at a rate of 500 Hz as shown in figure 3-2 a). Figure 3-2 b) is the measured response, at the receiving transducer electrical output, after amplification recorded using an oscilloscope. It can be observed that the measurement taken at the receiver output produces a delayed, band limited, response. The transient response to the electrical stimulation decays very slowly and is still visible when the next pulse arrives.

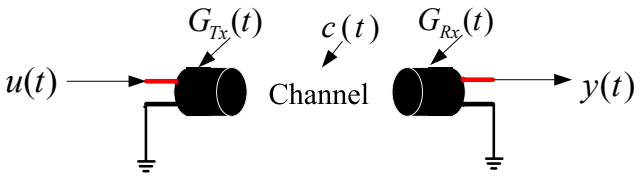

Figure 3-1: Block diagram of a simple transducer system

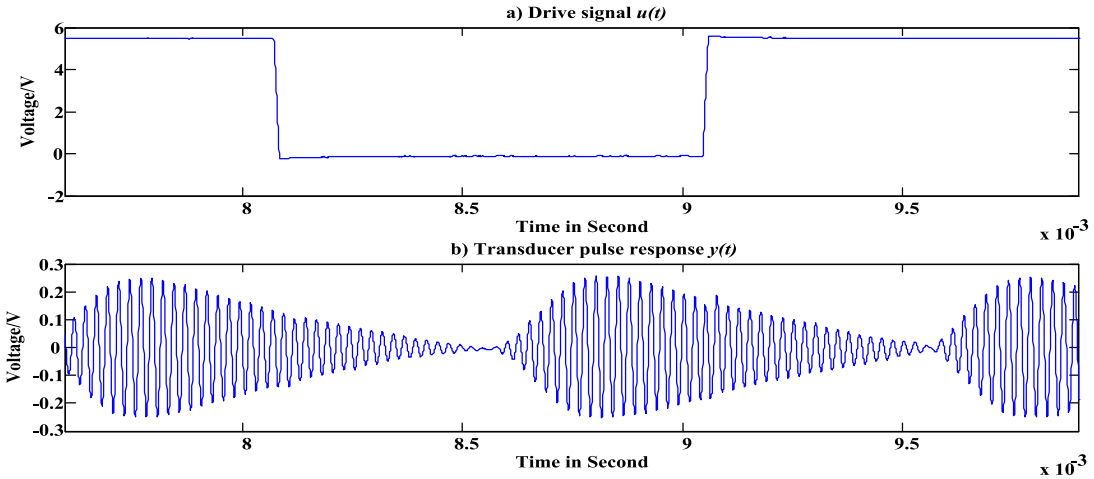

Figure 3-2: Measured transducer system response to a 500 Hz pulse drive signal

3.1.1. Mechanical Interpretation

The measured output response presents an electrical waveform that is associated with the mechanical resonance of both transducers [80]. Therefore, it is necessary to understand the

mechanical properties to interpret transducer dynamical behaviour. A mechanical mass-spring-damper is applicable to model the dynamical vibration process. The behaviour of the mechanical system can be modelled by a linear constant-coefficient differential equation (3.1) [81]:

$$\frac{\mathrm{d}^2 y_m(t)}{\mathrm{d}t^2} + 2\zeta\omega_o \frac{\mathrm{d}y_m(t)}{\mathrm{d}t} + {\omega_o}^2 y_m(t) = {\omega_o}^2 u_m(t). \tag{3.1}$$

For a mechanical vibrating system, (3.1) can be specified as:

$$m\frac{\mathrm{d}^2 y_m(t)}{\mathrm{d}t^2} = u_m(t) - k y_m(t) - b\frac{\mathrm{d}y_m(t)}{\mathrm{d}t}. \tag{3.2}$$

Where, *m*, *k* and *b* are denoted as *mass*, *spring constant* and *damping coefficient* respectively. Rearranging (3.2), the expression above becomes a similar form to (3.1)

$$\frac{\mathrm{d}^2 y_m(t)}{\mathrm{d}t^2} + \left(\frac{b}{m}\right)\frac{\mathrm{d}y_m(t)}{\mathrm{d}t} + \left(\frac{k}{m}\right) y_m(t) = \left(\frac{1}{m}\right) u_m(t). \tag{3.3}$$

Define the *un-damped natural frequency*, ω_o, and the *damping ratio (or factor),* ζ, as:

$$\omega_o = \sqrt{\frac{k}{m}}. \qquad\qquad \zeta = \frac{b}{2\sqrt{km}}. \tag{3.4,3.5}$$

Equation (3.3) can be transformed into the frequency domain by Laplace transform. Replacing physical parameters by ω_o and ζ yields a transfer function for the mechanical resonant system, (3.6):

$$\mathrm{G_m(s)} = \frac{{\omega_o}^2}{s^2 + 2\zeta\omega_o s + {\omega_o}^2}. \tag{3.6}$$

The system transfer function, (3.6), has a pair of complex conjugate poles or two real poles that can be configured to produce different system dynamics. An under-damped system dynamic occurs if the conjugate poles are in the stable region of Laplace plane, that is the poles have negative real components. Poles with a positive real component are unstable. The damping factor is related to the ratio of real and imaginary parts of the poles. Critically- or over-damped dynamics correspond to system pole configurations that only have real parts. The damping factor and the resonant frequency can be tuned through (3.4) and (3.5), which allows the system to resonate at specific frequency with a chosen level of damping.

3.1.2. Impedance Analogy

A analogy between mechanical, electrical and acoustic systems have been established for the purpose of understanding the behaviours of electro-mechanical and electro-acoustic systems [82]. [83] introduces the impedance analogy between acoustic and mechanical systems. According to [84], the mechanical-acoustic differential equation can also describe an electronic resonant circuit. The active elements of the mechanical and acoustic systems have corresponding analogous impedances in an electronic resonant network as demonstrated in figure 3-4. (3.7) is the transfer function of the electronic resonant circuit where Vsd is the applied voltage input and Vc(s) is the measured output. Table 3-1 summarises the typical impedance analogies between these three sorts of systems.

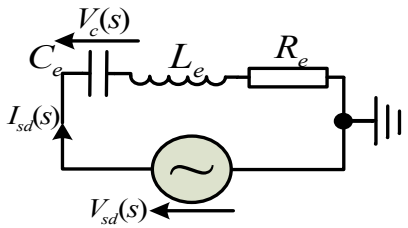

Figure 3-3: Electronic resonant circuit network

$$G_e(s) = \frac{{\omega_o}^2}{s^2 + (\omega_o/\zeta)s + {\omega_o}^2}. \tag{3.7}$$

$$\omega_o = \frac{1}{\sqrt{L_e C_e}}. \qquad \zeta = \frac{R_e}{2}\sqrt{\frac{L_e}{C_e}}. \tag{3.8,3.9}$$

An electronic analogy to an acoustic device has the advantage that voltages are available for measurement in places where there is no analogous point in the transducer. Secondly, the characteristics of a real transducer can be simulated and analysed in a computer program. Furthermore, a circuit model is physically realisable.

Electrical analogy	Mechanical analogy	Acoustic quantities
Voltage/V	Force/F	Sound pressure/p
Current/I	Velocity/(m/s)	Volume current/U
Resistance/R_e	Resistance/R_M	Resistance/R_A
Capacitance/C_e	Compliance/C_M	Capacitance/C_A
Inductance/L_e	Mass/M_M	Inertance/M_A

Table 3-1: Summary of analogies in three different systems [85]

3.1.3. *Butterworth-Van Dyke* Transducer Model

Based on the dynamic analogy introduced in Subsection 3.1.2, an electronic lumped-parameter circuit model was chosen for this study. US transducers can be modelled using a lumped-parameter model, figure 3-3, known as a *Butterworth Van-Dyke* (BVD) transducer model [86-87] and it constitutes two branches which are:

Electrical Branch:

Electrical or *static* branch contains the capacitive element modelling the electrode between *piezoelectric* resonators.

Acoustic Branch:

Acoustic or *motional* branch is the electric analogy to acoustic vibrator described by a series resonant circuit.

Table 3-2 lists the values of the equivalent circuit lumped parameters selected from transducer data sheet [88] used for later simulations.

Symbol[1]	Description	Values
C_p	Electrical Capacitance	2100 pF
L_s	Dynamic Inductance ($\propto$mass)	120 mH
C_s	Dynamic Capacitance ($\propto$1/stiffness)	130 pF
R_s	Dynamic Resistance	600 Ω
R_d	Output Resistance	600 Ω
R_{m4}	Driver Output Impedance	100 Ω

Table 3-2: Parameter definitions of BVD transducer model [88]

From the circuit network shown in figure 3-4 a), a transfer function can be derived using the voltage across the parallel capacitor C_p and voltage on the dissipative resistor R_d which is the acoustic output stage. For the receiver model, an acoustic input can be modelled as a current

[1] The subscripts, *p*, *s* and *d*, used in table 3-2 mean parallel, serial and dissipative respectively. The subscript, *m*, used in the resistive components means measurement, i.e. R_{m4} means measurement resistor 4.

input, i_{sa}, induced in the acoustic branch in parallel with its input impedance R_d. The corresponding output, V_{Rm3}, is the voltage across the load resistor in parallel with capacitor C_p. In practical US transmitting systems, the output impedance of an US driver can never be zero. A serial resistor R_{m4} is placed on the top of transducer model representing driver output impedance. The Laplace transformation of the model transfer functions, $G_{Tx}(s)$ and $G_{Rx}(s)$, can be written as in (3.10) and (3.11) (See 9.1.1. and 9.1.2. for detailed transfer function derivations).

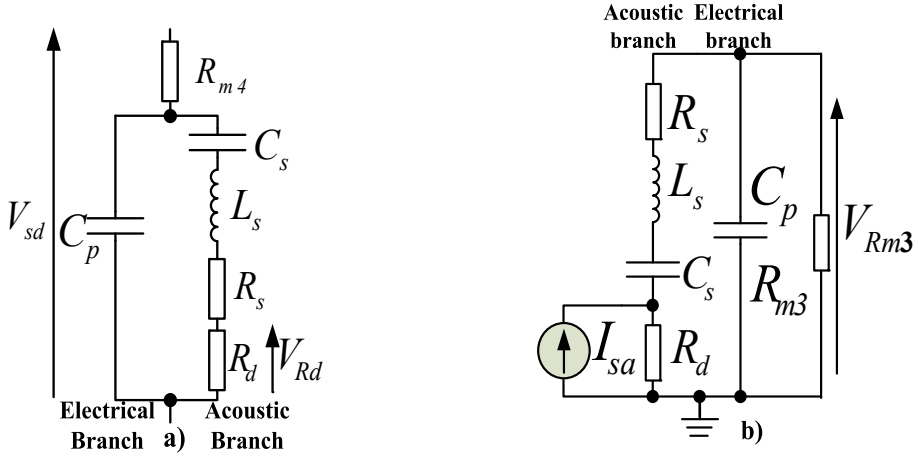

Figure 3-4: a) BVD equivalent circuit model b) Selected receiving transducer model

$$G_{aTx}(s) = \frac{V_{Rd}(s)}{V_{sd}(s)} = \frac{n_{11}s}{d_{13}s^3 + d_{12}s^2 + d_{11}s + d_{10}}. \tag{3.10}$$

$$G_{aRx}(s) = \frac{V_{Rm3}(s)}{I_{sa}(s)} = \frac{n_{21}s}{d_{23}s^3 + d_{22}s^2 + d_{21}s + d_{20}}\,\Omega. \tag{3.11}$$

n_{11}	d_{13}	d_{12}	d_{11}	d_{10}
0.78×10^{14}	3003	0.14×10^{11}	0.4×10^{15}	0.1×10^{22}
n_{21}	d_{23}	d_{22}	d_{21}	d_{20}
39	1.7×10^{-9}	8.4×10^{-4}	10.2	5×10^{7}

Table 3-3: Parameter values of the transmitting and receiving transducer transfer functions

3.1.4. Model Verification

These theoretical models are used to simulate the transducer time and frequency responses. The practical experiment introduced in Subsection 3.1.1 is simulated and the results illustrated in figure 3-5. The pulse rate remains at 500 Hz and the observed temporal response is from the receiving transducer model output before amplification. Compared with the measured results in

figure 3-2 b), the simulated circuit model yields a 40 kHz resonance with similar under-damped envelope. The similarity between simulated and measured temporal transducer receiver response is strong evidence that the selected transducer model can be used to predict transducer output response. Also illustrated, in figure 3-6, is the transfer function derived from a simulated frequency sweep from 10^4 to 10^5 Hz, for both transducer models.

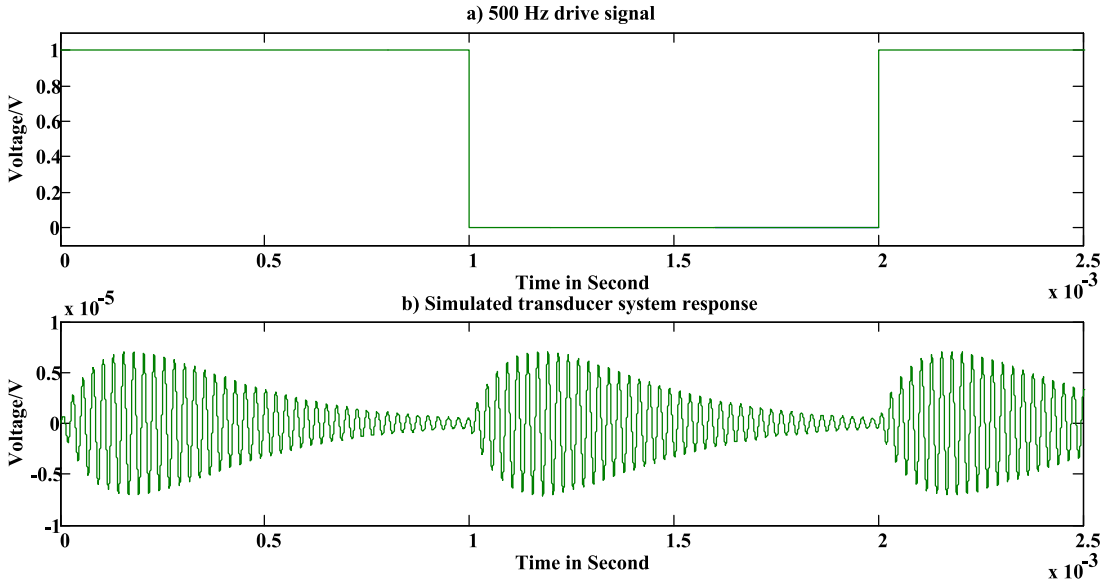

Figure 3-5: Simulated transducer system response to a 500 Hz pulse drive signal

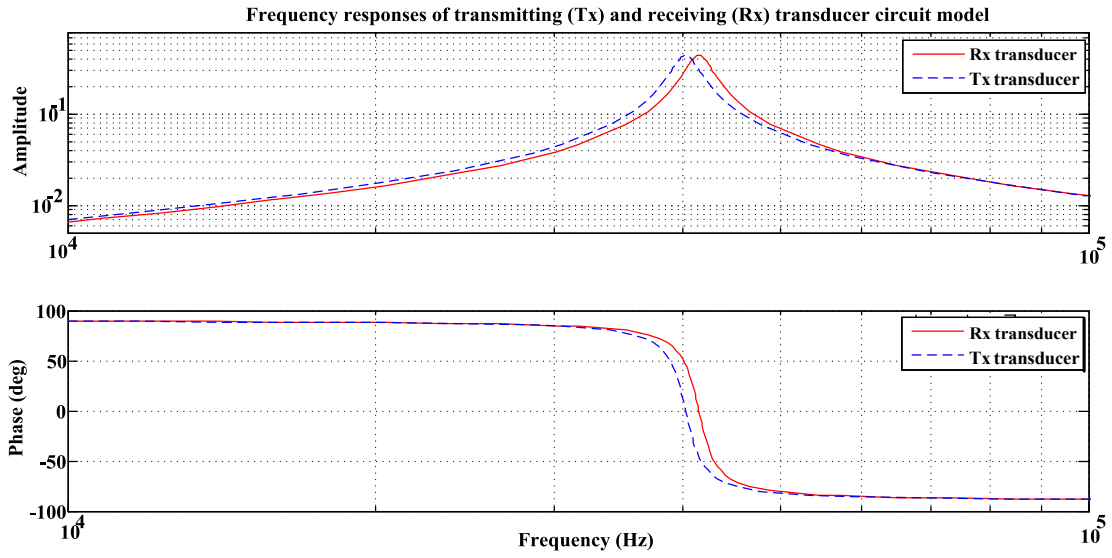

Figure 3-6: Frequency and phase responses of transducer circuit models

3.2. A Phase-Modulation based US System

This section will introduce an US continuous wave transmission system using phase modulation (PM) and evaluate its performance through the quality of the recovered message.

3.2.1. Testing Platform

The simulation test bench developed for the coded data transmission experiment is essentially an expansion of figure 3-1 with encoding and decoding subsystems. As illustrated in figure 3-7, these two subsystems comprise two multipliers; one is used to modulate the carrier wave with digital information and the other functions as a carrier-synchronised demodulator to extract information from the phase of the modulated signal.

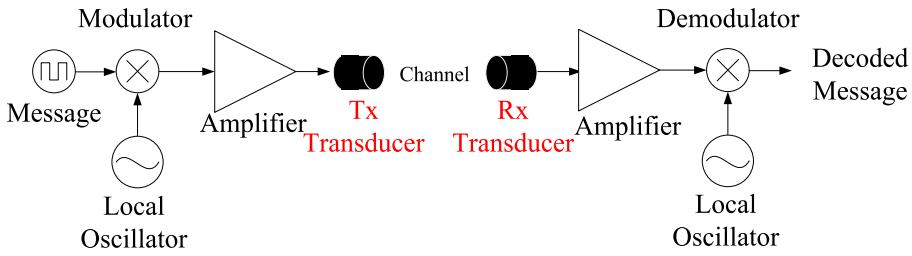

Figure 3-7: Conceptual diagram of PM-based US system

A more detailed block diagram of figure 3-8 explains the working principle of the modulator and demodulator. On the left hand side, a 2 kHz bi-polar message signal is multiplied with a 40 kHz carrier to produce a BPSK signal. The modulated signal is then amplified through a driver stage and conveyed to excite the transmitting transducer. On the right hand side, the process to demodulate the message can be decomposed into the following 4 steps:

- raising the signal level
- reshaping the signal to compensate for the filtering effect of the transducer
- digital carrier recovery
- phase detection

The following subsection will briefly introduce two commonly used driver techniques.

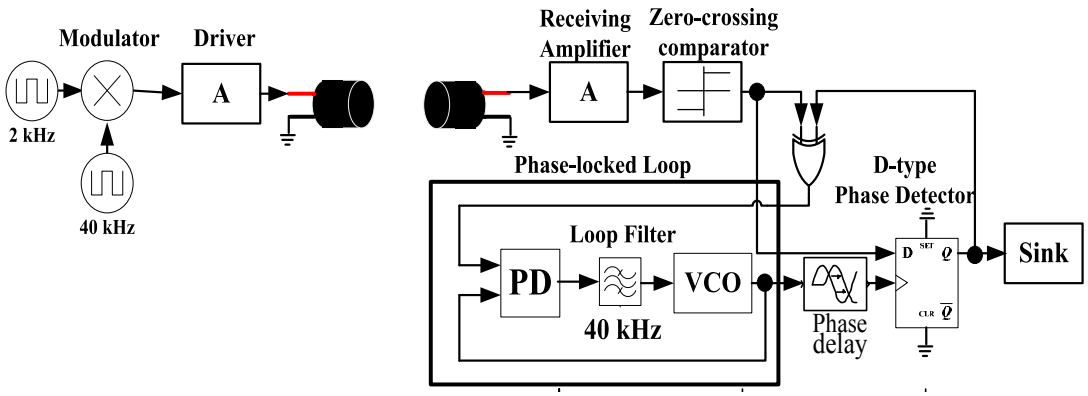

Figure 3-8: Block diagrams of phase modulation and demodulation systems

3.2.2. Driver Model and Modulator

Existing US driving technology can be classified as linear or pulsed drive [89]. A linear drive is, fundamentally, a linear power amplifier with a single-ended configuration and an impedance matching part for optimising drive capability and reducing energy conversion loss. Whereas pulsed drive provides pulsed stimuli designed to give an impulsive hit to the transducer, so that the transducer yields a higher sound level.

The excitation of *piezoelectric* transducers is normally achieved using a low-impedance drive circuit since the *piezoelectric* crystal appears as a capacitive load [89]. An Open-Drain (OD) driver as shown in figure 3-9 a) implemented using a metal oxide semiconductor field effect transistor (MOSFET) is widely employed [90]. In the OD configuration, the *drain* terminal of the transistor is linked with a voltage source through a pull-up resistor and the transistor *source* terminal is grounded. The advantage of this drive configuration is that the transistor is working in a switching manner and can provide an abrupt drive voltage change. An H-bridge drive configuration [91], as shown in figure 3-9 b), doubles the driving voltage capacity. In theory, an H-bridge driver creates a bi-directional current flow to equally polarise the transducer thus producing a voltage change twice that of the driving signal on each path.

In the simulation platform, OD and H-bridge drivers are implemented using analogue device models provided in *Simulink* and linear amplification is simply modelled as numerical gain. An exclusive OR (XOR) gate operates as a mixer that modulates the 2 kHz information onto 40 kHz carrier.

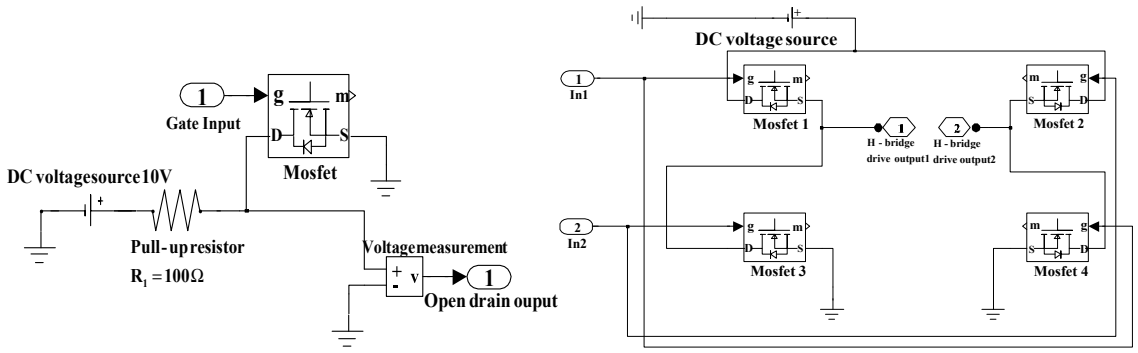

Figure 3-9: a) Single-ended OD drive configuration b) Double-ended H-Bridge drive configuration

3.2.3. Receiving Amplifier and Zero-Crossing Comparator

An operational trans-impedance amplifier circuit has been selected, providing a voltage output varying according to a current input. The second slot of the simulation result in figure 3-5 suggests the received US signal amplitude is fairly weak and requires large gain amplification. The trans-impedance amplifier is followed by a zero-crossing comparator to re-shape the received amplitude-varying envelope into saturated square wave.

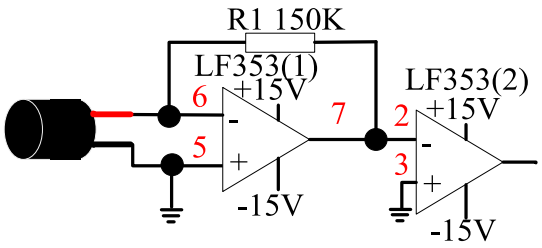

Figure 3-10: Trans-impedance amplifier and zero-crossing comparator circuits

3.2.4. Phase-Locked Loop

Coherent phase demodulation has to be implemented in the receiver using only the knowledge of the phase of the *received BPSK signal*. Accordingly, the receiver is required to be able to extract this information from the received signal, assuming no simultaneous carrier wave is transmitted. A linear Phase-Locked Loop (PLL) model composed of a phase detector, a loop filter and a Voltage Controlled Oscillator (VCO); can behave as a carrier synchroniser [92] to maintain correct timing for message decoding. The *VCO output* produces a regenerated carrier signal whose frequency is determined by the DC input voltage to the VCO. A phase comparator in the

PLL is chosen to detect the phase difference between the *BPSK signal* and *VCO output*. An error voltage is obtained as a result of the phase comparison. This phase error indicates whether the local oscillation is leading or lagging in phase and is used to tune the VCO frequency. A low pass filter controls the amount of voltage to pass through and eliminates any unwanted transients. In-phase lock will only be achieved when the locally generated 40 kHz square wave is synchronised with the zero-crossing comparator output signal.

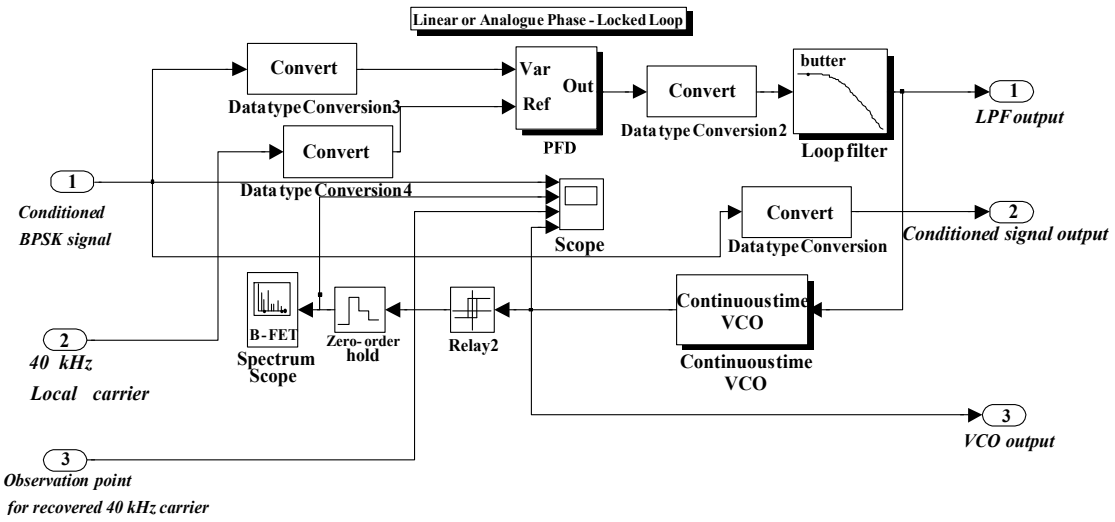

Figure 3-11: Analogue PLL *Simulink* model [93]

In the simulation, the selected *Simulink* PLL model uses a low-pass *Butterworth* first order filter. The cut-off frequency is set to be 4.1×10^4 Hz. The quiescent frequency of VCO is chosen to be 4×10^4 Hz. The VCO input sensitivity is 1 Hz/V and output magnitude is 5V.

3.2.5. D Flip-Flop based Demodulator with Delay Generator

A D-type flip-flop with clock input is used in this design to detect the phase difference between the *received BPSK signal* and the *VCO output*. The D flip-flop passes the logic state of the D input (*BPSK signal*) to the Q output at a rising edge of the clock signal (*VCO output*). Based on this working theory, the *VCO output* should be able to sample the phase modulated carrier at its rising edge and holds the same state as the D input until an anti-phase signal is identified. In order to lock on to the voltage level of the *BPSK signal*, the phase of the *VCO output* must be offset by 90 degrees with reference to the carrier phase. This is, in practice, achieved by delaying the PLL *VCO output* by 6.25 ms. An additional XOR gate shown in figure 3-8 is used to produce the

Conditioned Received Signal compared with *Demodulated Output* and provides an unmodulated carrier signal for PLL to synchronise with.

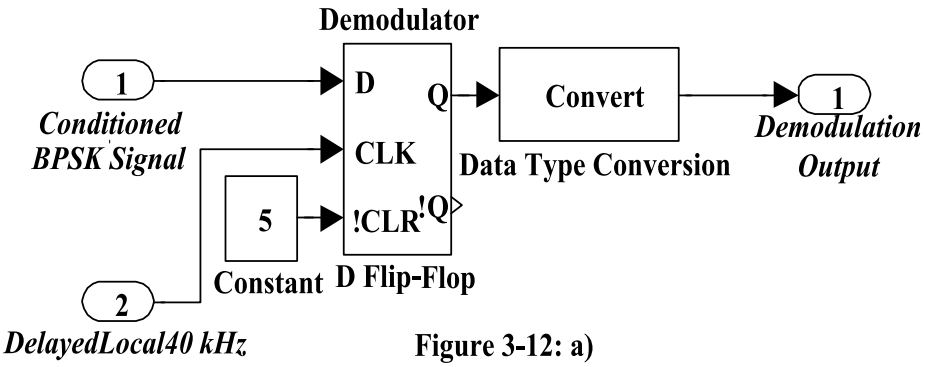

Figure 3-12: a)

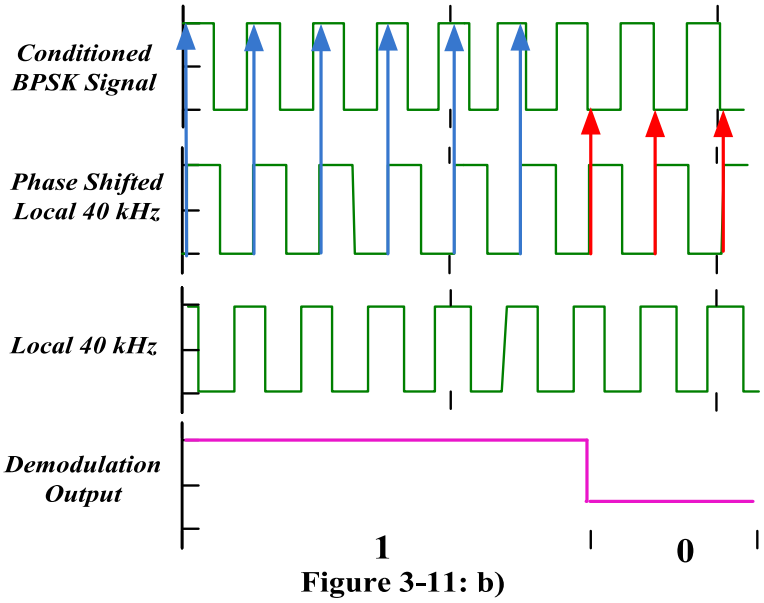

Figure 3-11: b)

Figure 3-12: a) D type demodulator b) Illustrative example of demodulation mechanism

3.3. Results

The system performance during data transmission will be evaluated through simulated and measured results.

The first experiment is designed to simulate the transducer *Simulink* model-based communication system and evaluate the system capacity using binary information transmission. An oscillating binary message with a frequency of 2 kHz (figure 3-13 a)) is modulated on a 40 kHz square wave carrier. The magnitude of BPSK signal is amplified to ± 10 V via an H-bridge driver as shown in figure 3-9 b). The *Simulink* transmitting transducer circuit model, figure 3-4 a), stimulated by the

BPSK drive signal, figure 3-13 b), yields an under-damped resonance. The receiving transducer model responds to the transmitted signal, figure 3-13 c), with a delayed resonance, figure 3-13 d). This received resonance is decoded using the principle explained in sections 3.2.2-3.2.5 to reproduce the original 2 kHz message signal, figure 3-13 e). As observed in figure 3-13 c) and d), the under-damped waveforms resulted from both transducer characteristics are incapable of settling down to respond to the phase switching commanded by the drive signal, figure 3-13 b). Consequently, the first two bits in the resultant data, figure 3-13 e), are delayed due to the gently decaying resonant responses of both transducers (the start of the transient). However, after the second bit, the subsequent decoding process illustrated in figure 3-14 succeeds in demodulating the message when the receiving transducer response has stabilised.

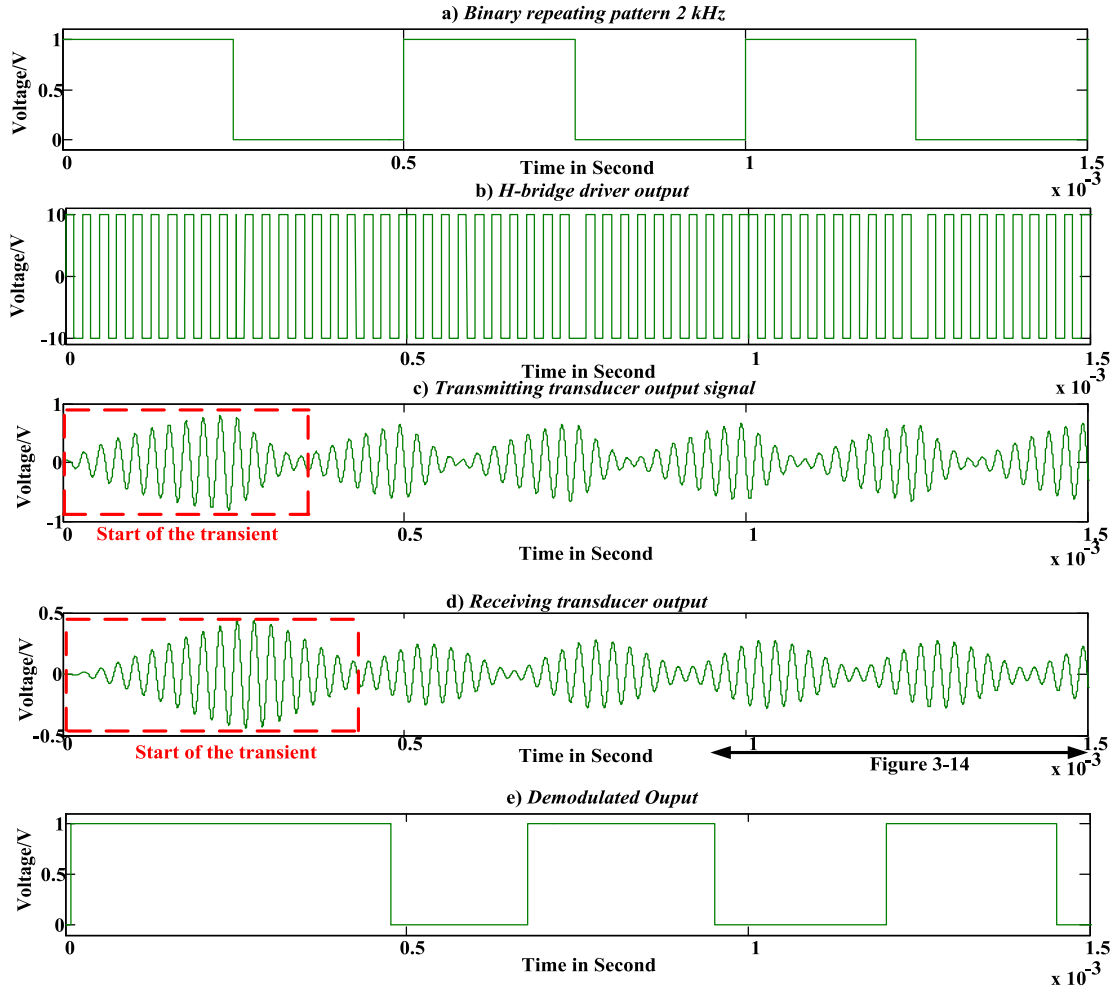

Figure 3-13: Simulated results – BPSK coding and decoding of an US transducer system

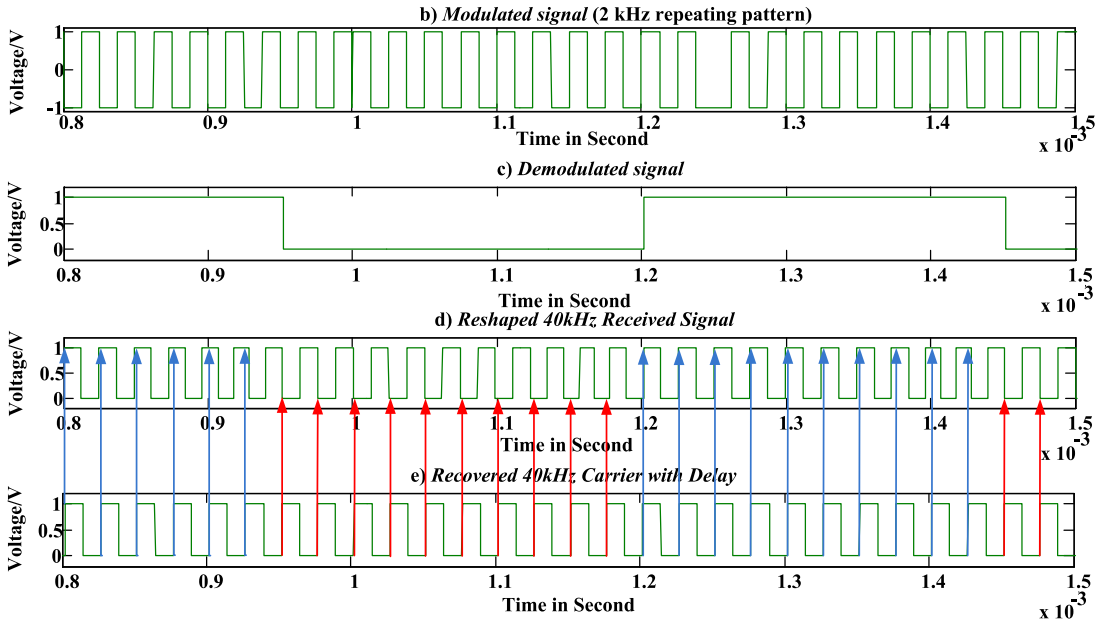

Figure 3-14: Simulated results – amplified regions in figure 3-13 focusing on demodulation process

The second test uses a random message signal. The pulse train pattern is defined to be [0 1 1 0 1 0 0 0 0 0 0 1 0 0 1]. This test code is converted into bi-polar signal before modulation. The phase modulation is realised by multiplying the binary sequence with the carrier signal. The bit rate is specified to be 2 kHz and carrier frequency is 40 kHz. Figure 3-15 b) demonstrates the decoded data, which has verified by simulation that the transmitted code sequence can be successfully recovered in the receiving system.

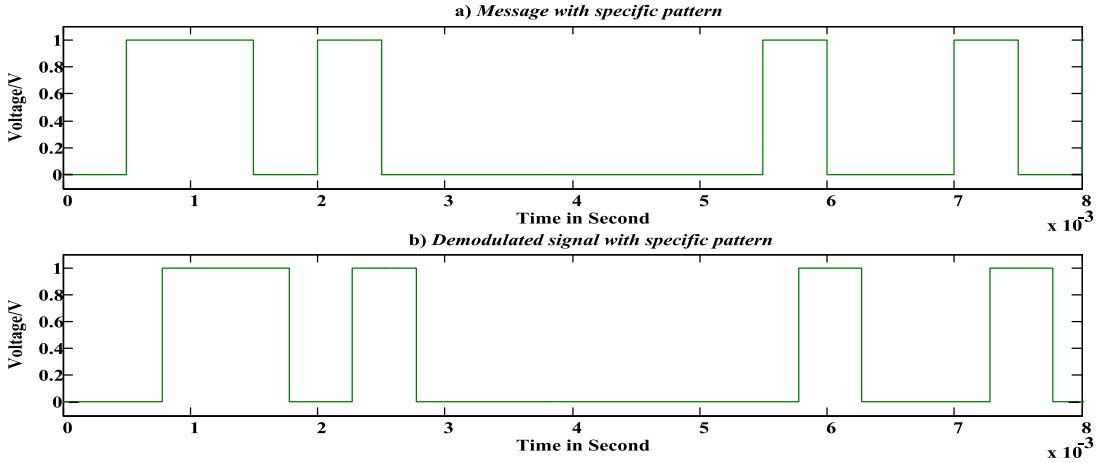

Figure 3-15: Simulated results – specific random message pattern

A practical implementation of the simulations in the early part of Section 3.3 is achieved to verify the simulated results. A 2 kHz repeating pulse train is selected as modulation signal and the carrier remains at the same frequency. The first group in figure 3-16 presents the *message* signal, received US energy and decoded message. The other group, figure 3-17, only shows the message and demodulated results. Although the repeating binary sequence is decoded by the receiver circuit, the demodulated data produces two different kinds of error codes. Figure 3-17 reveals that the pulse width is varied according to the transducer dynamic. The second results tell that the decoded binary information is distorted by the erroneous decision made by the phase detector.

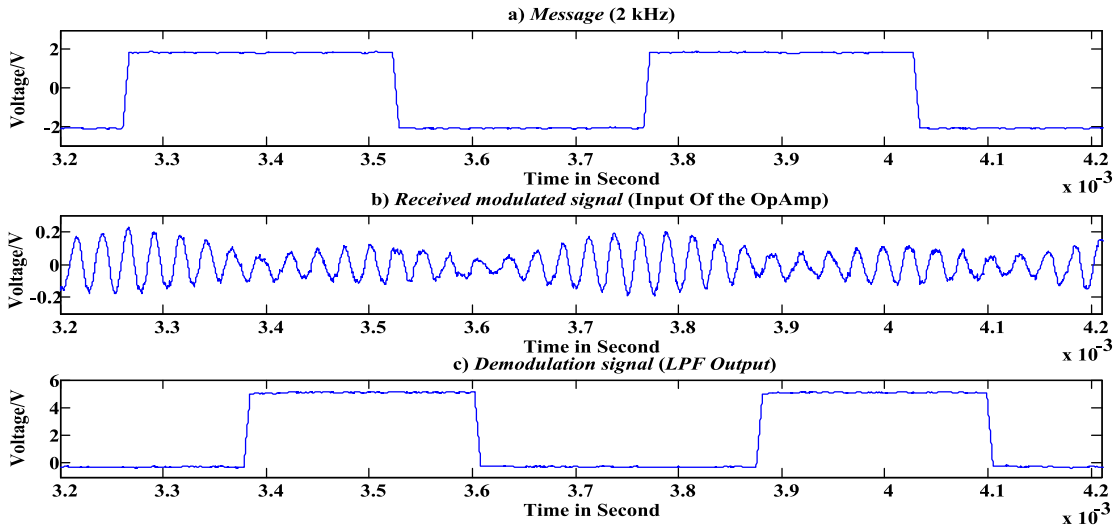

Figure 3-16: Measured results – a) *Message* b) *Received BPSK signal* c) *Demodulation result*

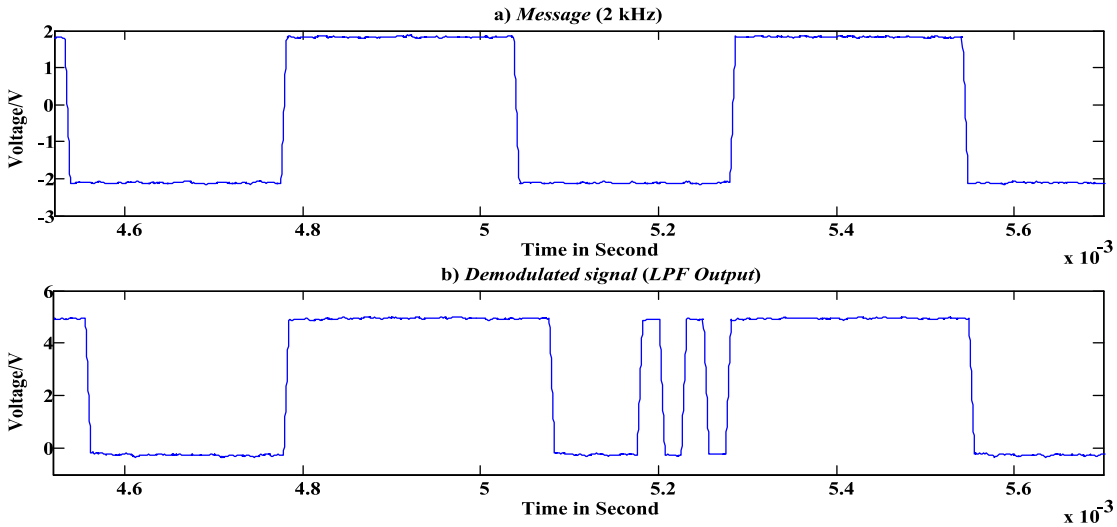

Figure 3-17: a) Received *Message* b) Measured *received BPSK output* with error code near phase change

3.4. Summary

The first part of this chapter demonstrated an US transducer stimulated with 500 Hz square wave can be simulated and produce comparable results with those observed in practice. The use of an H-bridge driver enhances the delivery of power in an attempt to control the oscillatory transient of the transducer, but the acoustic resonance still takes a long time to establish the correct phase. This limits the speed of phase modulation that can be achieved because of the delay in phase change of the output transducer's resonances. A decoding approach was attempted, illustrating a mechanism to promptly detect changes in phase of the received signal. However, the phase detector encounters problems due to variable changes in phase produced by the slow decay of the transducer resonance. The presence of error bits identifies the phase change rate limit that can be used. This cannot be improved upon without the use of control techniques to minimise the resonant effects in each transducer.

Chapter 4.

VSC-based Ultrasonic Transmitter

The capacity of a phase modulation (PM) system is limited by the rate at which the phase of the carrier signal can be changed. For ultrasonic (US) systems the change is delayed by many cycles due to the inertial properties of the *piezoelectric* transducer. Reducing the transducer response time will directly increase capacity. Various methods have been investigated in similarly damped systems to reduce the response time [94-95]. Variable Structure Control (VSC) using high speed switching has been successful in reducing the transient response of system dynamics in a variety of applications, and can be physically realised [96-97]. In this chapter we compare an US transmission system with and without VSC and quantify the reduction in transient response time.

Figure 4-1 shows the block diagram of a typical US transmission system, where an US transmitter may be decomposed into a signal source "*r*", driver "F" and an US transducer "G". The signal source, *r*, is the Binary Phase Shift keyed (BPSK) message signal, consisting of a sinusoidal carrier with occasional 180 degrees phase shifts. The driver block provides sufficient gain to excite the transducer. The output of the driver, F*r*, is an amplified version of *r*, possibly modified to compensate for the characteristics of the transducer with the aim of making *y* as close to *r* as possible. The block "G" is the US transducer. This is usually modelled as a linear system defined by its transfer function. To illustrate the uncompensated performance of the transducer, figure 4-2 shows the simulated acoustic output of the system when the input is a typical 40 kHz BPSK test signal with a 2 kHz bit rate. The double-ended arrow indicates a bit period of 500 milliseconds. Note that the acoustic output takes many cycles to synchronise with the message signal after a phase shift. This limits the data rates as phase measurement is required to identify each transmitted bit.

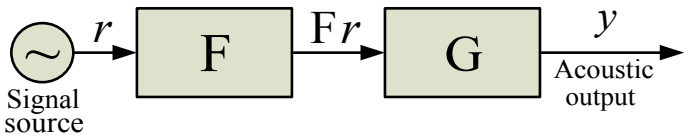

Figure 4-1: Block diagram of standard US driver

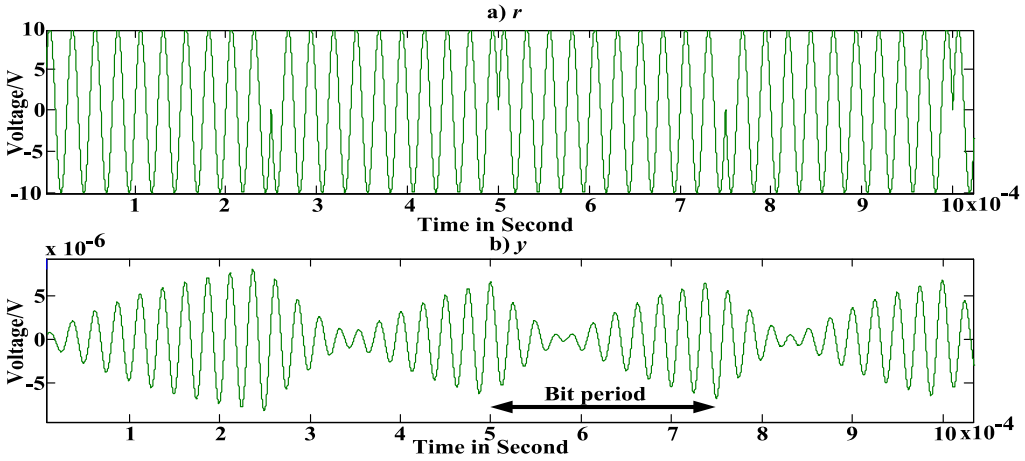

Figure 4-2: a) Simulated BPSK drive signal b) Acoustic BPSK signal with delay at phase change

4.1. Design of Dynamical Transient Compensator

The differences between the input and output waveforms in figure 4-2 are due to the transducer characteristics introduced in Subsection 3.1.3. The response illustrates the dynamics of the transmitting transducer without control. To reduce the duration of the transient response of the transducer system, dynamical feedback compensation can be applied. However, such designs rely on having accurate descriptions of the dynamics for both the transducer and driver amplifier.

Here, an implementation of dynamical feedback is chosen that is less sensitive to the precise behaviour of the system dynamics. A method known as a *Variable Structure Control* (VSC) is used and illustrated in figure 4-3. This approach is designed to switch between two feedback configurations, A and B, using a *switching line*, *sw*, condition to constrain the dynamics of the system.

Each of the feedback configurations results in a closed-loop transfer function. One yields negative feedback via functional blocks F, A, G and H and the other provides positive feedback via blocks

F, B, G and H. The feedback signal, Hy, is the measure of the acoustic output of the transducer. This is derived from the current in the acoustic branch of the BVD transducer model, G.

Techniques for the design of a VSC *switching line* are described in [98] and can be summarised by the diagrams shown in figure 4-4. Values for gains A and B are chosen so that the phase portraits for the negative and positive feedback configurations have similar shapes to those shown in figure 4-4 b) (*stable focus*) and figure 4-4 c)(*saddle point*). The *switching line* condition, *sw*, is then chosen to have a gradient, c_{tran}, to achieve a system property called *sliding mode*. This property uses the switching between the two feedback configurations to constrain or trap the overall system dynamics to that described by the *switching line*, $sw = 0$. In practice, the tightness of constraint to the *sw* is governed by the switching speed and thus is limited by the sampling period, ΔT, when using the discrete phase plane and other dynamics [99].

The *sw* condition used to select the feedback configurations in a discrete phase portrait [99] is constructed from the sampled error signal, e, $(\mathrm{F}r - \mathrm{H}y)$.

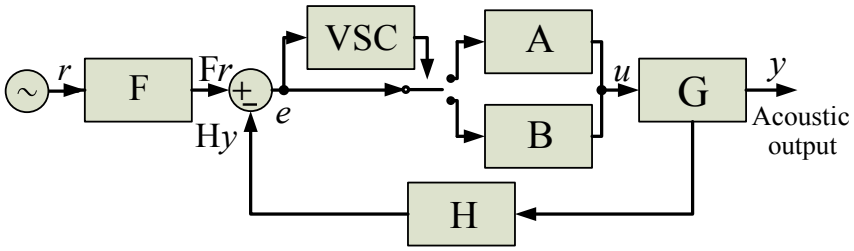

Figure 4-3: Block diagram of the VSC transmitter system

Symbol	Description
F	Amplification to Demand Signal
G	Transfer Function of US Sensor
H	to derive the equivalent electrical Signal
VSC	Discrete VSC Algorithm
r	Demand Signal
y	Acoustic Output of Transducer
e	Error Signal Difference between *r* and *y*
A, B	Positive and Negative Gain Blocks

Table 4-1: System components in VSC-based transmitter

4.1.1. Construction of Discrete Phase Portrait

The discrete phase portrait used in this design is based on the discrete version of VSC as described in [99]. The behaviour of the system is illustrated using a phase portrait. This is the temporal locus of the points $\mathrm{d}e/\mathrm{d}t\,, e$. In practice the error signal *e* is sampled at discrete intervals of a sample period ΔT . The backward difference approximation of the gradient is used i.e. $\Delta e/\Delta T \equiv \frac{e(n)-e(n-1)}{\Delta T}$ and the locus of $\big(\Delta e/\Delta T\,, e(n-1)\big)$ is used. For the discretised phase portrait to yield an adequate description of the system performance for the implementation of VSC, the sample period ΔT must be much shorter than the principal system time constant.

The motion of the system is mapped onto the discrete phase plane as shown in figures 4--4 g) and i). The phase plane can be divided into regions with one boundary defined by the *sw*:

$$sw \equiv \big(e(n) - e(n-1)\big)/\Delta T + c_{tran} * e(n-1). \tag{4.1}$$

where 'c_{tran}' is a positive constant. The *switching line* has slope, c_{tran}, passes through the second and fourth quadrants and is defined by:

$$sw = 0. \tag{4.2}$$

A second order system can produce several types of phase portrait which are overviewed in [9]. In this research two kinds of phase portrait are of interest. The *stable focus* spirals in and takes a long time to converge to the origin. The *Saddle point* is asymptotically stable in regions *II* and *IV* and unstable in regions *I* and *III,* see quadrant labelling in figure 4-4 j). The VSC attempts to constrain or trap the second order dynamics of a system onto a *switching line* by coupling the trajectories in the first and third quadrants of a *stable focus* portrait and those in second and fourth quadrants of a *saddle point* portrait as illustrated in figure 4-4 j). Once constrained the dynamics of the system are described by the dynamic of the *switching line*, that is a first order system with time constant, c_{tran}, the gradient of the *switching line.*

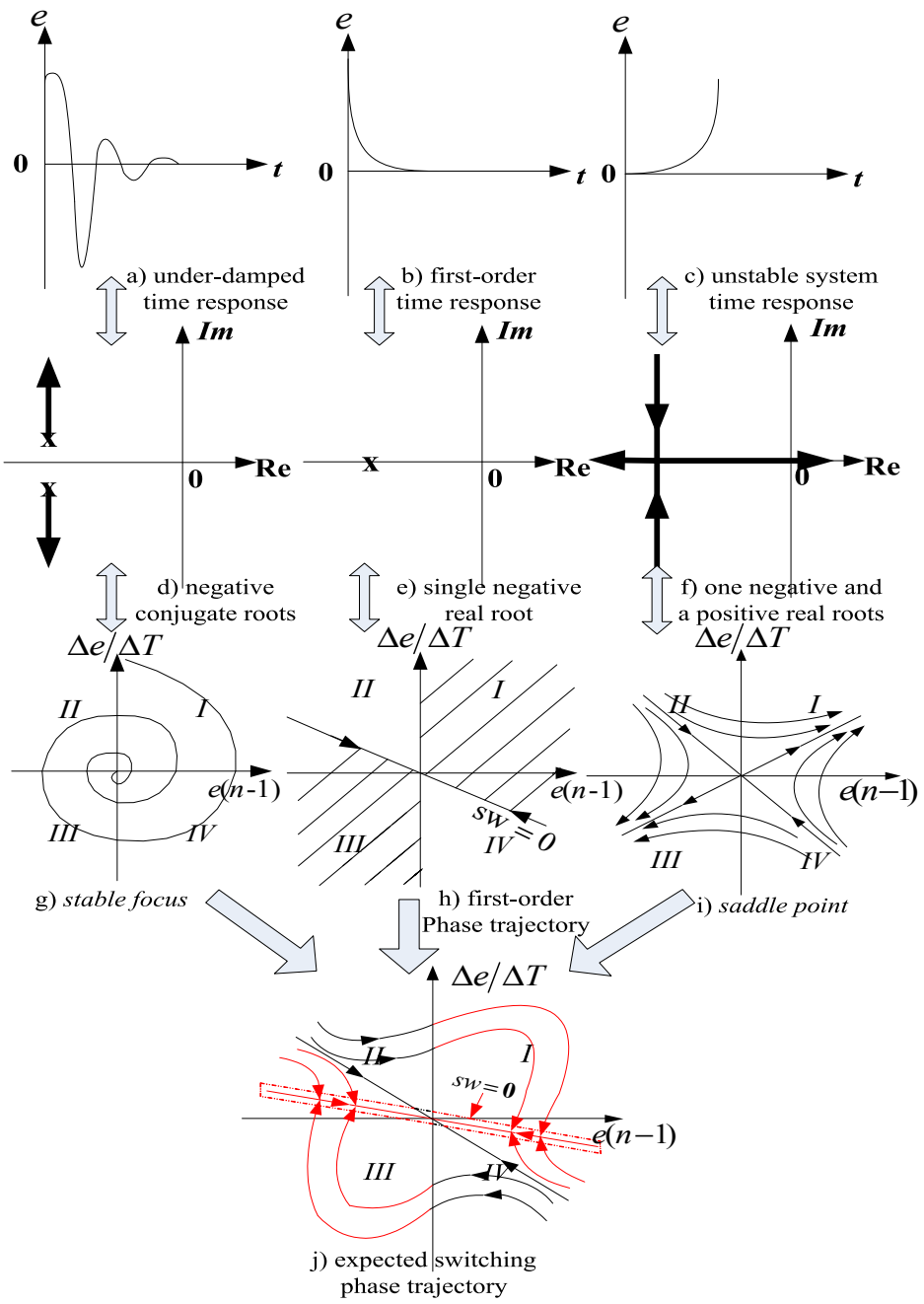

Figure 4-4: The composition of two selected system dynamics

The movement of the trajectory around the phase plane can be used to identify the boundaries of different regions. The phase plane is then partitioned into 4 regions by $\Delta e/\Delta T = 0$ and $sw = 0$:

$$\begin{aligned}
&\text{Region } I: e(n-1) \geq 0, sw > 0,\\
&\text{Region } II: e(n-1) < 0, sw \geq 0,\\
&\text{Region } III: e(n-1) \leq 0, sw < 0,\\
&\text{Region } IV: e(n-1) > 0, sw \leq 0.
\end{aligned}$$

In region *I* and *III* , the absolute magnitude of the error is increasing and negative feedback should

be applied to inhibit this increase. Conversely, when the product of these two signals is negative, in region *II* and *IV*, positive feedback should be applied to decrease the absolute value of the error signal.

System feedback is proportional to *e* and is determined from (4.3) below.

$$u = \begin{cases} \mathrm{A} * e, e(n) \in I \cup III, \\ \mathrm{B} * e, e(n) \in II \cup IV. \end{cases} \tag{4.3}$$

where A and B are the gains for the negative and positive feedback.

4.1.2. Design of Negative and Positive Feedback Paths

The VSC compensation algorithm can only be effective when the two feedback paths associated with A and B both produce appropriate closed-loop dynamics. The dynamics are assumed to be predominantly second order. In the phase plane, the second order closed-loop dynamics should be chosen to give a *stable focus* trajectory for the negative feedback path and a *saddle point* trajectory for the positive feedback path [100]. The VSC combines the useful regions of the two phase portrait trajectories to obtain the desired, approximate, first order system error response as defined in figures 4-4 j).

Note that to achieve each of the desired phase portrait trajectories the closed-loop system poles must be carefully selected. This can be assessed by plotting a *root-locus* for each feedback loop used in the system. For the negative feedback arrangement, the closed-loop poles must be dominated by two complex conjugate poles of adequate speed to achieve a *stable focus* phase portrait trajectory. For the positive feedback arrangement, the closed-loop system pole set must be dominated by two real poles with one in the left half of the Laplace plane and the other in the right half plane to obtain a *saddle point* trajectory. The major design problem in the VSC control system is the selection of gains for the feedback paths, A and B.

$$\mathrm{TF}_n = -\mathrm{AG}_{aTx}(\mathrm{s}) = -\frac{\mathrm{A}n_{31}s}{(s-p_{13})(s-p_{12})(s-p_{11})}. \tag{4.4}$$

$$\mathrm{TF}_p = \mathrm{BG}_{aRx}(\mathrm{s}) = \frac{\mathrm{B}n_{41}s}{(s-p_{23})(s-p_{22})(s-p_{21})}. \tag{4.5}$$

n_{31},n_{41}	p_{11},p_{21}	p_{12},p_{22}	p_{13},p_{23}
0.78×10^{14}	-4.7×10^{6}	$-6818 + 264380.i$	$-6818 - 264380.i$

Table 4-2: Values of the VSC transmitting transducer open-loop transfer functions

The *root-locus* plot of the transducer feedback system can be used to analyse the system dynamics when its root trajectories vary according to the positive and negative feedback gains. Figure 4-5 depicts the root loci of the transducer system configured as shown in figure 4-3 with only negative feedback used to control the acoustic output. The p_{ij} and z_{ij} used in the following analysis are the notations for the i^{th} pole and the j^{th} zero in corresponding transfer functions. The feedback gain sweep used in the *root-locus* plot is in the range [0 2000].

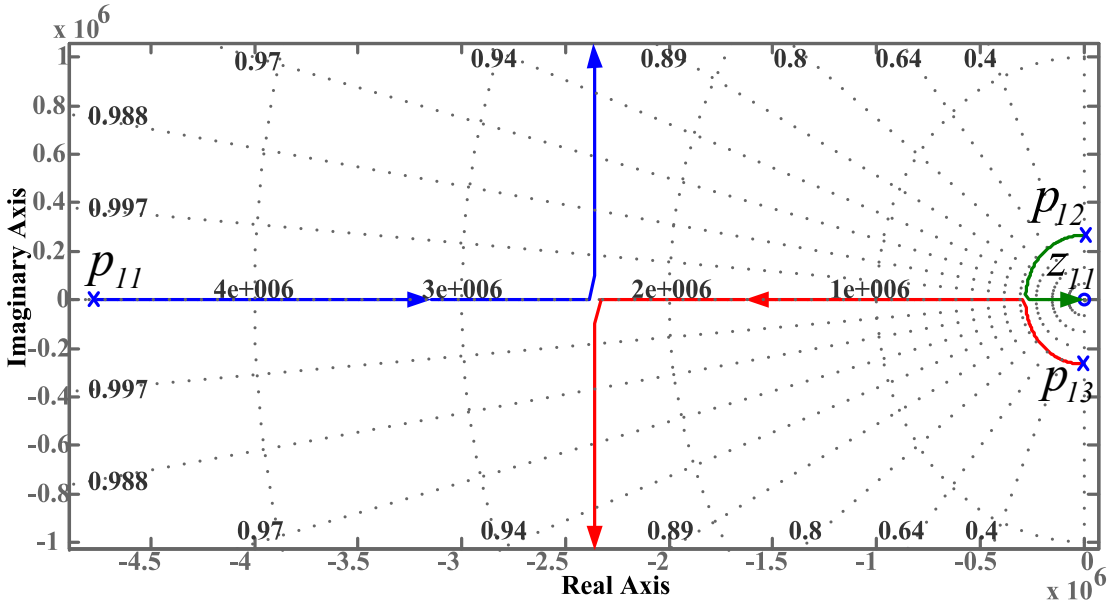

Figure 4-5: *Root-locus* plot for negative feedback loop using acoustic output

The initial pole positions in figure 4-5 demonstrate a pair of conjugate roots and a negative real root. Since the conjugate pair is closer to the origin, they are considered dominant. As the gain increases, the conjugate roots meet on the real axis and become a double real root. Then one real pole cancels with its zero counterpart. The other pole slides towards the other real pole coming inward. These two poles overlap and start to form a new pair of complex roots when the loop gain is greater than 200. The above analysis suggests that for the negative feedback arrangement to achieve dominantly under-damped system dynamics a value of K= 200 should be used.

Figure 4-6 illustrates a *root-locus* of the same system where positive feedback is used. The

conjugate pair and the real pole are initially located in the stable region of Laplace plane. As gain is increased, the conjugate pair cross the imaginary axis and converges back to the real axis in the unstable region. The two positive conjugate poles intersect on the real axis and then separate. One forms a pole-zero cancellation and the other moves away and becomes increasingly positive. These stable and unstable real poles present the dominant feature giving *saddle point* dynamics when the positive feedback gain K has reached K= 104.

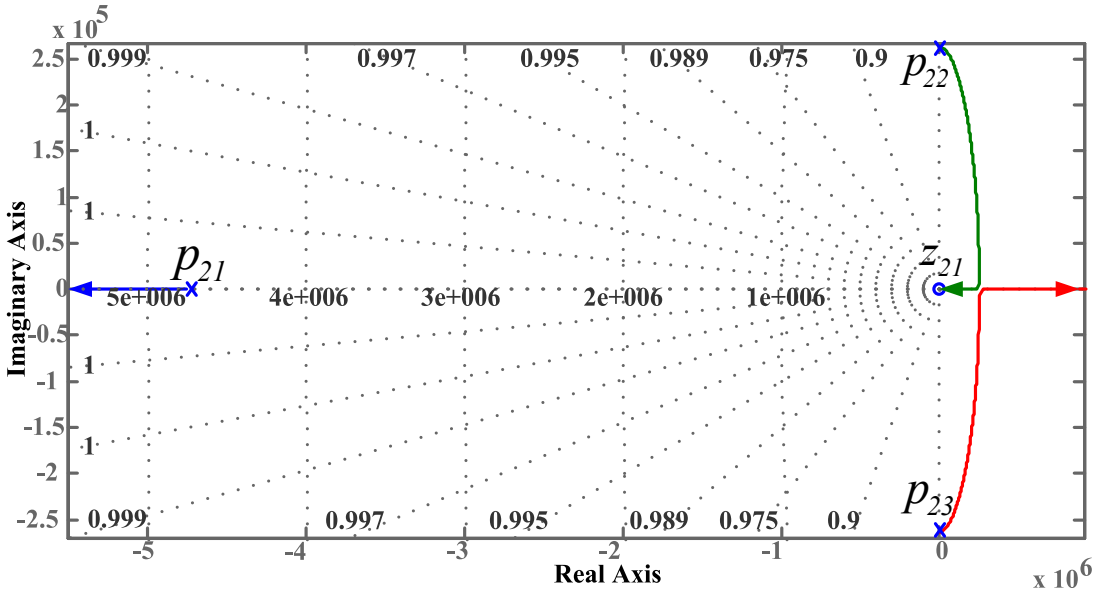

Figure 4-6: *Root-locus* plot for positive feedback loop using acoustic output

4.1.3. Design of the Sensing Unit

In a real transducer it is not possible to measure a parameter equivalent to the current in the acoustic branch of the BVD model, as no separate electrical and mechanical parts exist. An equivalent approximation for the transducer output signal can be achieved using the differencing circuit in figure 4-7 The value of the capacitor, C_{m1}, is chosen to match the equivalent capacitance in the electrical branch of the BVD model of the transducer.

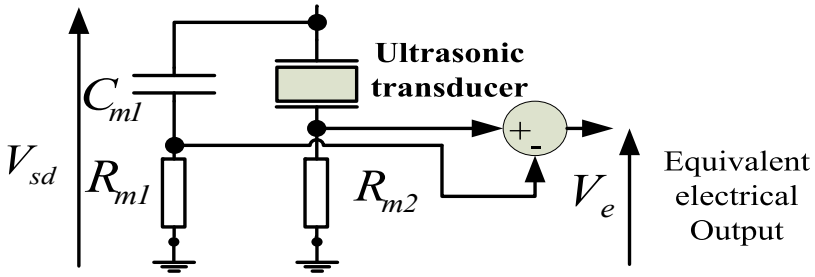

Figure 4-7: Circuit diagram for transducer with electrical output measurement circuits

Symbols	Values	Symbols	Values
C_{m1}	2100 pF	H	17.5
R_{m1}	10 Ω	A	100
R_{m2}	10 Ω	B	100

Table 4-3: Values of the VSC system with electric equivalent feedback

Note that the additional circuits in this sensing configuration are only used for current measurement in transducer and capacitive branches. The modification of the sensing method should not unduly change the dynamics of the system when using positive and negative feedback. Therefore, root-loci analyses must then be used to assess the impact caused by the sensing change on the closed-loop system dynamics for positive and negative feedback. The transfer functions, $-\mathrm{AG_{eTx}}$ and $\mathrm{BG_{eTx}}$, of the receiver VSC transducer model with positive and negative feedback are respectively stated in (4.6) and (4.7).

$$\mathrm{TF}_n = -\mathrm{AG}_{eTx}(\mathrm{s}) = -\frac{\mathrm{A}n_{51}s}{(s-p_{34})(s-p_{33})(s-p_{32})(s-p_{31})}. \tag{4.6}$$

$$\mathrm{TF}_p = \mathrm{BG}_{eRx}(\mathrm{s}) = \frac{\mathrm{B}n_{61}s}{(s-p_{44})(s-p_{43})(s-p_{42})(s-p_{41})}. \tag{4.7}$$

p_{32},p_{42}	p_{33},p_{43}	p_{34},p_{44}	n_{51},n_{61}	p_{31},p_{41}
-2.2×10^6	$-6860 + 264409i$	$-6860 - 264409i$	0.61×10^{21}	-4.7×10^7

Table 4-4: Values of the VSC transmitting transducer open-loop transfer functions

The same *root-locus* method applied in Subsection 4.1.2 is used here to examine the system dynamics when the transducer system feedback is derived from the electrical equivalent output. Figure 4-8 depicts the root loci of the transducer system configured as shown in figure 4-3 with only negative feedback used to control the acoustic output.

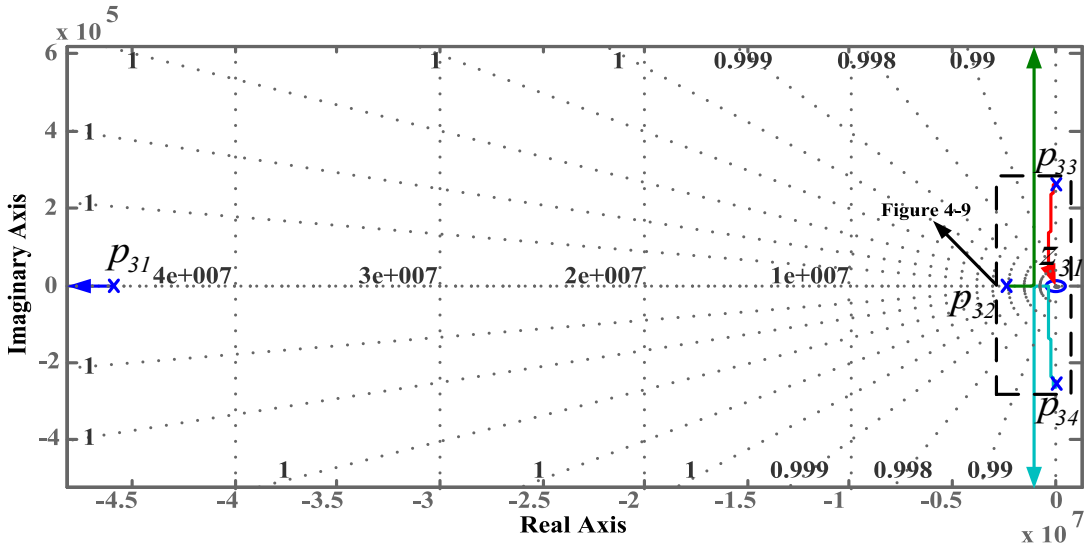

Figure 4-8: *Root-locus* plot for negative feedback loop using electrical output (overview)

The area of figure 4-8 that determines the dominant system dynamics is magnified and plotted in figure 4-9. The complex conjugate poles converge towards each other and form a double pole on the real axis. This convergence implies a *stable focus* phase portrait with reduced speed of decay. Then the double real pole breaks away. After separation, one pole approaches the nearest zero at the origin. The other pole moves horizontally along the real axis and meets a corresponding real pole moving towards the origin from the right hand side of s-plane at -1.2×10^6. The breakaway of these two real poles produces a conjugate pair. In the phase portrait domain, these conjugate roots feature as a *stable focus* with higher resonant frequency than the dominant complex poles close to the origin. However, for VSC-based US system, the dominant complex conjugate pair trajectories that achieve a *stable focus* phase portrait are those that are closest to the origin. The desired conjugate pair with appropriate performance is obtained with gain values of K that are no larger than 490.

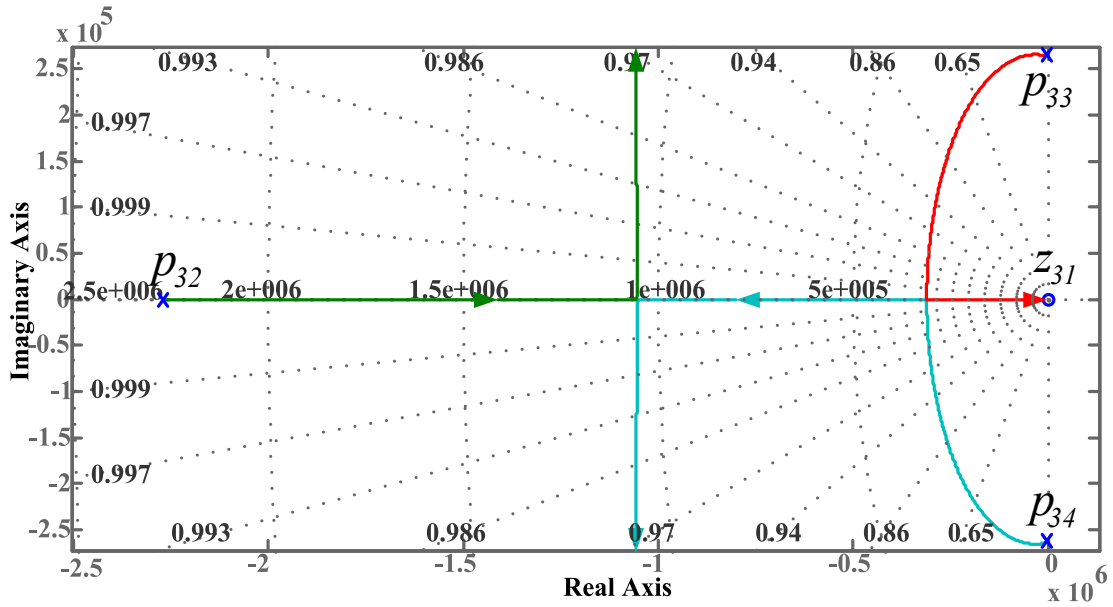

Figure 4-9: *Root-locus* plot for negative feedback loop using electrical output (focused view)

Figure 4-10 plots the root loci generated by the system with positive feedback. The locations of the open-loop system poles and zeros are the same since the same transducer transfer function is used. As the loop gain sweeps from [0 2000], the real pole located at the far end of the stable region move inwards.

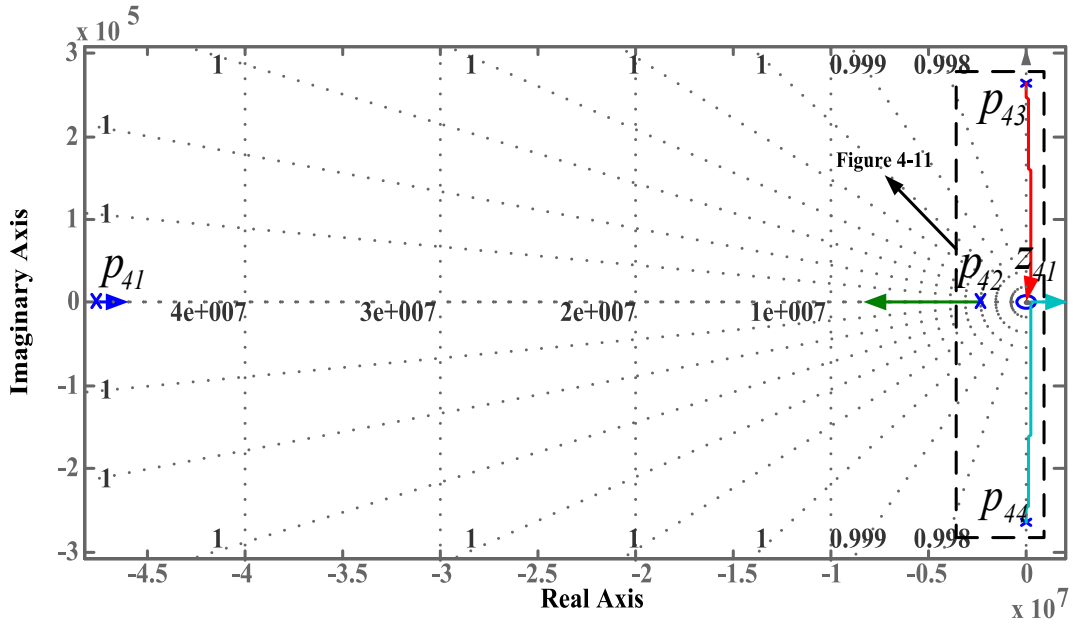

Figure 4-10: *Root-locus* plot for positive feedback loop using electrical output (overview)

The region of interest in figure 4-10 is amplified and presented in figure 4-11. As loop gain increases, the negative real pole moves away from the origin. After crossing the imaginary axis, the conjugate roots converge on the real axis. This movement, in the phase plane, signifies an unstable circular phase trajectory. The two conjugate roots intersect on the real axis and then move in opposite directions. One forms a pole-zero cancellation near the origin. The other positive real pole and the negative real pole dominate the system dynamics and lead to a change from a spiral phase portrait to a *saddle point* when the loop gain K is greater than 66.

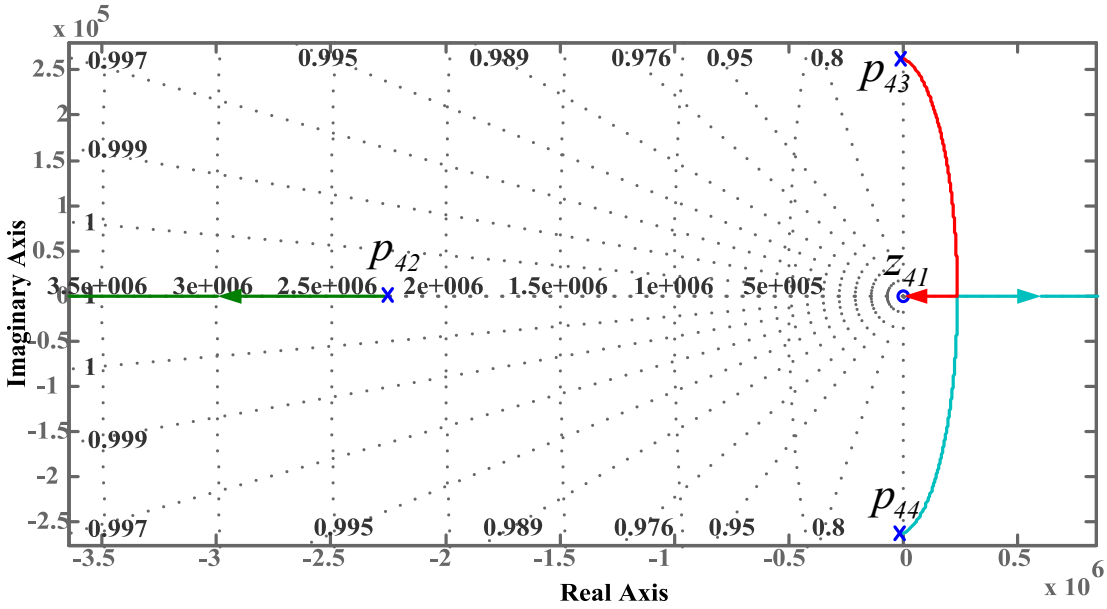

Figure 4-11: *Root-locus* plot for positive feedback loop using electrical output (focused view)

Clearly, the above root loci analyses illustrate that it is possible to achieve both the under-damped *stable focus* and *saddle point* for both acoustic and electric feedback approaches. However, the gain needs to be changed to achieve the required system dynamics when electric feedback is used.

4.2. Simulation Results

The following section describes the simulation results from the VSC system of figure 4-3. The *Simulink* simulation results presented are based on a model of the transducer illustrated in figure 3-3 a) with a resonant frequency of 40 kHz and a Q factor of around 55. The sampling frequency for the discrete VSC system is set at 4 MHz. Figures 4-12 and 4-13 demonstrate the outcomes when employing VSC compensation with the gain values of F, A, B and H tabulated in table 4-5.

This result can be compared with the response of the uncompensated transducer in figure 4-2 b) when the signal of figure 4-2 a) is applied using a linear amplifier of gain F.

F	A	B	H	c_{tran1}	c_{tran2}	R_{m4}
2	100	100	2	100 Hz	100000 Hz	100 Ω

Table 4-5: Values of the VSC system with acoustic signal feedback

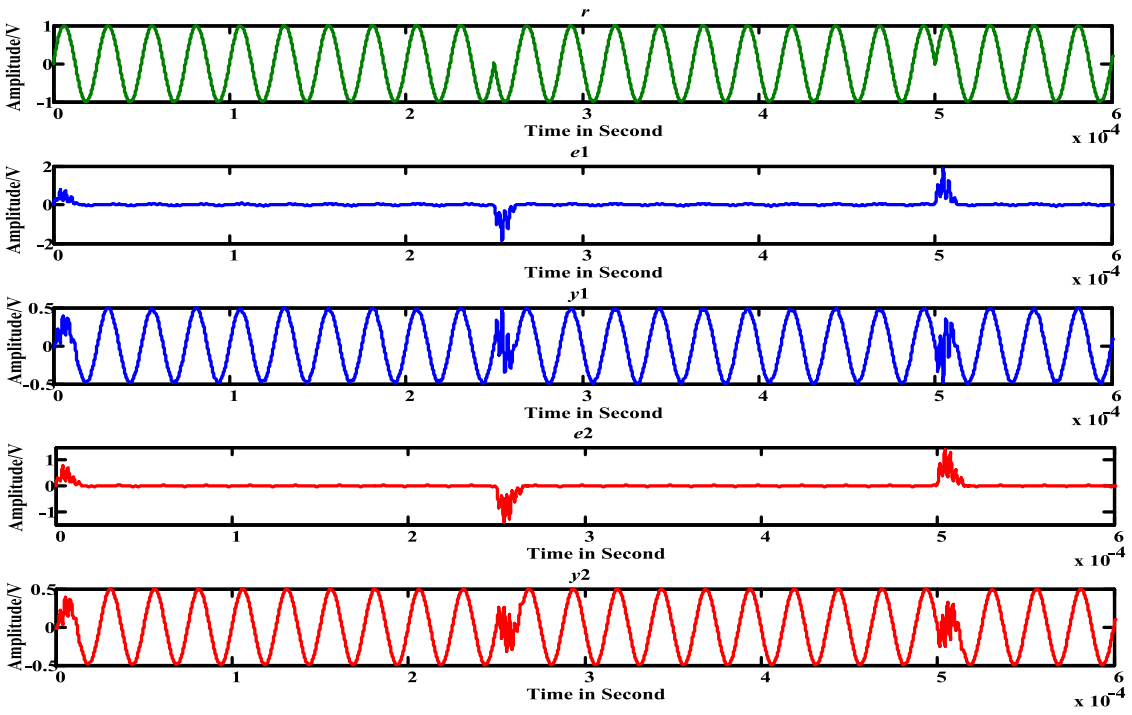

Figure 4-12: r: BPSK excitement (carrier: 40 kHz, symbol: 2 kHz) $e1$, $e2$: System error signal $y1$,$y2$: Compensated output with acoustic feedback

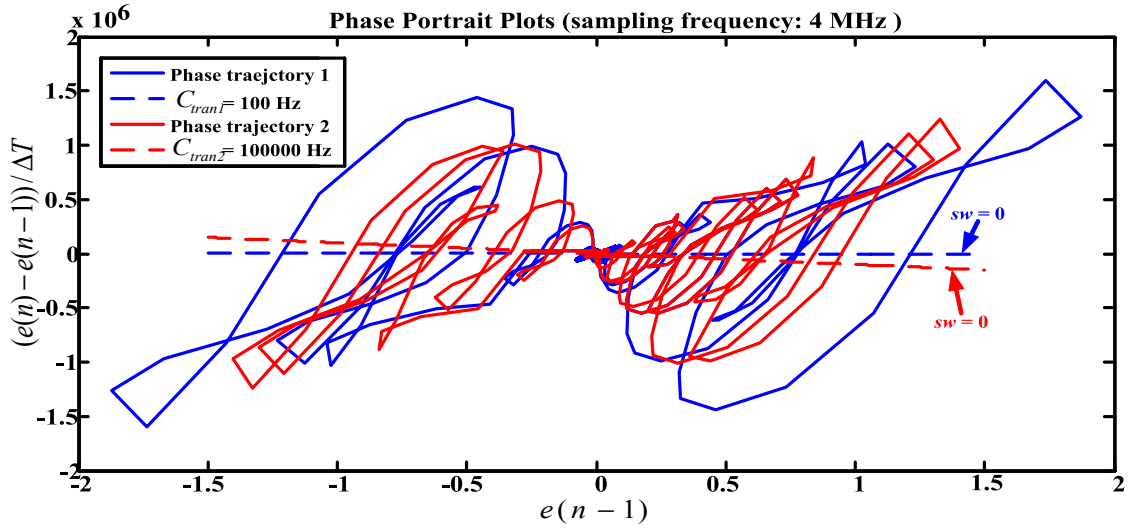

Figure 4-13: Phase portrait of the VSC system with transducer acoustic output as feedback signal

The loops along the *sw* illustrated in the phase portraits above were particularly noticeable when in *sliding mode* the trajectories from regions *I* and *III* passed through *sw* into regions *IV* and *II* respectively where they are switched back on themselves. Similarly trajectories from regions *IV* and *II* are switched back to regions *I* and *III* on crossing *sw*. The loops suggest the time constant, c_{tran}, chosen for the *sw* and the sampling frequency, $1/\Delta T$, in both simulations are too slow, because the delay in switching between the two feedback paths is allowing the phase trajectories to travel too far away from the *sw*. If higher sampling frequency is used, the magnitude of the loop will be smaller.

A set of time and phase responses are presented in figure 4-14 as an illustration of the effect of different sampling frequencies and *sw* constants on the transient dynamics of the overall system. It can be noticed that the loop amplitude about the *sw* is gradually reduced as the sampling frequency increases. Also, the switching frequency about the *sw* observed in the time responses in figure 4-14 increases as the *sw* becomes steeper.

F	A	B	H	c_{tran}, c_{tran1}	c_{tran2}
2	200	200	0.5	250000 Hz	450000 Hz
$1/\Delta T_1$	$1/\Delta T_2$	$1/\Delta T_3$	$1/\Delta T_4$	R_{m4}	c_{tran3}
4 MHz	8 MHz	10 MHz	20 MHz	1000 Ω	550000 Hz

Table 4-6: Parameters used in further simulations of VSC transducer using acoustic signal feedback

An interesting feature illustrated in the phase portraits of figure 4-14 is that the trajectory around the *sw* is immediately bounced back towards regions *I* and *III* after crossing *sw*. A large vertical displacement on phase plane suggests high speed movement. The speed of the vertical push of the *saddle point* phase trajectory is dominated by the speed of the real poles on the s-plane. If a low sampling frequency is selected, the next sample after a *sw*-crossing is detected can be a long way away from the *sw* before it turns back towards the *sw*. The sudden movements indicate positive feedback is sustained for the one sampling period until the next sample is noticed. Once it is switched to the negative feedback, it then plods back to the *sw* because the velocity for negative feedback dominated by the *stable focus* complex conjugate is slower. This feature does not simply vary with the change of the sampling frequency. It is the effectively resulted from the interaction between the sampling rate and the choices of feedback system root dynamics. The composite

phase portraits of figure 4-15 using the same test condition as those for figure 4-14 a) demonstrate that the *sw* gradient can be tailored to provide an anticipated response.

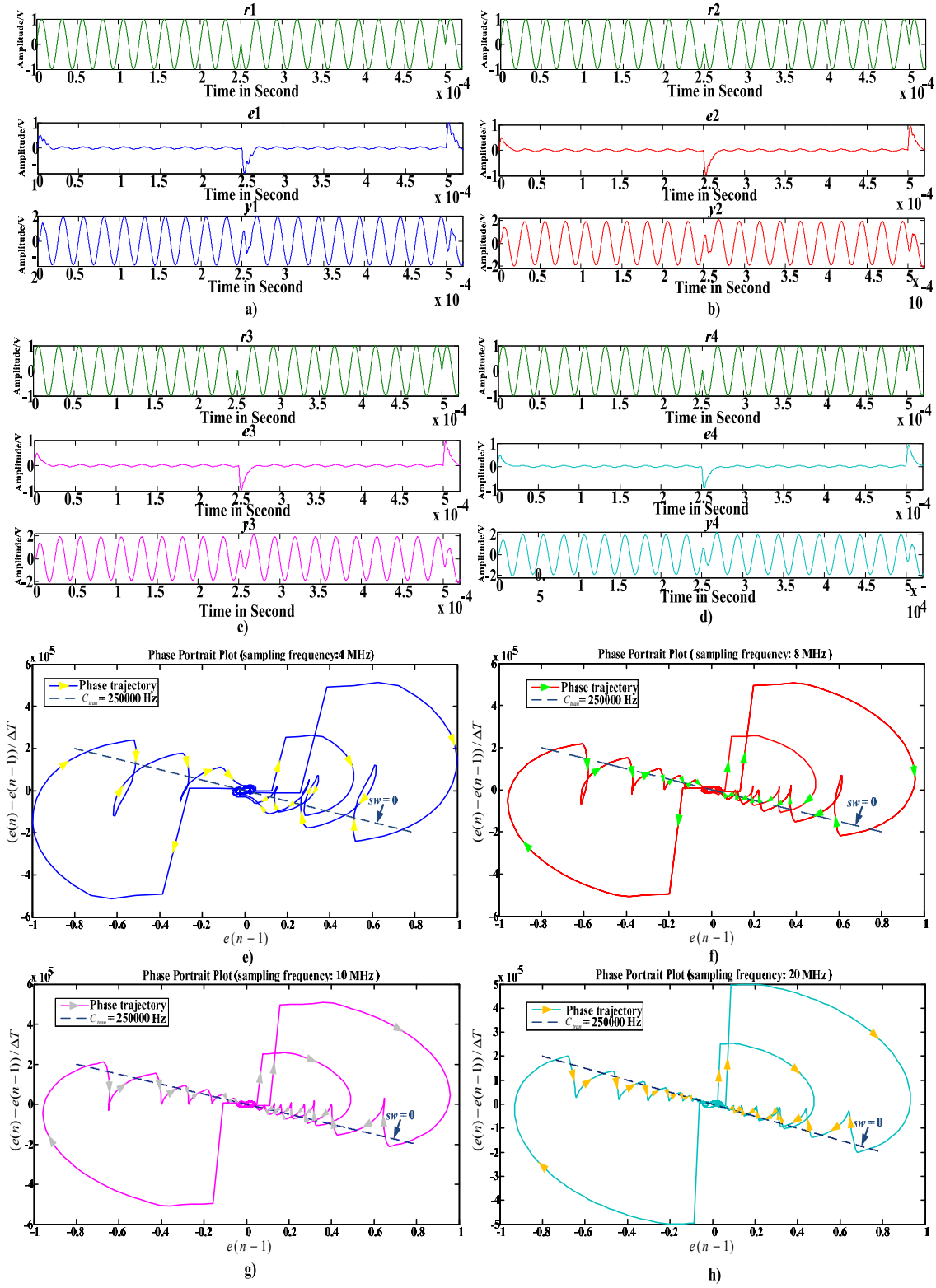

Figure 4-14: Illustration of the VSC system with different sampling frequency (acoustic feedback)

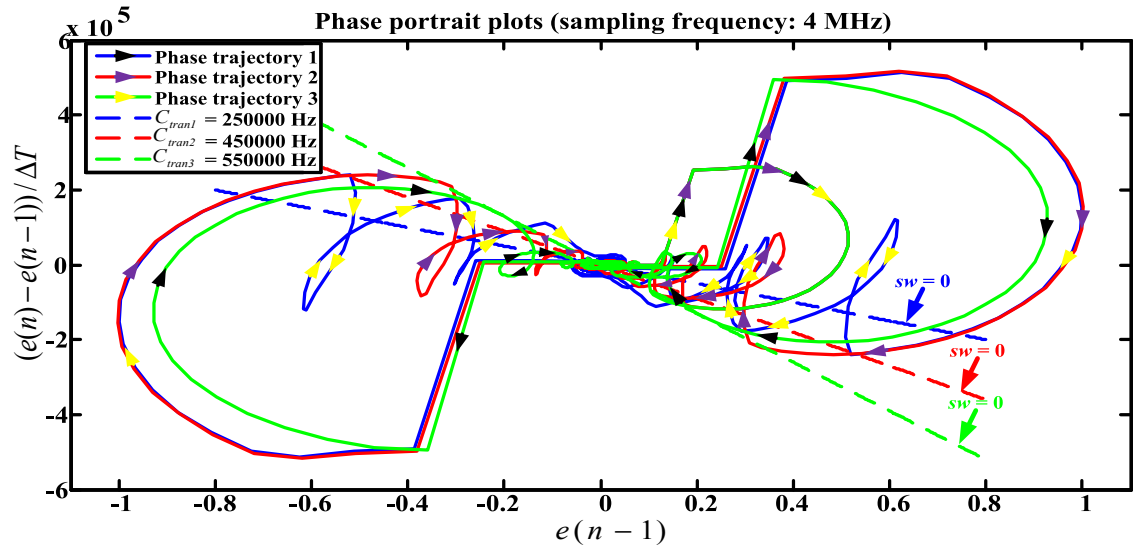

Figure 4-15: Illustration of the VSC system with different *sw* constants (acoustic feedback)

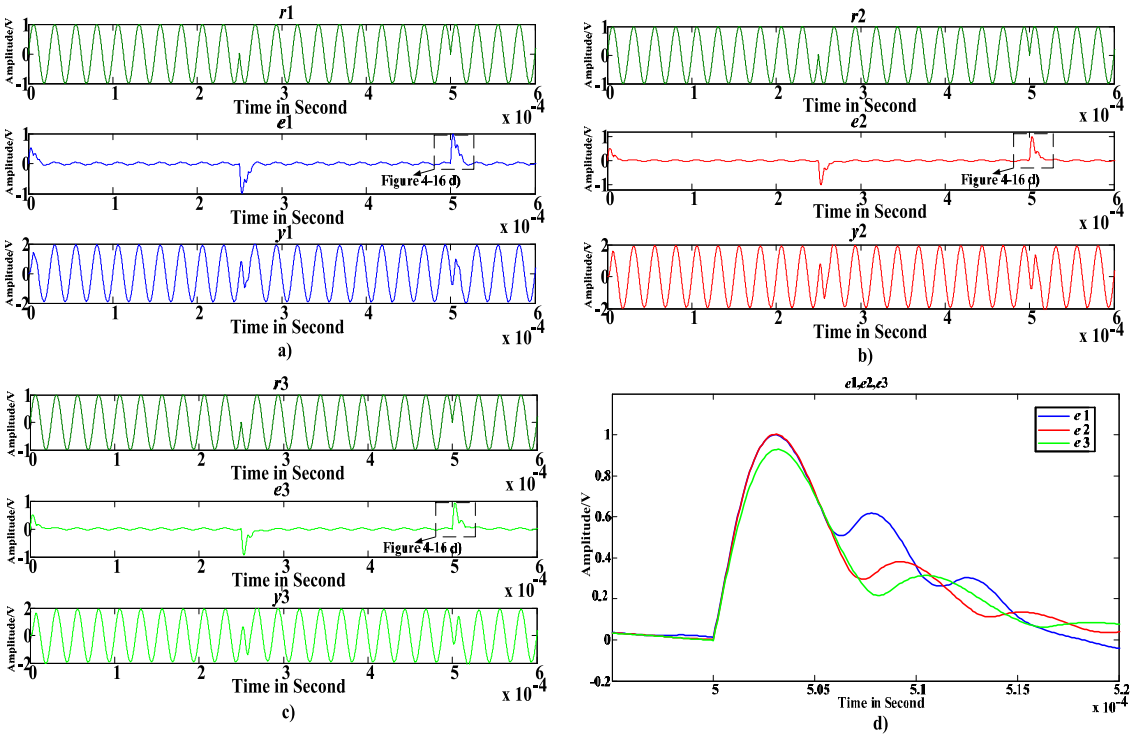

Figure 4-16: Temporal responses of the VSC system with different *sw* constants (acoustic feedback)

Simulations of the VSC control system using the electrical output sensing circuit, described in Subsection 4.1.3, are presented in figure 4-16 and 4-17. It can be seen that the VSC control system still operates satisfactorily to provide an output response with quick transient decay. The gain values for this simulation experiment are listed in table 4-3. The *sw* constant is varied to be 10000.

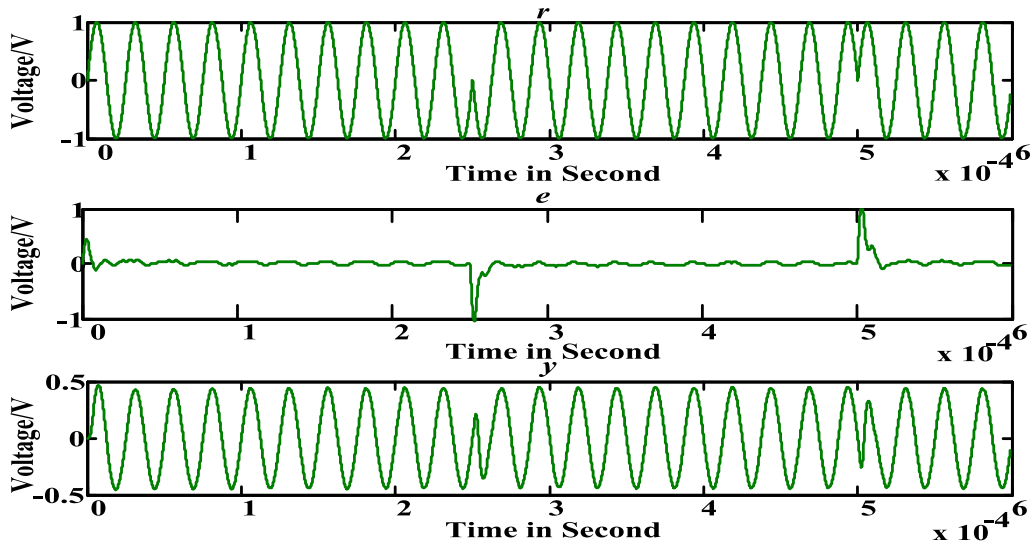

Figure 4-17: *r*: BPSK excitement (carrier: 40 kHz, symbol: 2 kHz) *e*: System error signal *y*: Compensated output with electrical feedback

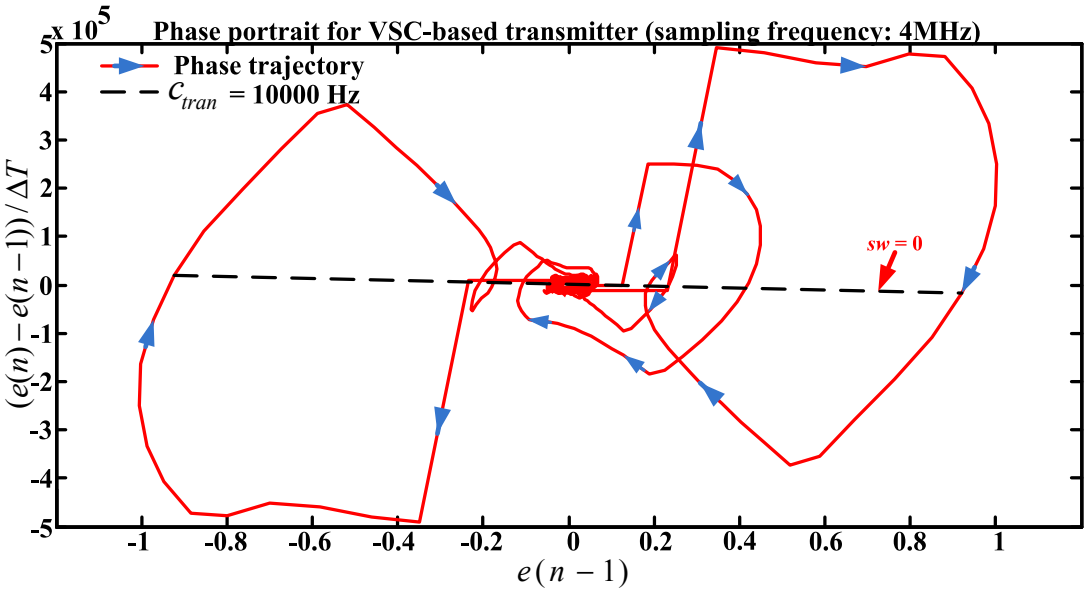

Figure 4-18: Phase portrait of the VSC system using electrical output as feedback signal

Further simulation results were conducted with alternative sets of parameters to evaluate the performance of the VSC system. Simulation outputs with various gain values and sampling frequencies used can be found in table 4-7 in Section 9.3 of the appendix. The simulated waveforms in figures 9-6 and 9-7 demonstrate that the proposed VSC transducer system can also produce acceptable transient responses with other sets of gain and *sw* parameters.

F	A1, B1	A2, B2	A3, B3	$1/\Delta T$
2	100	150	250	40 MHz
H	c_{tran1}	c_{tran2}	c_{tran3}	R_{m4}
175	100000 Hz	250000 Hz	450000 Hz	1000 Ω

Table 4-7: Parameter values used in further simulations for VSC system using electrical feedback

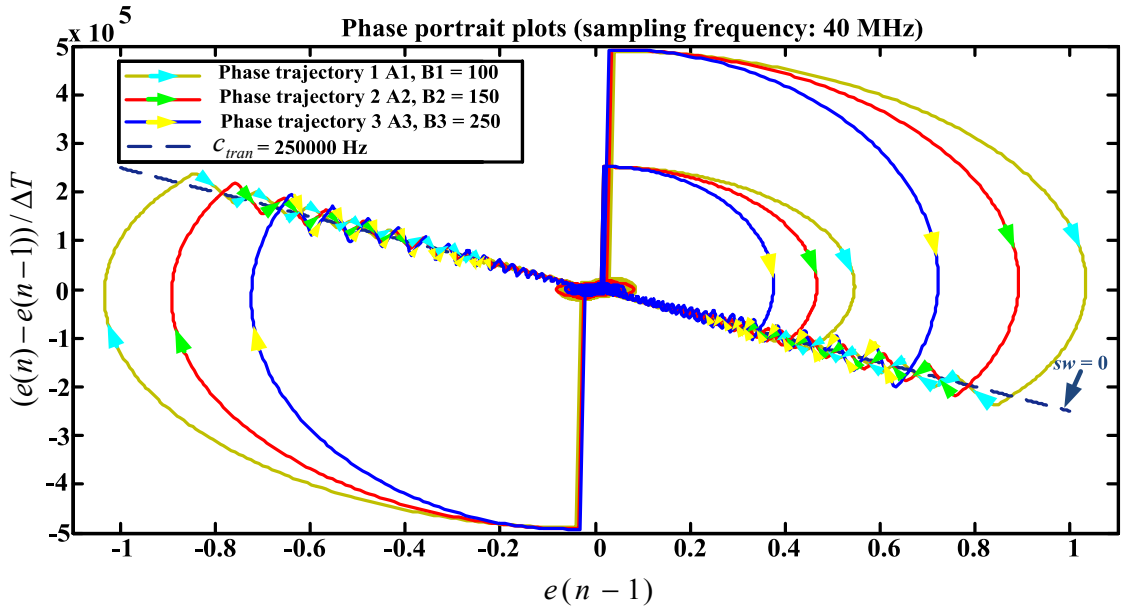

Figure 4-19: Illustration of the VSC system with different gain values (electrical feedback)

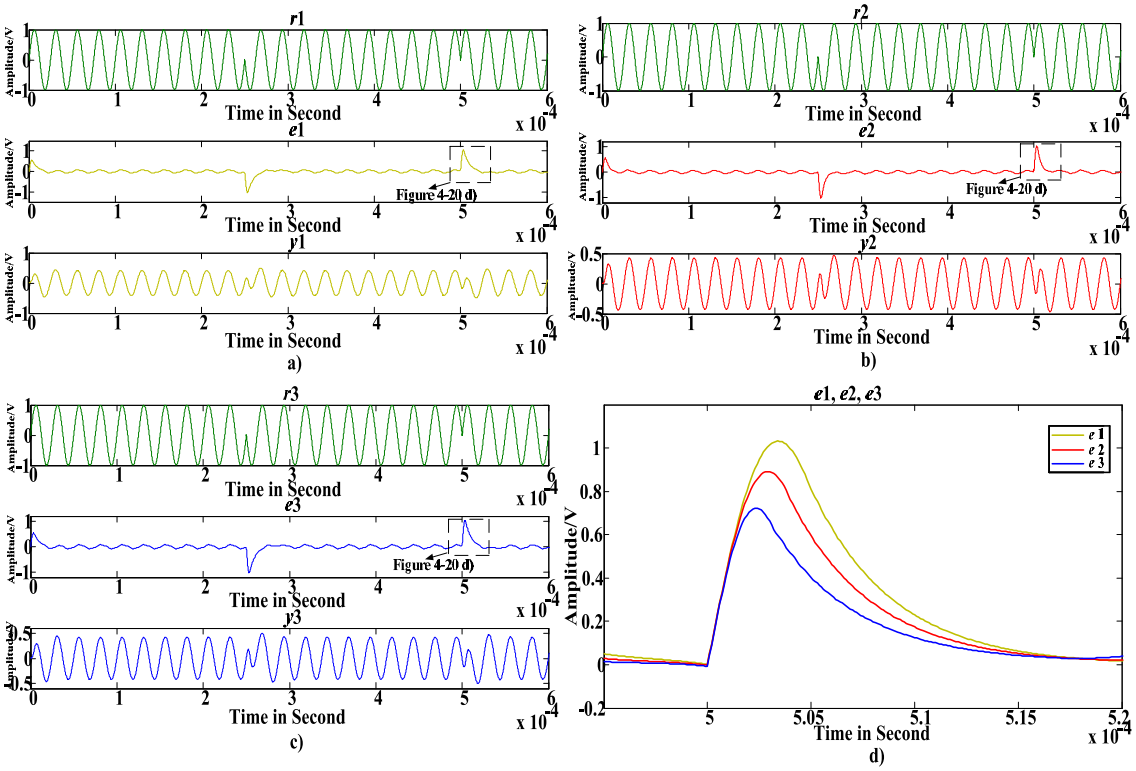

Figure 4-20: Temporal responses of the VSC system with different gain values (electrical feedback)

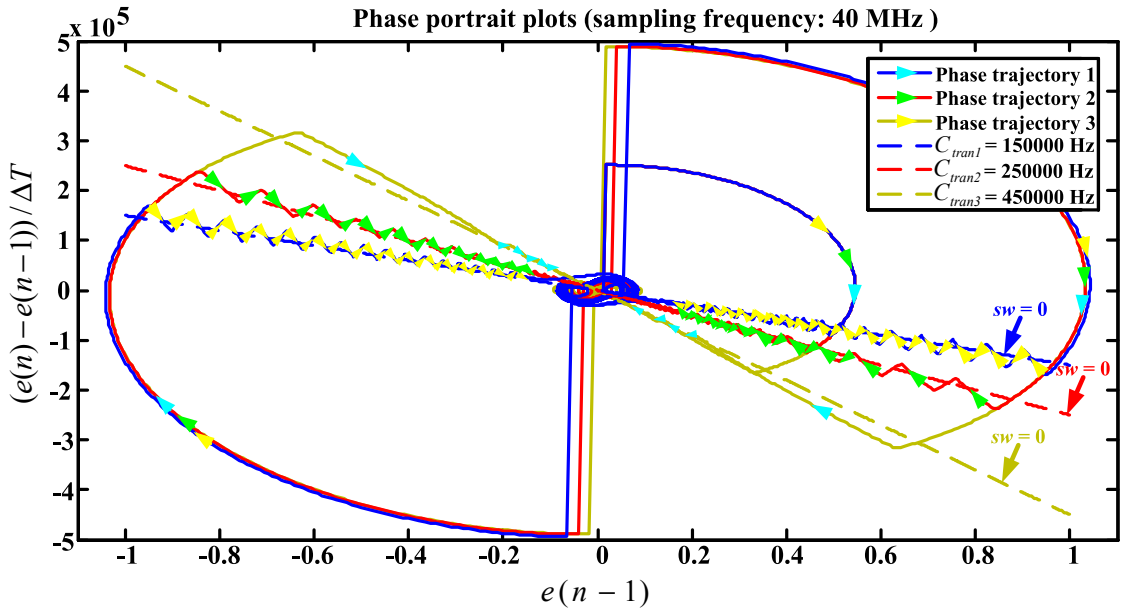

Figure 4-21: Illustration of VSC system with different *sw* constants (electrical feedback)

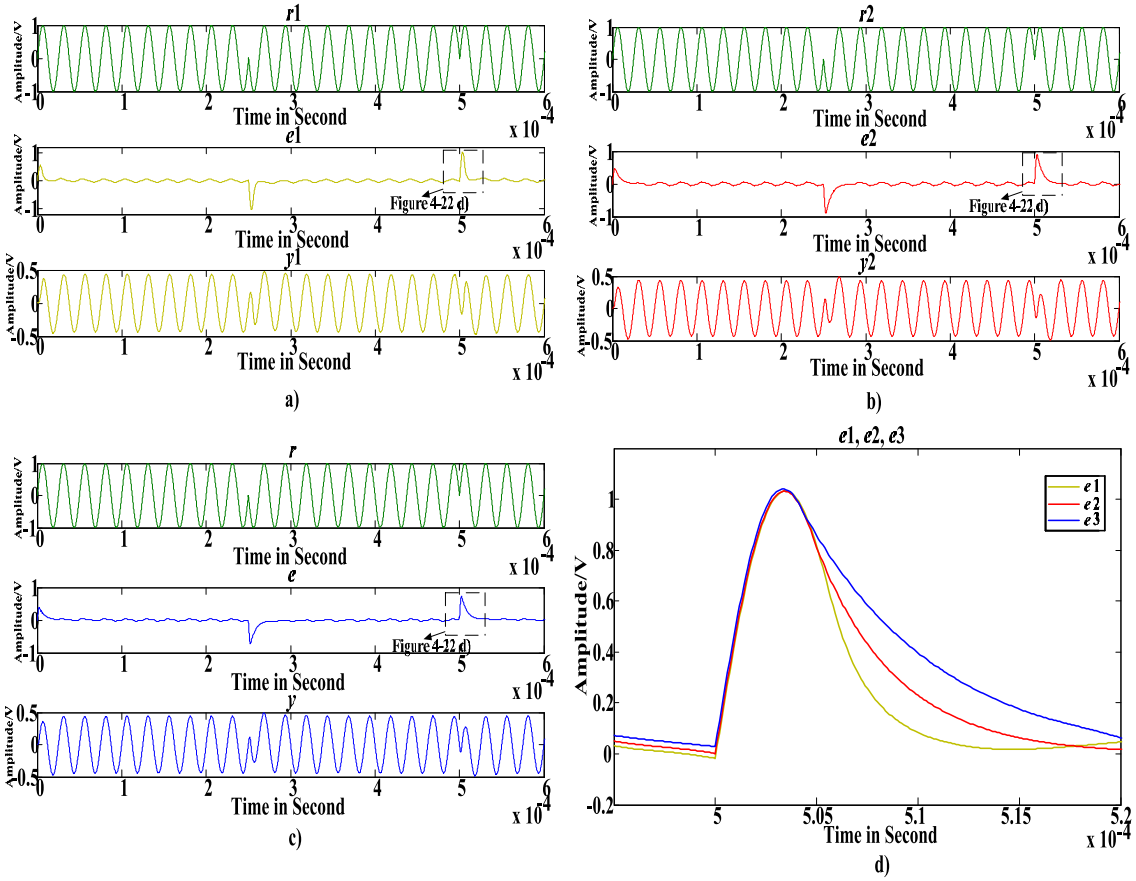

Figure 4-22: Temporal responses of the VSC system with different *sw* constants (electrical feedback)

4.3. Summary

This chapter has presented a design of an US transmission system using VSC control to reduce the duration of the transient response to phase switching. The initial design relied upon an idealised measure of acoustic feedback derived from the current in the series resonant branch of the transducer model. The simulated results for this system show that the time taken for a full change of phase in the transducer output could be reduced from approximately seven cycles of carrier to a maximum of half of a carrier cycle. The second realisable design replaced the idealised acoustic feedback with an approximate electrical measure. The overall performance of the second design was unaffected by this change although the higher order transient dynamics became more noticeable in the system's phase portrait.

Chapter 5.

VSC Ultrasonic Receiver

Chapter 4 presents a successful system configuration to decrease the transient response time of an ultrasonic (US) transmitter, which relies on the Variable Structure Control (VSC) technique. A communication system also requires a receiver capable of producing a matched response. The under-damped response of a conventional US transducer configuration limits the capacity of an US receiver. Applying VSC to the receiver, in a similar fashion as in the transmitter, is a possible method to produce a high capacity communications system. This chapter investigates a specific equivalent circuit model to produce a receiver with as little modification to the structure of the VSC compensator as possible. The full evaluation of the performance of VSC compensator used in Chapter 4 will be applied to the VSC-based receiver.

5.1. Configuration of VSC US Transmitter as Receiver

Before analyzing the application of VSC compensation to a receiving transducer, consider the simulated behaviour of the US transmitter transducer from Chapter 4 when it receives an acoustic signal similar to the waveform that it can emit.

Symbol	Description
F	Amplification to Demand Signal
G	Transfer Function of US Circuit Model
H	Gain Block of Feedback Signal
VSC	Discrete VSC algorithm
r	Demand Signal
y	Acoustic Input of Transducer
y^*	Electrical Output of Transducer Sensory Circuit
e	System Error between Fr and Hy^*
A, B	Negative and Positive Gain Blocks

Table 5-1: VSC system signals and transfer function definitions

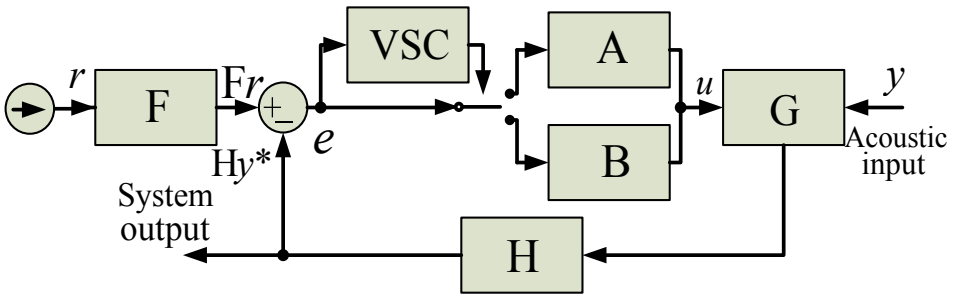

Figure 5-1: Block diagram of VSC US transmitter configured as receiver

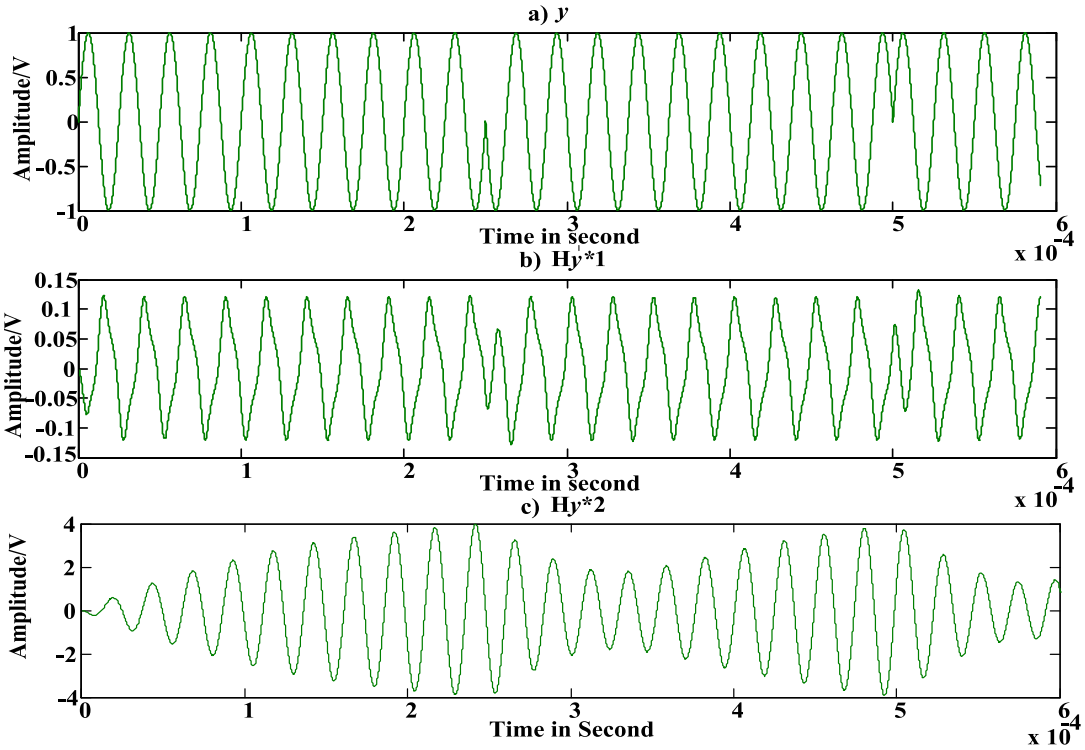

Figure 5-2: a) Simulated BPSK acoustic input signal *y* b) US receiver output signal, H*y**1, with VSC compensation c) US receiver output signal, H*y**2, without VSC compensation

The system configuration remains the same as shown in figure 5-1. When configured as a transmitter an electrical drive signal *r* is input. To use this system as a receiver *r* is set to zero (grounded) and the control system aims to minimise the mechanical movement of the transducer. An acoustic drive signal, as in figure 5-2 a), is applied to the transducer. The corresponding response of figure 5-2 b) is the measured transducer feedback output, H*y**1. The transients are quickly damped illustrating that the VSC-US transmitter can be also used as a receiver. For comparison, if the VSC feedback path is disconnected, the sensing unit output returns to a gently

damped ringing as illustrated in figure 5-2 c). A communication system based on transducers with this response would have a much lower capacity due to the time required to establish the correct phase.

As observed in figure 5-2 c), the uncompensated transmitter system, used as a receiver, yields an under-damped sinusoidal oscillation resonating around the carrier frequency of input US signal. The phase change of the open-loop system response is delayed compared to the 40 kHz BPSK signal with the bit rate of 2 kbps. These results demonstrate that the transmitting transducer model can be configured as a receiver and that VSC designed for transmission provides a marked increase in performance.

5.2. US Receiving System Model with Sensing Circuit

The following section will analyse the receiver circuit model in terms of the transfer function from acoustic input to electrical output.

5.2.1. Transducer System Transfer Function Analysis

The damped oscillations illustrated in figure 5-2 c) are due to resonance between the electronic and mechanical characteristics of the transducer, described in Subsection 3.1.3. The control system requires an error signal with which to determine the feedback signal. The error signal is the difference between the actual and desired response of the transducer. An error signal can be derived from the voltage across the electronic branch of the equivalent circuit model. However, this signal is inaccessible in a real transducer. Chapter 4 suggested an alternative feedback signal derived from an external sensing circuit that mimics the electronic branch of the circuit model, illustrated in figure 5-3 a). A block diagram of the sensing circuit working as receiver is given in figure 5-3 b). The unit has two inputs, one electrical and one acoustic, and an output derived from the sensing circuit, see figure 5-4 a). The transfer function of this model will be analysed in detail (See 9.2.2. for detailed transfer function derivations).

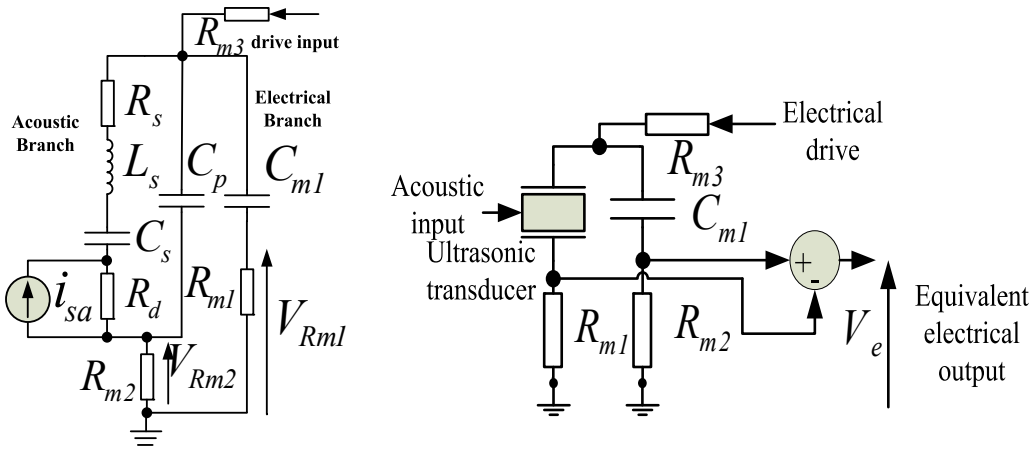

Figure 5-3: a) Receiver model with impedance matching path b) Circuit diagram for electrical equivalent sensor output

C_{m1}	R_{m1}	R_{m2}	R_{m3}
2100 pF	10 Ω	10 Ω	10 kΩ

Table 5-2: Values of the VSC system with electric equivalent feedback

The output of the receiver is assumed to be the sum of the outputs due to the electrical and acoustic inputs. The transducer model G is decomposed into two equivalent circuit models, I and C, for the corresponding sources. This separation is demonstrated in a block diagram in figure 5-4 b).

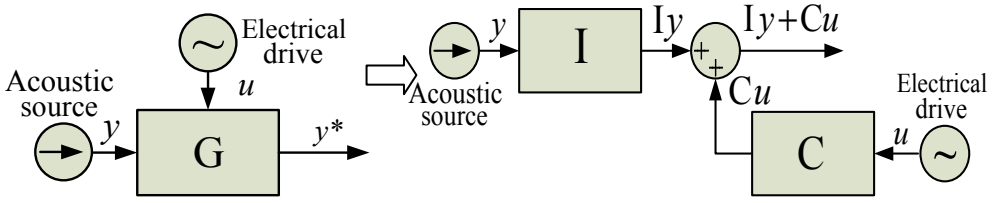

Figure 5-4: a) Receiving transducer with two inputs b) Separation of G in terms of two transfer functions

The forward path in figure 5-4 b) describes the receiving process of the transducer excited with an acoustic input. C*u* is the VSC compensation from the feedback path to suppress the movement of the transducer with a time constant defined by the *switching line* (*sw*). Since the piezo ceramic in the transducer stays static unless a compatible acoustic signal is received to excite it to vibrate, I*y* can, accordingly, be seen as the impact caused by a constant disturbance input and the suppression of the acoustic input is thought of as *disturbance rejection*.

n_{71}	n_{82}	n_{81}	d_{50},d_{60}
6.1×10^{20}	1.56×10^{19}	3.7×10^{23}	4.7×10^{29}
d_{54},d_{64}	d_{53},d_{63}	d_{52},d_{62}	d_{51},d_{61}
6×10^{6}	2.8×10^{14}	1.07×10^{19}	2×10^{25}

Table 5-3: Coefficients of transfer functions C and I

$$\mathrm{G_c} = \frac{V_e(s)}{V_{sd}(s)} = \frac{n_{71}s}{d_{54}s^4 + d_{53}s^3 + d_{52}s^2 + d_{51}s + d_{50}}. \tag{5.1}$$

$$\mathrm{G_I} = \frac{V_e(s)}{I_{sa}(s)} = \frac{n_{82}s + n_{81}}{d_{64}s^4 + d_{63}s^3 + d_{62}s^2 + d_{61}s + d_{60}}\,\Omega. \tag{5.2}$$

The transmitter VSC compensation is designed to force the error transient dynamics of the transducer using high loop gains [101]. The higher the switching gains, the stronger is the cancellation of a received acoustic input. Consequently, the forceful switching control used to achieve the desired transient response reduces the magnitude of the sensing unit response to an acoustic input. On the other hand, the receiver is expected to contribute an output signal that has sufficient amplitude for further processing. To reach a compromise between a tolerable disturbance signal magnitude and effective damping of the transient response, the tuning of switching gains for the receiving system needs to balance these two considerations.

5.2.2. Performance Evaluation of Dynamic Compensation Gain

The positive and negative feedback gains of the receiver system can be simultaneously adjusted by changing the driver output impedance, R_{m3}. This adjustment allows the transducer model dynamics to be flexibly controlled. The impact of modifying R_{m3} on the sensor unit output signal magnitude is demonstrated by the two superposed time and phase diagrams of figures 5-5 and 5-6. The green curve in time diagram features a signal magnitude 5 times greater than the blue waveform due to the increase of R_{m3} from 2000 to 10000.

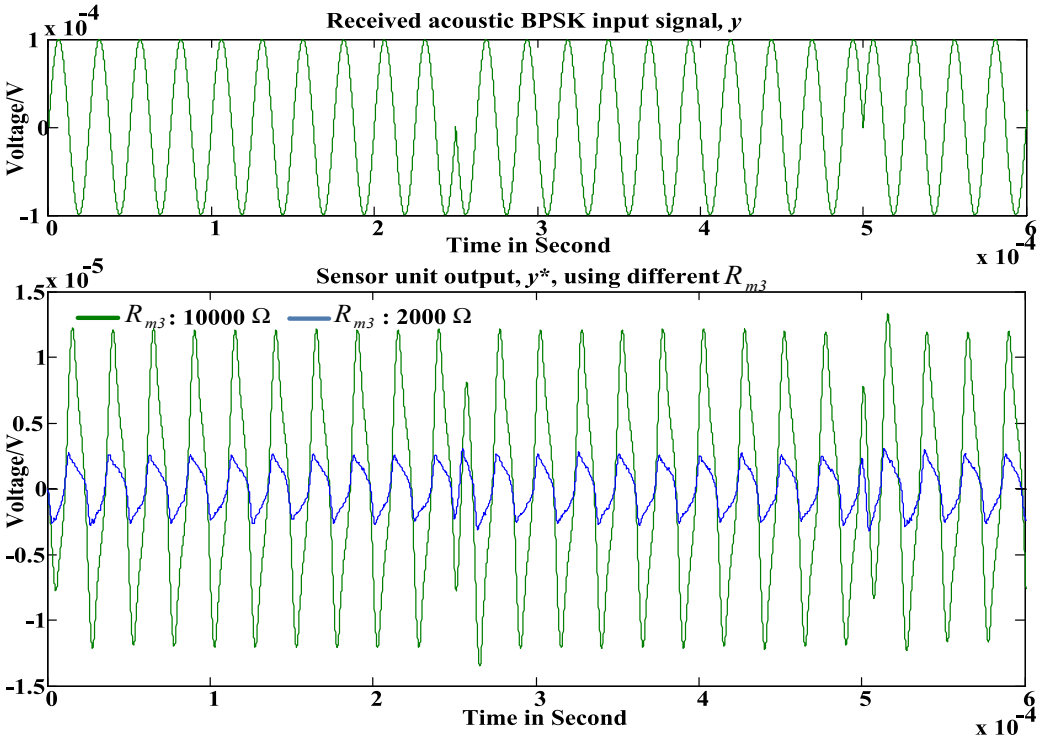

Figure 5-5: Composite time domain signals with different degrees of suppression

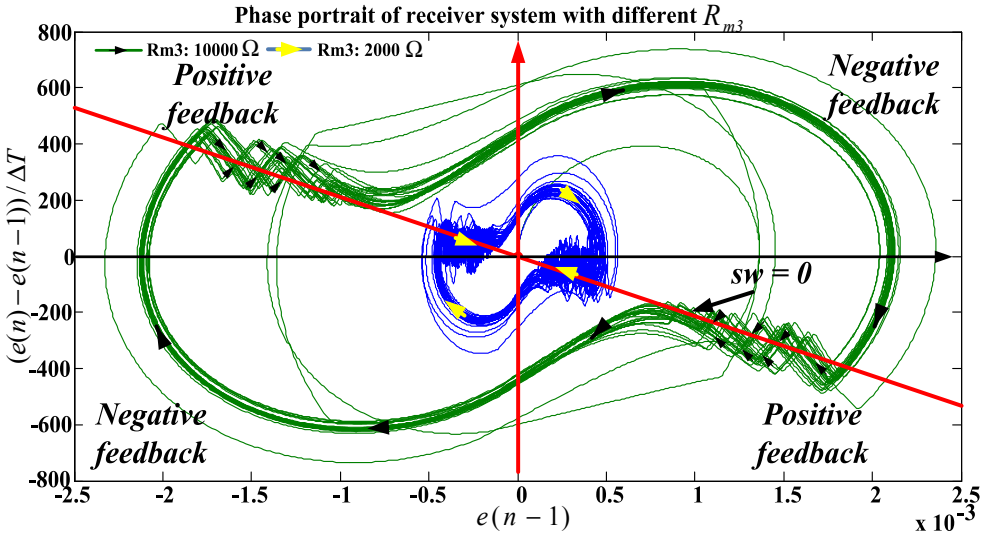

Figure 5-6: Composite phase portraits with different degrees of suppression

This analysis indicates that the transfer function of transducer model G can be decoupled into its Norton equivalences, I and C. The application of VSC switching control to the decoupled system configuration is interpreted as the rejection of the received acoustic input. In the following section, this transfer function analysis is extended to investigate the root trajectories of the system transfer function with positive and negative feedback controls.

5.2.3. *Root-Locus* Analysis

Figure 5-7 shows the full block diagram of the US receiver. An acoustic input is countered by a dynamical feedback control system and the control signal yields the output. The transducer model can be altered into figure 5-8 by decomposing block G as explained in the Subsection 5.1.2. As the electrical drive input *r* is set to zero, the error signal, *e*, may be simplified from $(\mathrm{F}r - \mathrm{H}y^*)$ to $-\mathrm{H}y^*$. The block diagram of the closed-loop system figure 5-7 is simplified into a standard control system structure illustrated in figure 5-8 with positive and negative gains in feedback path.

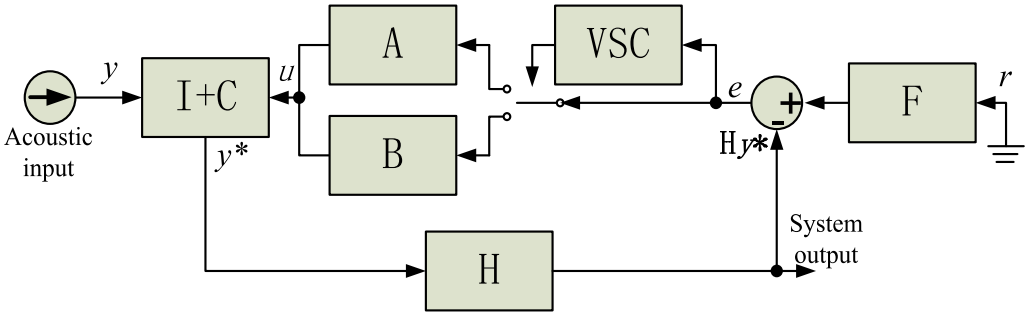

Figure 5-7: Block diagram of the VSC receiver system

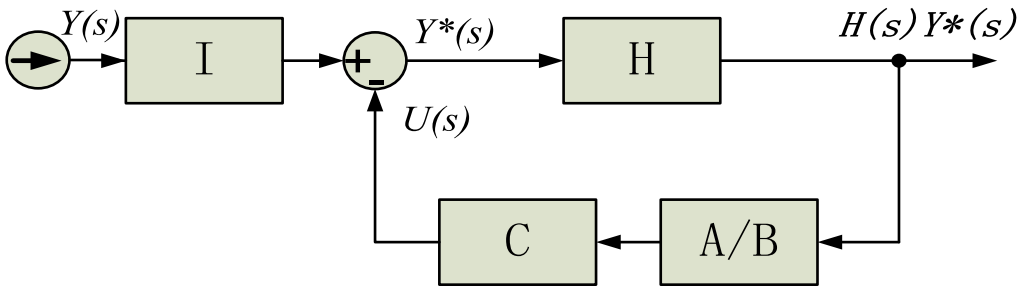

Figure 5-8: Simplified block diagram of the VSC receiver system

The closed-loop transfer functions of the control system in figure 5-8 can be individually written for the negative feedback configuration, C, H, A and I and the system with positive feedback, C, H, B and I. As introduced in Chapter 4, these two proportional control systems can produce the required phase portraits only if their transfer functions contain dominant characteristic roots. For negative feedback, dominant complex conjugate roots correspond to *Stable focus* phase portrait and two dominant real roots (one negative pole and one positive pole) implicates a *saddle point* phase portrait for the realisation of a positive feedback. The decision to apply negative or positive

feedback is determined by the instantaneous position in the phase portrait as illustrated in figure 5-6. Feedback is switched when a *sw* is crossed. The *switching line* is defined by $sw = 0$ where:

$$sw \equiv \big(e(n) - e(n-1)\big)/\Delta T + c_{tran} * e(n-1). \tag{5.3}$$

For the results shown in this chapter, the sampling frequency, $1/\Delta T$, is chosen to be 40MHz. In order to determine if the proposed systems can achieve the desired system dynamics, the *root-locus* diagrams are plotted individually using the open-loop transfer functions (5.4, 5.5) for each feedback system. The characteristic roots of the open-loop transfer function are listed in table 5-4.

$$\mathrm{TF}_{cln} = \frac{\mathrm{A(s)I(s)}}{1-\mathrm{A(s)C(s)H(s)}}, \mathrm{TF}_{clp} = \frac{\mathrm{B(s)I(s)}}{1+\mathrm{B(s)C(s)H(s)}}. \tag{5.4,5.5}$$

p_{51},p_{61}	p_{52},p_{62}	p_{53},p_{63},p_{54},p_{64}	n_{91},n_{101}
-4.7×10^7	-0.23×10^5	$(-0.07 \pm 2.68i) \times 10^5$	$\pm 9.01 \times 10^{18}$
A	B	H	$1/\Delta T$
900	900	175	40MHz

Table 5-4: Coefficients of system open-loop transfer function ACH and BCH

$$\mathrm{TF}_n = -\mathrm{AG_c(s)H(s)} = \frac{n_{91}s}{(s-p_{54})(s-p_{53})(s-p_{52})(s-p_{51})}. \tag{5.6}$$

$$\mathrm{TF}_p = \mathrm{BG_c(s)H(s)} = \frac{n_{101}s}{(s-p_{64})(s-p_{63})(s-p_{62})(s-p_{61})}. \tag{5.7}$$

The *root-locus* diagrams using the open-loop transfer function of each system are plotted individually to inspect if the designed systems can achieve selected system dynamics.

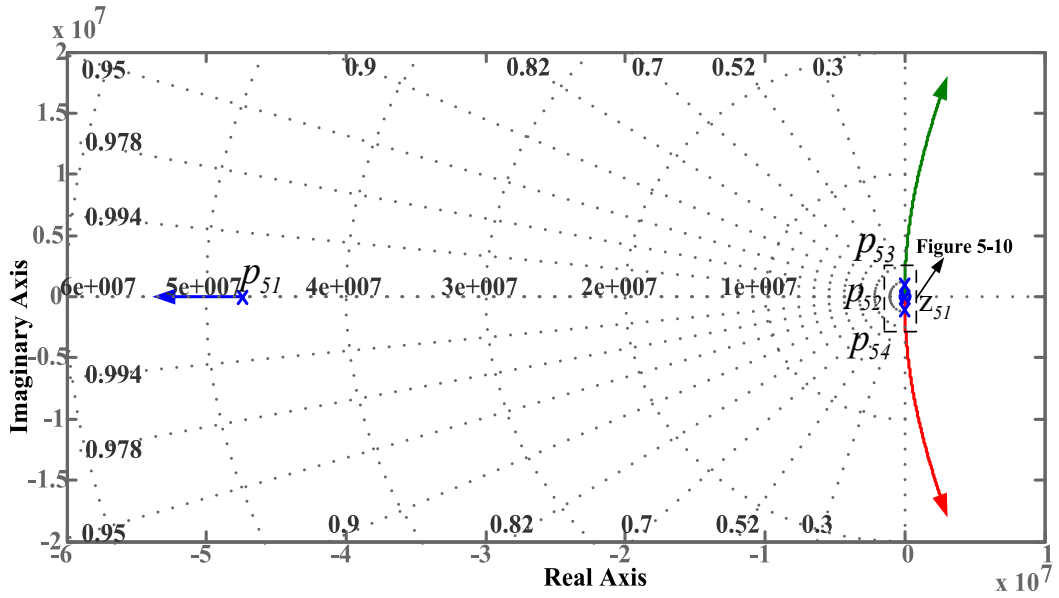

Figure 5-9: *Root-locus* plot of negative feedback loop (overview)

The roots of the characteristic equation of the open loop transfer function are listed in table 5-4. Figure 5-9 shows an overview of system root trajectories for negative feedback system described in (5.4). Since the location of a negative real pole is far from the origin, the system dynamic is dominated by the complex roots and the negative real pole near the origin. Although the general shape of the *root-locus* suggests an unstable oscillatory system dynamic governed by the two expanding complex root loci, a focused view of figure 5-9 unveils that a stable system configuration can be obtained if the feedback gain is selected within a certain range.

Figure 5-10 demonstrates that the initial locations of the complex conjugate pair are close to the origin, which reflects a system dynamic on the phase plane similar to a decayed inward spiral. As the loop gain sweeps, the complex roots produce symmetrically a pair of curvilinear traces approaching towards unstable region of the s-plane. Before passing through the imaginary axis, the velocity of the inward spiral phase trajectory gradually slows down since the complex roots move away from the origin. To realise *stable focus* system dynamic the dominant conjugate pair should remain within the stable region of Laplace plane and the loop gain should be smaller than K = 700000. After crossing through the imaginary axis, the direction of the spiral phase portrait is reversed and becomes an *unstable focus*.

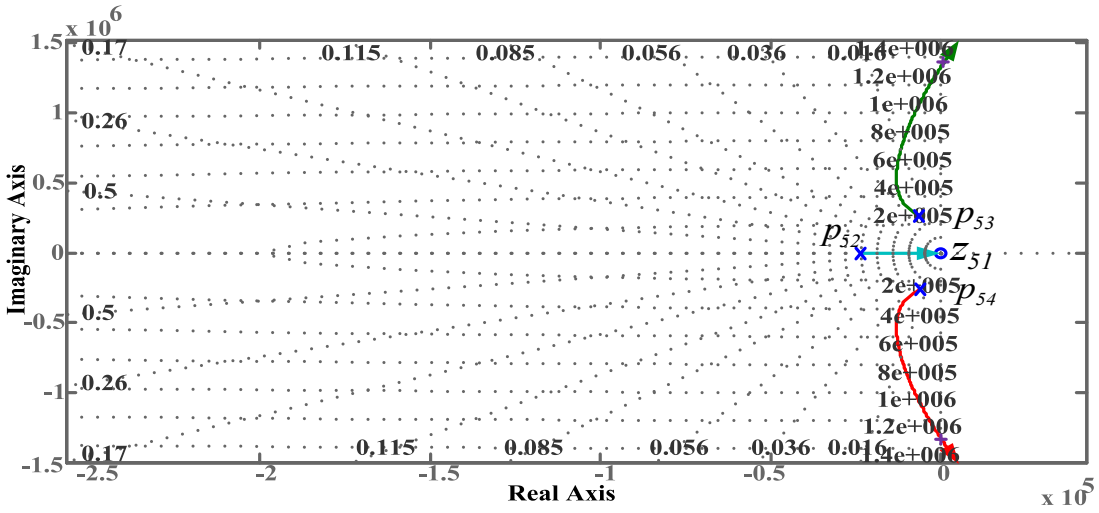

Figure 5-10: *Root-locus* plot of negative feedback loop (focused view)

The *root-locus* plot for the positive feedback system configuration, as depicted in figure 5-11, demonstrates root loci in both stable and unstable regions. In the stable region of Laplace plane, two root trajectories come close to each other but separate after intersecting at $(-3.2 \times 10^7, 0)$. The roots densely placed around the origin are dominant and the corresponding root loci are as shown in figure 5-12.

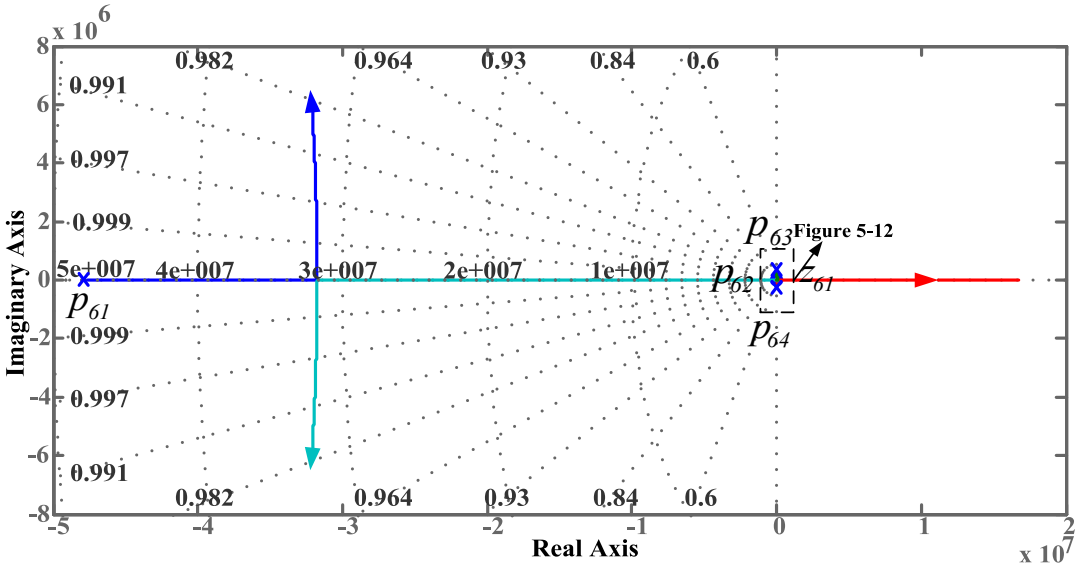

Figure 5-11: *Root-locus* plot of positive feedback loop (overview)

The behaviour of the dominant roots can be observed in figure 5-12. The initial positions of the conjugate roots are located in the stable region. As the loop gain starts to increase, the root trajectories of this conjugate pair slide towards the real axis and meet at the break-in point of

$(0.8 \times 10^5, 0)$. Then one pole moves to the zero at the origin. The other pole shifts longitudinally to be more unstable.

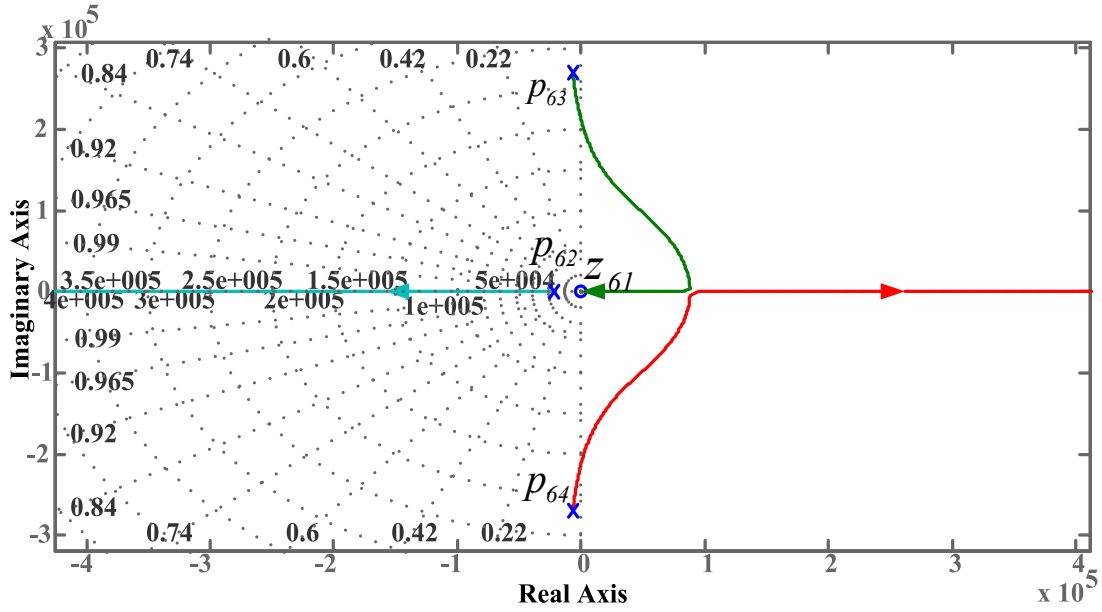

Figure 5-12: *Root-locus* plot of positive feedback loop (focused view)

The complex roots illustrated in figure 5-12 correspond to a spiral phase locus that spins inward. As the loop gain rises, these two roots loci will cross the imaginary axis. On phase plane, the direction of the inward spiral is reversed and become an unstable circular phase trajectory. If the gain keeps increasing, the trajectories of conjugate pair are broken to become two real poles at the intersection on real axis where the loop gain K = 47250. The separation of these two poles along the real axis suggests a change of phase trajectory from *unstable focus* to *saddle point.* One real pole moves towards a system zero at the origin. The other real pole travels along the real axis to become more unstable and coalesces with a negative real pole to form a dominant *saddle point* phase trajectories.

5.3. Simulation Results

The response of the VSC-based US receivers with variation of *sw* condition is demonstrated through a group of time and phase domain trajectories. The time constant, c_{tran}, defined in (5.3) is adjusted to tune the slope of *sw*. The second and third rows of Figure 5-13 are the resultant temporal waveforms, measured at the system output of figure 5-7. In the phase plane, it can be seen that the two phase trajectories follow the *switching lines* and converge towards the origin.

This distinctive motion of system dynamics repetitively sliding along *sw=0* is known as the *quasi-sliding mode* [102]. The adjustment of c_{tran} in the *sw* condition allows flexible control of the speed of convergence of the transient response.

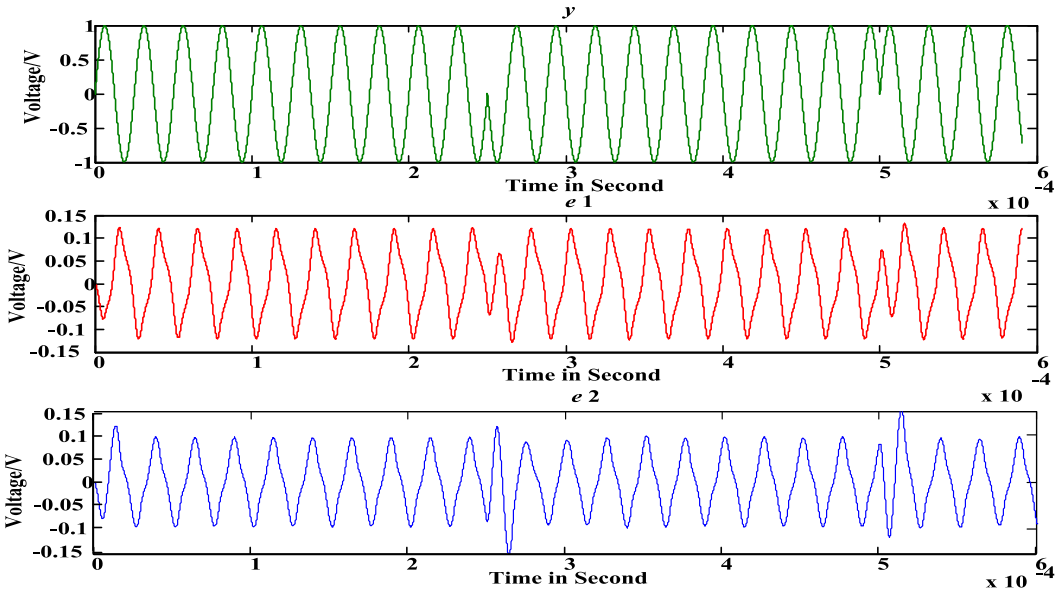

Figure 5-13: *r*: BPSK excitement (carrier: 40 kHz, symbol: 2 kHz) *e* 1, *e* 2: Electrically compensated outputs with associated with *sw* 1 and *sw* 2 respectively

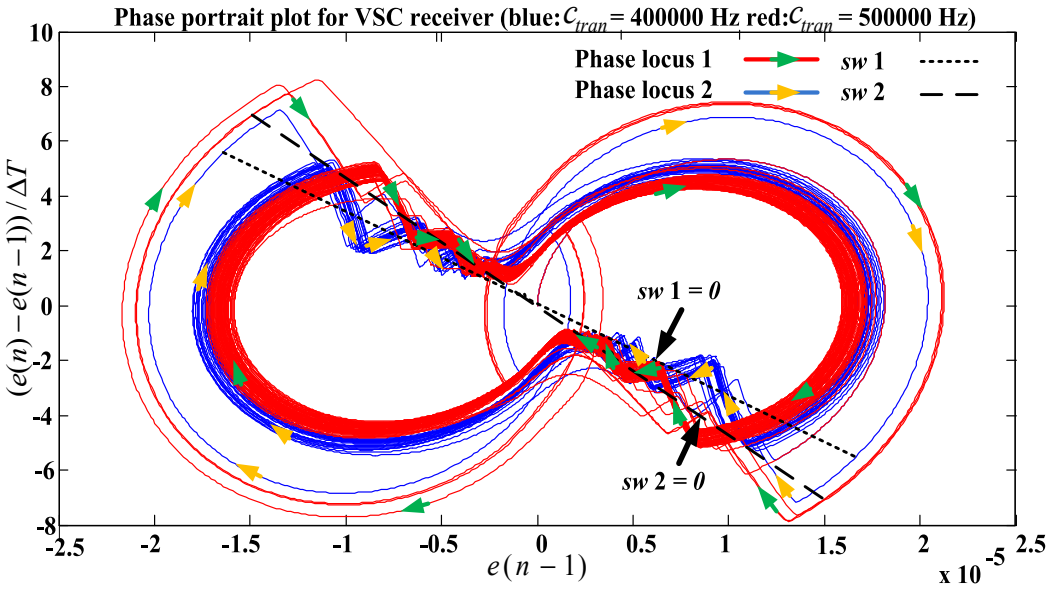

Figure 5-14: Composite phase portraits of VSC system with different *sw* conditions

A simulated acoustic BPSK input signal with Additive Gaussian White Noise (AGWN) at a Signal to Noise Ratio (SNR) of 10 dB was injected into the VSC-based receiver to test its

capability when the received signal is immersed by noise. The system response of VSC receiver shows that the controlled output still yields immediate phase switching and is unaffected by the input with noise because of the transducer's frequency selectivity. Although the unfiltered noise causes irregular velocity estimations on the phase portrait, the phase trajectory converges satisfactorily towards the origin in spite of the additive noiser.

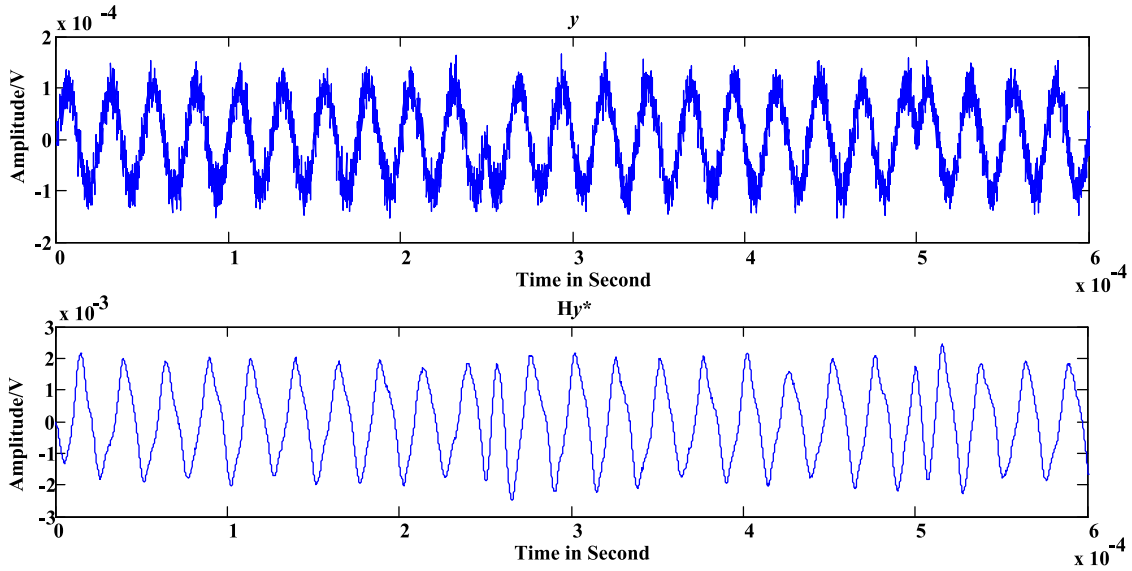

Figure 5-15: Simulated input with AGWN noise of SNR 10 dB and VSC receiver output response

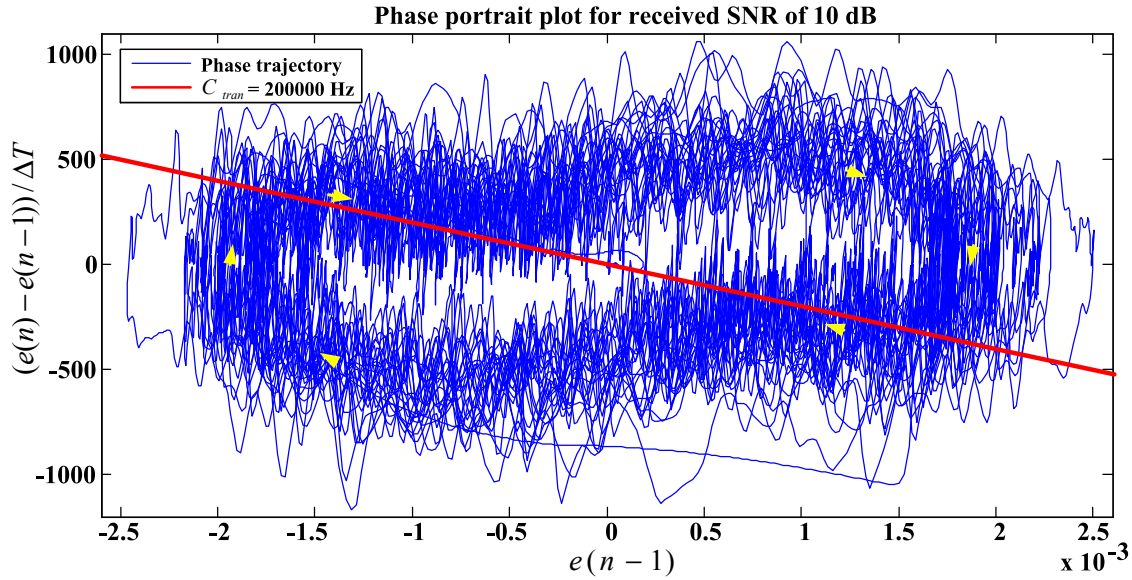

Figure 5-16: Phase portrait of VSC receiver with noise input

5.4. Discussion

The above simulation results demonstrate that the receiving transducer can be actively damped to respond promptly to the phase change of acoustic stimulus coming into the receiver. A controlled transducer has two inputs as shown in the circuit model analysis in Subsection 5.2.1. On the one hand, there is a transfer function to represent the acoustic to electrical energy conversion and, on the other hand, the same network is stimulated by the electrical drive that provides the compensation process. The interaction between these two inputs allows the transducer to produce a damped response. The feedback signal becomes a measure of the actual response of the transducer to an external stimulus while being actively damped. The only issue is that the VSC compensation is designed to vigorously reduce the error to zero but part of this error is the response to external stimulus so the level of compensation drive has to be moderated to allow sufficient amplitude of received signal to be obtained. Therefore, the choice of driver gain that governs the amplitude of receiver output while the gradient of the *sw* governs the degree of damping. Naturally this causes certain levels of damping to be unavailable because high feedback gains cannot be used to hold the transient response on *sw*. This functionality has been demonstrated in the Subsection 5.2.2.

5.5. Summary

An US communication system based on BPSK modulation requires a transmitting transducer that can quickly switch its acoustic output between the two phases. US transducers have an under-damped, oscillatory transient response. A transducer-VSC feedback system was described in Chapter 4 that achieves very rapid switching. To communicate with this signal it is necessary to have a receiver transducer that can quickly identify the phase of the received acoustic signal. In this chapter we have presented an US receiver, matched to the transmitter developed in Chapter 4. The same VSC feedback system is used to minimise physical oscillations within the receiver transducer. The detected signal is derived from the feedback control signal produced by the VSC system. The proposed transmitter-receiver combination has the potential to yield a 40 kHz US communications system with capacities of more than 20 kilo bits per second (kbps).

Chapter 6.

Implementation of VSC Ultrasonic System

The design of transient compensators using a discrete Variable Structure Control (VSC) algorithm, for both the ultrasonic (US) transmitter and the receiver, has been introduced in the preceding two chapters. So far it has been assumed that the performance of the transient compensator is unconstrained by system parameters such as the numerical precision of measurements and calculations and sampling frequency. This chapter will consider a physically realised VSC transducer system. This platform uses an analogue computer-based transducer circuit model working at a lower frequency of 1.75 kHz, to emulate the analogue circuits. It also investigates the potential problems encountered when using a microcontroller with a fixed-point number representation.

6.1. System Hardware Platform Specifications

Figure 6-1 is the block diagram of the implemented VSC transmission system. The functional block definitions of the real system are listed in the table 6-1. This illustrative design has both analogue and digital subsystems. In the analogue part, F and H are gain amplifiers for the input signal r and feedback signal y^*. Blocks A and B are the negative and positive feedback drivers respectively. Block M is the transducer output measurement circuit. Switching between the positive and negative feedback system structures is performed by the analogue switch of block S. The digital Advanced RISC Machine (ARM) processor is used to execute the control algorithm and generate the decision output to switch the system structure. It uses an on-chip Analogue-to-Digital Converter (ADC) to acquire sampled data upon which is used to base the switching decision. The introduction will start from the analogue subsystems.

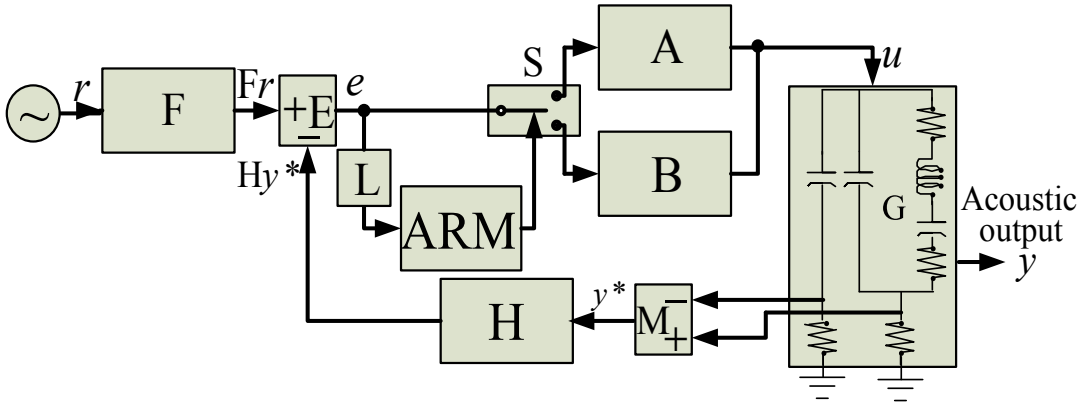

Figure 6-1: System block diagram of illustrative design

Symbols	Physical Devices
ARM	32-bit ARM7 Microprocessor
G	Analogue Computer-based Transducer Circuit Model
A, B	Single-ended Driver for Positive and Negative Feedbacks
F, H	Gain Amplifiers
E	The Differential Amplifier
S	Analogue Switch
L	Voltage Level Shifter

Table 6-1: VSC prototype system block definitions

6.2. Analogue Circuitry

This section introduces the analogue circuit designs for both forward and feedback paths of the VSC control system. Four circuits will be described: the transducer model, the switcher-based driver, the transducer output measurement and the system error detection. This physical system is designed to investigate the analogue circuit implementation of those functional blocks and to test and verify the simulations of Chapters 4 and 5.

6.2.1. Transducer Circuit Model

The structure of the circuit model configured for implementing the VSC compensation system has been introduced in Chapter 4. This circuit model has the ability to modify the transducer dynamics by tuning the value of individual circuit components. The resonant frequency of the transducer serial branch is primarily dictated by the inductance L_s and the capacitance C_s and can be determined using (6.1).

$$f_r = \frac{1}{2\pi\sqrt{L_s C_s}}. \tag{6.1}$$

In practice, the precision of tuning this frequency is affected by two major factors. One is the error tolerance of actual circuit components; the other is the limited choice of fixed-value electronic component parameters. For a circuit model resonating around 1.75 kHz, the lumped-parameter components selected are tabulated in table 6-2.

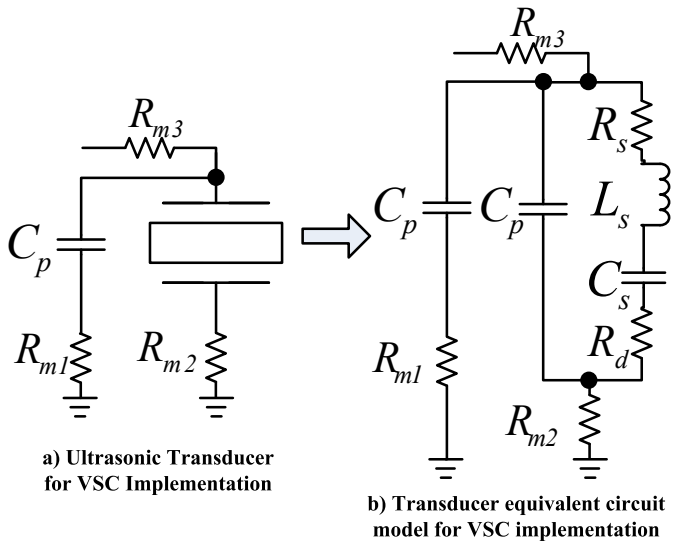

Figure 6-2: a) VSC transducer circuit model symbol b) circuit diagram for implementation

Symbol	Description	Values
C_p	Static Capacitance	2 nF
L_s	Dynamic Inductance (∝mass)	10 H
C_s	Dynamic Capacitance (∝1/stiffness)	1 nF
R_s	Dynamic Resistance	1 kΩ
R_d	Output Resistance	1 kΩ
R_{m1}	Measure Resistor 1	10 Ω
R_{m2}	Measure Resistor 2	10 Ω
R_{m3}	Serial Input Resistor	10 kΩ

Table 6-2: Parameter values of 1.75 kHz transducer circuit model

Note that the inductor analogue to mass, L_s, is impractically large and the Quality factor (Q) of the inductor is greatly reduced at low frequencies [103]. A possible alternative, known as a *Gyrator* [104], uses inductor-less devices to produce the required inductive properties. The following section will provide details of the selected *Gyrator* circuit configuration.

Gyrator-based Inductor

The gyrator-based inductor can be classified into single-ended and floating types. Single-ended means that one port of the gyrator-inductor needs to be grounded. A floating gyrator does not have this constraint. Since the inductor in the lumped-parameter circuit model of figure 6-2 has no earth for single-ended configuration, a floating inductor is required to mimic the behaviour of a physical inductor.

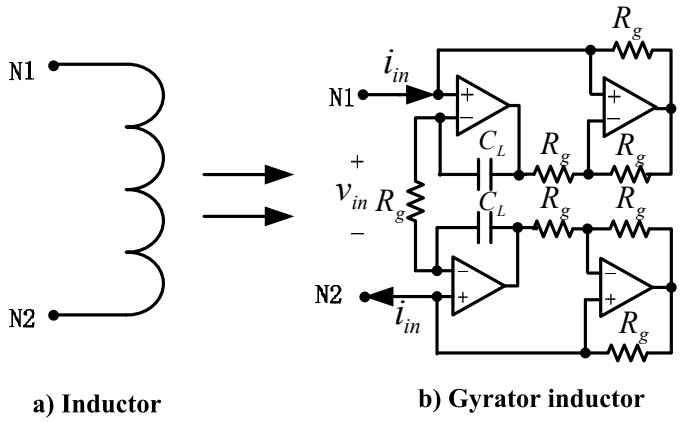

Figure 6-3: a) Floating inductor b) *Riordan* floating gyrator in back-to-back configuration

Figure 6-3 b) presents the selected active RC network configuration based on a *Riordan gyrator* in back-to-back configuration [105]. This network functions as an impedance converter. It "gyrates" the load capacitance, C_L, into an equivalent inductance appearing at the input ports N1-N2.

The input impedance of the gyrator, as illustrated in (6.3), is defined to be the ratio between the input voltage, v_{in}, over the input current, i_{in}, after Laplace Transformation. The gyration-inductance, as shown in (6.4), can be determined by choosing C_L and R_g.

$$V_{in}(s) = sC_L{R_g}^2 I_{in}(s), \quad if\ R_{g1} = R_{g2} = R_{g3} = R_{g4} = R_g \tag{6.2}$$

$$Z_{in}(s) = \frac{V_{in}(s)}{I_{in}(s)} = sC_L{R_g}^2, \qquad L_g = C_L{R_g}^2. \tag{6.3,6.4}$$

Due to the square term of the resistor R_g, it is not necessary to use a large capacitor, C_L, to generate the required inductance. Theoretically the active network of figure 6-3 b) will behave

approximately as an inductor when Operational Amplifiers (Op-Amp) have adequate gain [106]. Table 6-3 lists the parameters selected for the floating gyrator. The gyration-inductance is about 10 Henries.

Symbol	Description	Values
C_L	Load Capacitance	0.1 μF
R_g	Gyration-Resistance	10 kΩ

Table 6-3: Selected values of floating gyrator

6.2.2. Switcher and Driver

As can be seen from figure 6-1, the transducer VSC compensator has two feedback control system structures; one provides positive feedback and the other negative feedback. These two system structures share most of the parts in the control system except their driver circuits. This suggests the change from one system structure to the other can be regarded as the selection between two signal paths, each with its own gain factor. Figure 6-4 illustrates a feasible connection between switcher and driver in a simplified block diagram. The error signal is passed through either signal path 1 or signal path 2 depending on the criteria of the *channel selection* signal given in table 6-4.

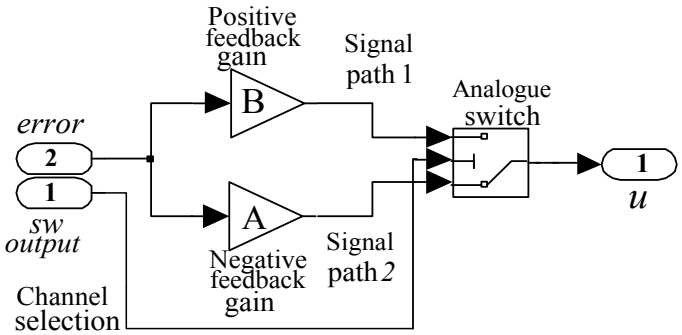

Figure 6-4: Switcher-based driver

Channel selection	Switcher output
1	Signal path 1
0	Signal path 2

Table 6-4: Channel selection criteria of switcher-driver subsystem

The practical design utilised a different form of switcher-driver connection, as shown in figure

6-5 a). This configuration implements the blocks A and B as programmable gain amplifiers which can be disabled through the switcher. The selected signal path is bypassed to ground and the other path is conducted.

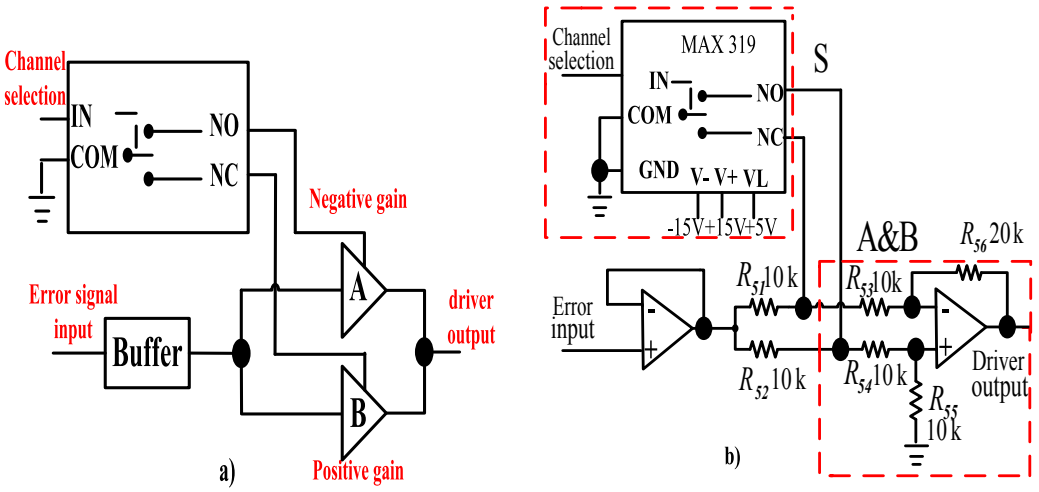

Figure 6-5: a) Illustrative diagram of switch-driver b) Schematic diagram of designed switch-driver

A schematic of the physically implemented switcher-driver subsystem is given in figure 6-5 b). The following sections will analyse how the driver and switcher are realised separately.

Driver Circuit

The negative feedback gain, A, in the control system is functionally represented by an *inverting amplifier*. Symmetrically, the physical realisation of positive feedback gain, B, could be a *non-inverting amplifier*. In this design, the two driver structures are integrated together using a single Op-Amp to reduce design complexity. The combined driver structure can be separately analysed, as demonstrated in figure 6-6 a) and 6-6 b) according to the conditions in table 6-4 and the relationship between input and output signals is expressed in (6.5).

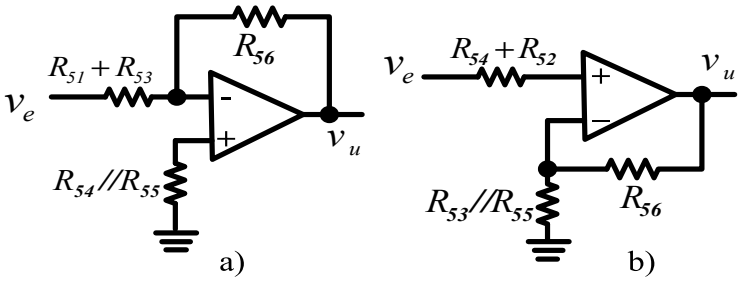

Figure 6-6: a) Equivalent circuit for negative feedback driver A b) Equivalent circuit for positive feedback driver B

$$v_u = \begin{cases} -\frac{R_{56}}{R_{51}+R_{53}} v_e, & channel\ selection = 1 \\ 1 + \frac{R_{56}(R_{53}+R_{55})}{R_{53}R_{55}} v_e, & channel\ selection = 0 \end{cases} \quad (6.5)$$

Switcher Subsystem

The switching between these two designated feedback system structures relies on an electronically controlled switching device. The physical switcher chosen in this design is an *analogue switch*, MAX319 [107]. It contains a *control input*, (IN), and two switch terminals *Normal Open* (NO) and *Normal Close* (NC) which are connected with the inputs of the two signal paths of the driver as shown in figure 6-5 b). The *common* (COM) port of the switch is grounded. The switch channels one feedback signal to ground and the other to the transducer.

6.2.3. Transducer Output Measurement M

This section deals with the transducer output measurement circuit used in the VSC compensator. There are two methods to obtain the transducer output signal. One is to measure the acoustic signal emitted from the transducer, the other is to measure an analogue to the current in the transducer acoustic branch formed by a differencing circuit. The former is unavailable due to the difficulties intrinsic in acoustic measurement. The concept of adopting a differencing circuit, as shown in figure 6-7 a), was first proposed in Chapter 4 as a realisable solution to detect an equivalent transducer output signal. This approximation signal can be acquired using a differential amplifier circuit as illustrated in figure 6-7 b). The inputs of the differential amplifier are the measured voltage across R_{m2} in the transducer branch and the voltage on R_{m1} in a capacitive arm that is similar to the transducer static branch. This circuit outputs a difference signal between the two input voltages v_{Rm2} and v_{Rm1}. Equation (6.6) specifies the input-output relationship of this differential amplifier circuit. The differenced outcome, v_{y^*}, is expected to be close to the current in acoustic branch in both magnitude and phase.

$$v_{y^*} = -\frac{R_{76}}{R_{73}} v_{Rm1} + \left(\frac{R_{75}}{R_{74}+R_{75}}\right)\left(1 + \frac{R_{76}}{R_{73}}\right) v_{Rm2}. \quad (6.6)$$

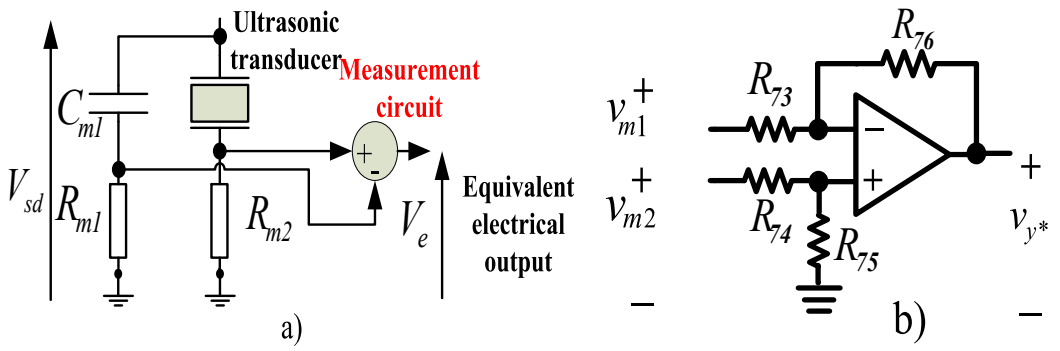

Figure 6-7: a) Circuit diagram for electrical equivalent sensor output b) differential circuit used as error detector

6.2.4. Sensor Gain Amplifier H

In figure 6-7 b), a DC-blocking capacitor is placed in series with the inverting input of the differential amplifier to reject the likely DC offset produced by the analogue transducer model. Nevertheless, this capacitor forms a high pass filter (HPF) configuration that generates a 90 degrees phase lead. This phase change must be removed, for the variable structure system to reach the correct switching condition decisions. Therefore, a low pass filter (LPF), as seen in the same figure, is used to compensate for the phase lead.

Z_{81}	Z_{83}	R_{81}	C_{81}	R_{83}	C_{83}
$R_{81}+\frac{1}{C_{81}s}$	$R_{83}//\frac{1}{C_{83}s}$	500 Ω	10 µF	50 kΩ	0.1 nF

Table 6-5: Parameter values of senor gain amplifier configured as BPF

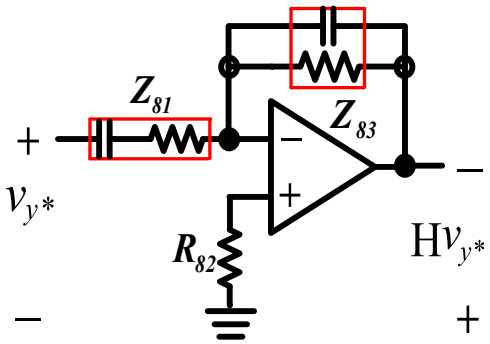

Figure 6-8: Sensor gain amplifier configured as BPF

$$G_{HPF} = -\frac{R_{83}}{\frac{1}{C_{81}s}+R_{81}} = -\frac{R_{83}C_{81}s}{1+R_{81}C_{81}s}, G_{LPF} = -\frac{R_{83}V_{i1}}{(C_{83}s)(\frac{1}{C_{83}s}+R_{83})} = -\frac{R_{83}sV_{i1}}{(1+R_{83}C_{83}s)R_{81}}. \quad (6.7,6.8)$$

$$G_{BPF} = -\frac{Z_{83}}{Z_{81}} = -\frac{R_{83}}{C_{83}(\frac{1}{C_{83}s}+R_{83})(\frac{1}{C_{81}s}+R_{81})}. \quad (6.9)$$

To examine the frequency and phase response of these filters, the total transfer function of the LPF, HPF and band pass filter (BPF) are deduced and a *Bode* Diagram is plotted using the parameters in table 6-5. The composite plot in figure 6-9 provides the magnitude and phase variation from 10^{-1} to 10^{7} Hz. It can be observed that G_{HPF} and G_{LPF} yield high pass and low pass frequency responses respectively. The magnitude response of the BPF transfer function, G_{BPF}, indicates that The phase response of the filter remains at 180 degrees at the working frequency of the transducer system, around 1.75 kHz, due to the *inverting amplifier* configuration.

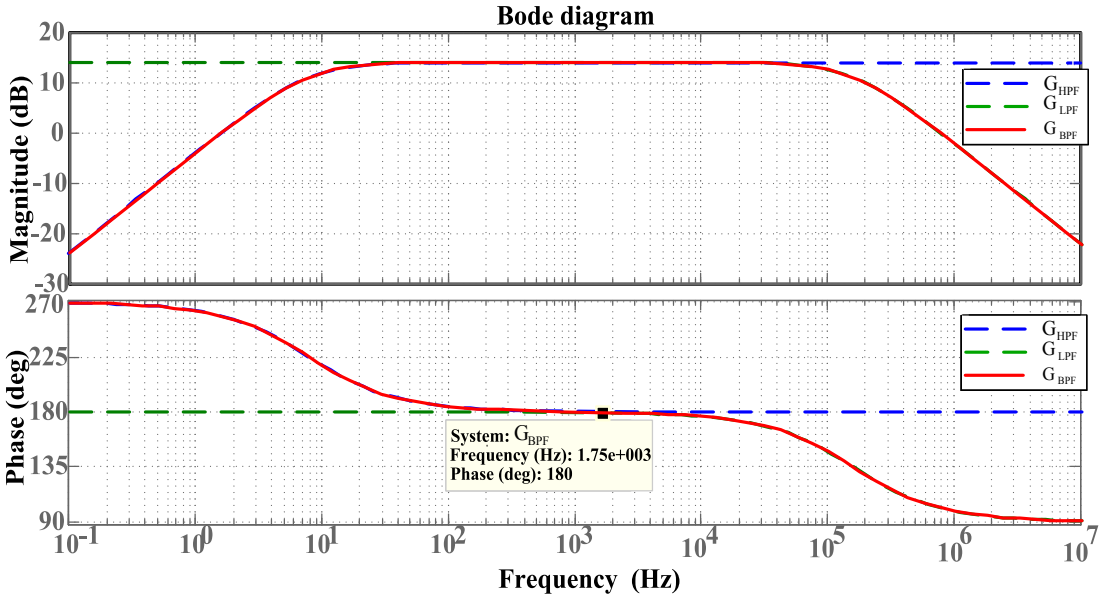

Figure 6-9: BPF magnitude and phase responses

6.2.5. Error Detector E

The transducer circuit model, switcher-based driver and transducer output measurement circuit presented in the last three subsections form an open-loop transducer drive and measurement system. The measured transducer output, through detector M, is fed back to be compared with

the demand signal. The error detector is required to close the control loop. It is used to measure the deviation of transducer feedback signal, Hy* from the reference input Fr. This error is defined to be:

$$v_e \equiv v_{\mathrm{F}r} - v_{\mathrm{H}y^*}. \tag{6.10}$$

Any change of sign in the analogue paths of the control system could possibly reverse the phase of system error signal. Figure 6-1 is simplified to illustrate how the analogue circuit is configured to achieve the defined error signal. In figure 6-10 a), the transducer system is configured in negative feedback mode to determine the sign of each block, for positive feedback is only needed when the system phase trajectory crosses the *switching line*. To begin the analysis, the feedback path is initially disconnected. The reference input signal Fr is directly passed to the driver and is reversed by the *inverting amplifier*. When the transducer is driven by a signal resonating at its central frequency, the transducer impedance becomes resistive. Therefore, both signals measured at detector M and the transducer model output should maintain the same sign as that of drive signal.

To compare the reference input and transducer output feedback in the form defined in (6.10), gain blocks F, H and error detector E are arranged consistently using *inverting amplifiers*. F and H yield -Fr and Hy*. The error detector E uses an adder circuit as shown in figure 6-11. The combined inputs (-Fr + Hy*) will be inverted by E to produce (Fr-Hy*). The output signal can be computed using expression (6.11).

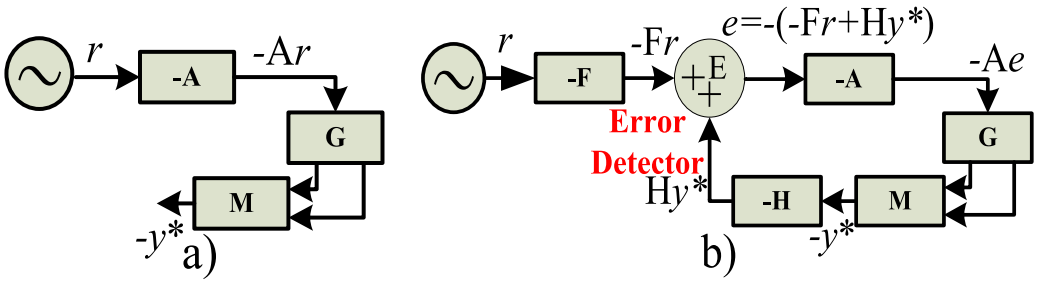

Figure 6-10: a) Block diagram of open-loop configuration b) Sign arrangement of closed-loop system

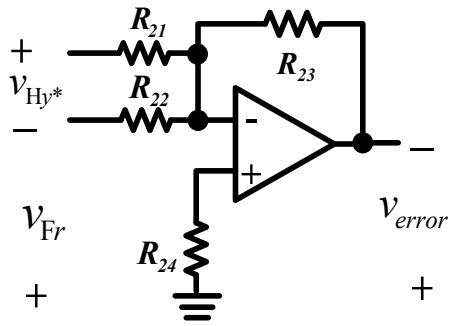

Figure 6-11: Adder circuit used as error detector

$$v_{error} = -\frac{R_{23}}{R_{22}}\left(v_{\mathrm{H}y^*} - v_{\mathrm{F}r}\right), \quad \text{if} \quad R_{21} = R_{22}, \;\; R_{23} = R_{24}. \tag{6.11}$$

6.2.6. Voltage Level Shifter L

A level shifter using the configuration shown in figure 6-12 will lift the average voltage of the error signal to the middle of the ADC input range (in this design it is between 0 V and 3.3 V) by superimposing 1.6 V on the error signal. The non-*inverting amplifier*-based level shifter has a prescribed gain to ensure that the magnitude of error signal does not overflow the ADC conversion range.

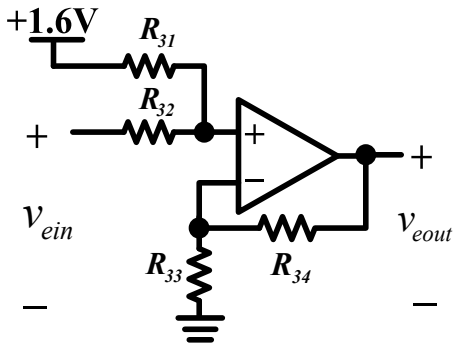

Figure 6-12: Voltage level shift circuit configuration

$$v_{eout} = \left(1 + \frac{R_{34}}{R_{33}}\right)(v_{ein} + 1.6\mathrm{V}). \tag{6.12}$$

In conclusion, Section 6.2 has demonstrated the physical representation of each functional module in the analogue path of the transducer VSC compensator. A switchable feedback control system can be formed by fitting these modules into the block diagram of figure 6-1. Problems such as determination of transducer resonant frequency, the DC offset of the Op-Amp and phase

shifts caused by active components are encountered when practical implementation is considered. The circuit designs introduced in each subsection, have addressed these problems. The following section will investigate the design and analysis of the digital part of the transducer VSC system.

6.3. Digital Subsystem

Section 6.2 investigated the architecture of the analogue circuits in the VSC transducer system and how they are constructed. It ends with the introduction to the comparator circuit that produces system error. This error will be imported into a digital microprocessor through an internal ADC to implement the control algorithm. This section will describe how the control algorithm is developed within the ARM microprocessor.

6.3.1. ARM Processor LPC2368

A prototype board LPC2368 containing an ARM7 chipset was selected to realise the discrete *switching line* algorithm of the control system. This board was chosen due to the ease of connection and programming. The 32-bit processor can input and output digital signals and includes a 10-bit Successive Approximation Routine (SAR) type ADC with a maximum sampling rate of 400 kilo samples per second (ksps) [108] for the input of analogue signals. The ADC is internally linked to an ARM core, which transfers the digitised signal to the processor through a data register. The power supply range for both the ARM core and the internal ADC is between 0 and 3.3V, which restricts the range of measure for the ADC to the same range. The ADC and General Purpose Input Output (GPIO) peripheral clock frequencies are supplied by an on-chip real-time clock (RTC) module which will be introduced in Subsection 6.3.3.

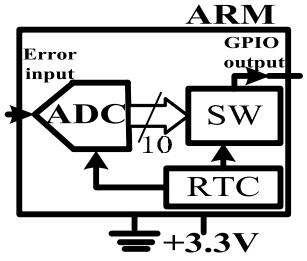

Figure 6-13: Reduced block diagram of ARM processor for VSC compensator

6.3.2. Signal Quantisation due to ADC

The measured deviation between the reference input and system feedback is sampled and quantised before transfer to the processor core. The 10 bit ADC resolution, given a 3.3V power supply, yields a least significant bit of:

$$1\text{LSB} = \frac{3.3\text{ V} - 0\text{ V}}{2^{10}}. \tag{6.13}$$

which yields in a theoretical resolution of 3.222mV.

6.3.3. System Clock Frequency

LPC2368 uses a low frequency external crystal oscillator at 12MHz. This external clock signal is up-converted to a higher frequency by an on-chip Phase-Locked Loop (PLL)[108]. The output of the PLL passes through frequency dividers controlled by the respective control registers to provide the customised working frequency for the processor core and other interfaces [108]. The procedures to the PLL configuration to produce the required ADC and GPIO frequencies are illustrated using a simplified block diagram in figure 6-14 and explained in the following subsection. The actual coefficient initialisations in the computer programme are given in Section 9.3.

In this design, the CPU clock frequency ($\mathrm{F_{cclk}}$) and the frequency of the PLL output signal ($\mathrm{F_{cco}}$) are chosen to be 48 MHz and 288 MHz respectively. Therefore, the coefficient for the CPU clock divider, CCLKSEL, is set to be 6. The PLL output frequency ($\mathrm{F_{cco}}$) needs to be configured by choosing the PLL divider factors (*M* and *N*). It is suggested in the user manual that not all potential combinations of *M* and *N* are capable of generating the desired clock frequency [108]. The relationship between PLL input and output signal frequencies is shown in (6.14)

$$\mathrm{F_{cco}} = \frac{\mathrm{F_{osc\_in}} \times M \times 2}{N}. \tag{6.14}$$

(6.14) can be altered into the forms of (6.15) and (6.16) with *M* and *N* as unknown values.

$$N = \frac{\mathrm{F_{osc\_in}} \times M \times 2}{\mathrm{F_{cco}}}, \qquad M = \frac{\mathrm{F_{cco}} \times 2}{\mathrm{F_{osc\_in}} \times N}. \tag{6.15,6.16}$$

The choices of *M* and *N* for this illustration are 12 and 1. The value of the peripheral clock divider for the ADC is chosen to be 28 to generate a sampling frequency of 1.7 MHz. Because the SAR ADC takes 11 cycles to complete one conversion, the actual sampling rate is 155 ksps. Figure 6-15 depicts the conversion results of 1 kHz sinusoid test signal recorded using digital oscilloscope and plotted in Matlab.

Parameters	Descriptions	Values
F_{osc_in}	External Clock Signal Frequency	12 MHz
F_{cco}	PLL Output Clock Signal Frequency	288 MHz
F_{cclk}	CPU Clock Signal Frequency	48 MHz
F_{pclk}	Individual Peripheral Clock Signal Frequency	1.7 MHz
N	PLL Pre-Divider Value from The NSEL Bits in the PLLCFG Register	1
M	PLL Multiplier Value from The MSEL Bits in the PLLCFG Register	12
CCLKSEL	CPU Clock Frequency Division Value	6
PCLKSEL	Peripheral Clock Frequency Division Value	28

Table 6-6: Parameters for CPU and peripheral clock frequency setting

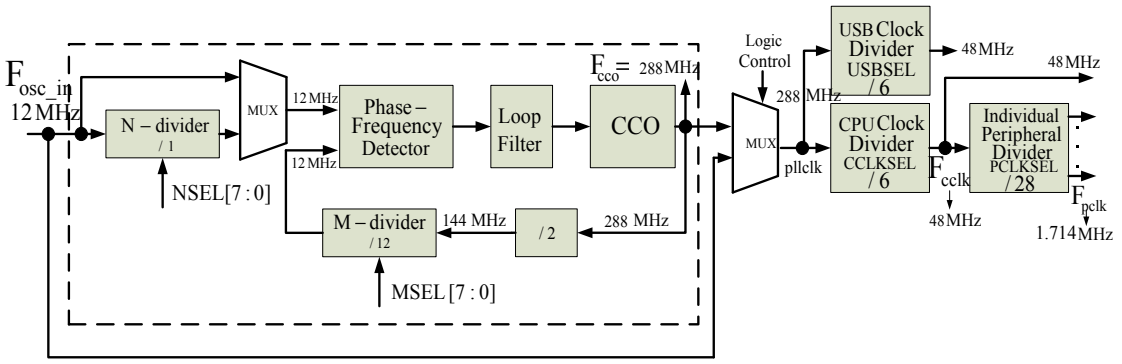

Figure 6-14: PLL-based system clock management [108]

The section above describes the ARM board configuration process necessary to achieve the desired ADC sample period and to drive the other peripherals.

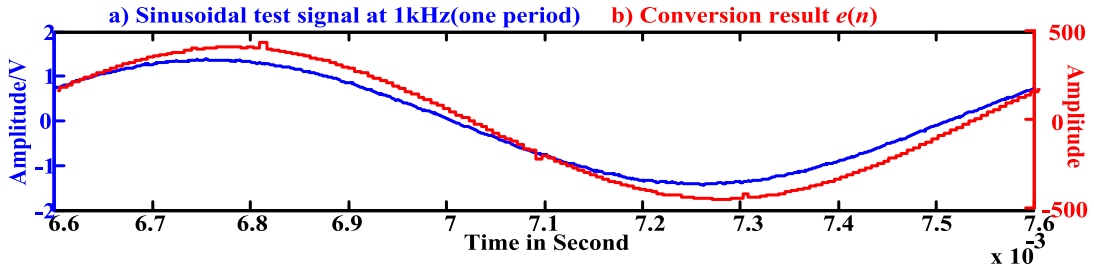

Figure 6-15: Illustaration of Sampled signal a) 1 kHz sine wave signal (blue) b) conversion results (red)

6.3.4. Microprocessor Implementation of the *Switching Line* Algorithm

This section describes the *switching line*, *sw*, algorithm implementation using the selected ARM microprocessor. As introduced in Chapter 4, the switching conditions for Variable Structure Control (VSC) are summarised in (6.17) with the *switching line* equation for *sw* given (6.18). Figure 4-4 j) is repeated here for convenience.

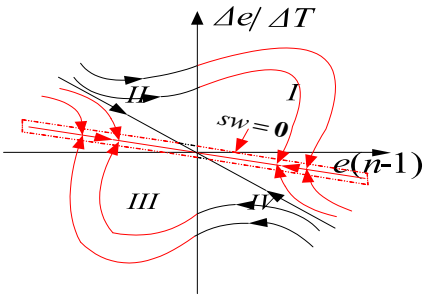

Figure 4-4: j) Expected switching phase trajectory

$$u = \begin{cases} \mathrm{A} * e, e(n) \in I \cup III, \\ \mathrm{B} * e, e(n) \in II \cup IV. \end{cases} \tag{6.17}$$

The selection of the different control gains stated in (6.17) depends upon the gradient of the *switching line*, c_{tran}. This is the reciprocal of the desired transient time constant of the constrained system dynamics. To compute *sw*, defined in (6.18), the temporal gradient of the error is required.

$$sw \equiv \frac{e(n)-e(n-1)}{\Delta T} + c_{tran} * e(n-1). \tag{6.18}$$

In (6.18), the estimation of the error gradient signal is based on a difference operation between two consecutive samples. Given the desired value for c_{tran}, the sampling period ΔT is chosen to best represent the transient of the input signal and its choice can be treated as a scaling factor.

Figure 6-16 is used to investigate the choice of sampling period ΔT. The red curve in figure 6-16 is the gradient signal of a 1 kHz sinusoidal test signal estimated using (6.19) before it is mathematically scaled by $1/\Delta T$.

$$e_d = e(n) - e(n-1). \tag{6.19}$$

It can be observed that the calculated error gradient is a noisy estimate with a 90 degrees phase

lead compared with discretised sinusoidal test signal $e(n)$ in blue in figure 6-16. It can also be seen that the analogue-to-digital conversion errors in $e(n)$ lead to large artefacts in the gradient. Figure 6-17 is the phase trajectory plotted using the sampled sine wave and its gradient. The conversion errors and associated gradient artefacts cause spikes in the phase portrait. This experiment illustrates that the gradient estimate using the difference of sampled data is sensitive to high frequency noise in the error signal. The conversion errors cause significant distortion of the phase trajectory.

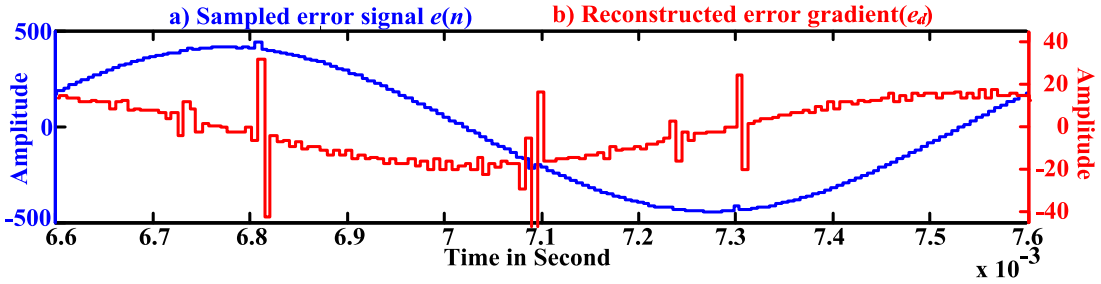

Figure 6-16: a) Sampled system error signal (blue) b) Computed error velocity (red)

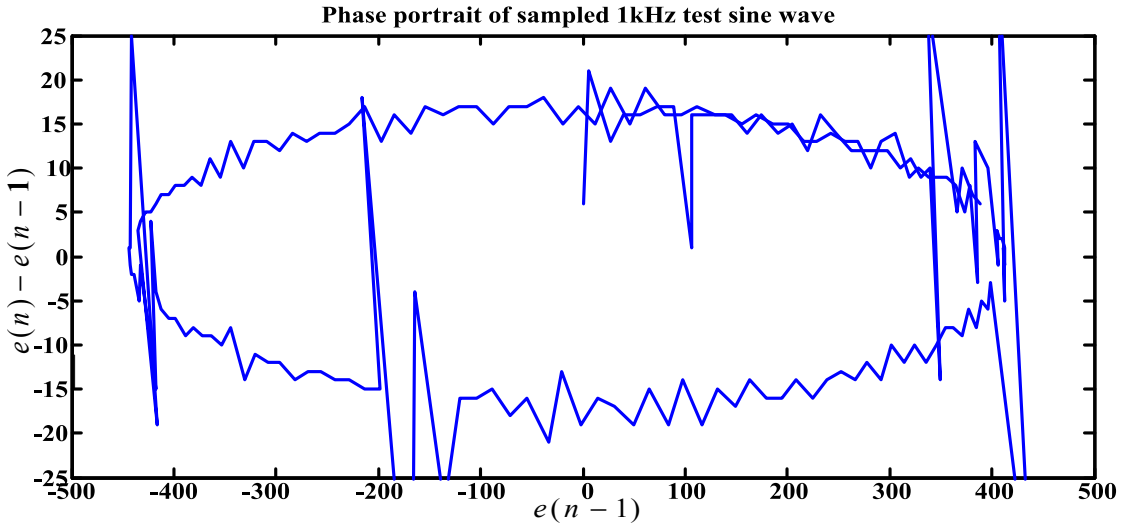

Figure 6-17: Discrete phase portrait plotted using sampled error and velocity signals

One purpose of the sampling period ΔT is to balance the contributions of the error signal and its gradient to yield a phase portrait that is approximately circular. For a sinusoidal error signal:

$$e(t) = Acos(\omega_o t). \tag{6.20}$$

the gradient is also sinusoidal, with a 90° phase shift:

$$\frac{de}{dt} = A\omega_o sin(\omega_0 t). \tag{6.21}$$

Using Taylor's series, truncated after the linear term, the gradient estimate may be written:

$$e(n) - e(n-1) \cong \Delta T \frac{de}{dt}\Big|_{t=n\Delta T} \tag{6.22}$$

which is sinusoidal with amplitude:

$$\Delta e_{max} = \Delta T A \omega_o \tag{6.23}$$

Given a sampling frequency $1/\Delta T = 155$ kHz, $\omega_o = (2 \times \pi \times 1000\ \text{Hz})\ rad/sec$ and $A = 420$, this predicts that Δe_{max} =17. These values are all consistent with figure 6-16.

For control to be feasible, the sampling frequency must be much greater than the drive frequency i.e. $\Delta T \ll 2\pi/\omega_o$. Therefore, the amplitude of the gradient estimate will typically be much smaller than the error term.

The ADC data register produces 10-bit resolution conversion results with fixed-absolute error. The calculation of e_d is achieved by the subtraction of the previous measured value from the current one. If there is little difference between them, this result will be a very small number. The illustration of the bit distribution is shown in figure 6-18 where the difference between error values is very small. Multiplication of e_d by the constant $1/\Delta T$, can often be accomplished in the microprocessor by a bit shift but this does not increase the number of significant figures.

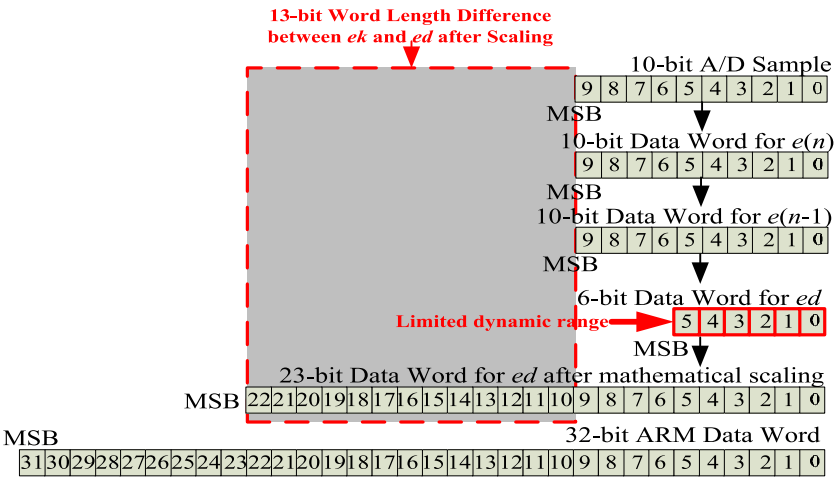

Figure 6-18: Illustrative diagram to explain numerical inconvenience caused by ADC word length

The critical factor causing the small dynamic range of the velocity signal is that as the sampling period is relatively short, consecutive error samples have similar values, which results in an error velocity with a low number of significant figures. If the sampling frequency is too slow the feedback control will lose performance. As the sampling period increases to a quarter of a drive signal period, the gradient estimate increases yielding a larger number of significant bits, but the finite different approximation to the gradient becomes less accurate.

In this illustration, the use of the sampling period as a scaling factor in combination with the *switching line* gradient, ΔT and c_{tran}, achieve an acceptable signal range for both the position and velocity of the error measure. As the switching condition is based on the sign of *sw*, it may be scaled arbitrarily. By dividing through by the constant, c_{tran}, the switching line condition may be redefined:

$$sw = \frac{e_d}{c_{tran}*\Delta T} + e(n-1). \tag{6.24}$$

where the sampling period, ΔT, is determined in the Subsection 6.4.3 to be 0.000006451 seconds. The *switching line* constant represents the length of time that the error signal takes to return back to nearly zero when a phase change occurs. The transient time period of the error, T_{tran}, in the transducer system reflects the phase difference between the demand signal and transducer output. This phase error is expected to be minimised within a given fraction of a carrier signal period. In this design, this time constant is chosen to be half of the carrier signal period. Therefore the resulting value for c_{tran} can be calculated by substituting the centre frequency of transducer circuit model $f_{\mathrm{r}} = 1.75$ kHz into (6.25):

$$c_{tran} = \frac{1}{2*T_{tran}} = 2 * f_{\mathrm{r}} \approx 3500 \text{ Hz}. \tag{6.25}$$

This yields a coefficient of approximately 44.28 for (6.24). In this design, it is approximated to be 45 since the fixed-point microprocessor it must have an integer value. Therefore, the final *switching line* equation becomes:

$$sw = 45 * e_d + e(n-1). \tag{6.26}$$

The sections above have described the digital features of the ARM microcontroller with a focus on the effects of finite precision as well as the system sampling frequency.

6.3.5. Implementation of VSC Algorithm in the C Language

The VSC algorithm coded in Matlab may be easily translated into the C programming language. The structure of the program code written in C can be partitioned into system configuration and algorithm implementation.

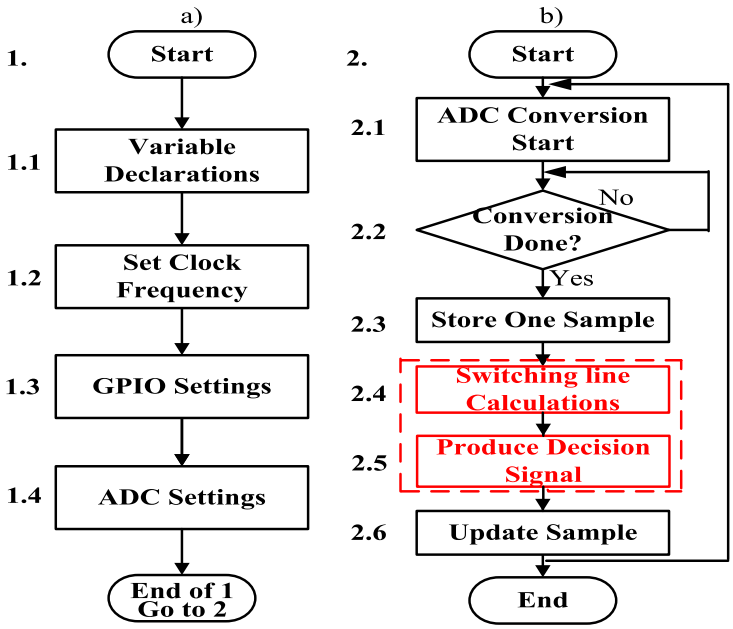

Figure 6-19: a) System configuration b) Algorithm implementation

Two conceptual flowcharts for the program structure are depicted in figure 6-19. The system configuration illustrated in figure 6-19 a) aims to initialise the ARM processor before executing the control algorithm. It includes global variable declarations and initialises the required peripherals i.e. system clocks, ADC and GPIO.

After configuring the necessary peripherals, the ADC will start conversion. The processor waits for the completion of the analogue-to-digital conversion, flagged by the setting of the Most Significant Bit (MSB) of ADC data register. Logical “one” of this bit indicates a conversion is complete. The converted value, stored in the ADC data register, needs to be loaded into a predefined variable for the current sample, ek0, before it is automatically refreshed by the

following conversion result. Next, the ARM processor core calculates the *switching line* value described in (6.18) using the stored samples, $e(n)$ and $e(n\text{-}1)$. Application of the control law yields a pulsed decision signal to instruct the analogue switcher to vary the system structure. The realisation of the *switching line* algorithm will be examined in detail in the following subsection. Before one iteration calculation terminates, the value in current sample variable ek0 will be shifted into the variable ek1 to update the previous sample $e(n-1)$. This part of program loops indefinitely.

6.3.6. *Switching Line* Algorithm Implementation

The focus of this subsection is to describe the *switching line*-based control algorithm implementation illustrated in the fourth and fifth steps of figure 6-19 b). The on-chip ADC subjected to the power supply range (0-3.3V) can only process positive signals. Therefore, the DC bias in $e(n)$ produced by the voltage level shifter must be removed after the ADC output is loaded into the variable, ek0, for the current sample. The *sw* and error gradient, see (6.18) and (6.19), are determined in the steps 2.4.2 and 2.4.3. These two equations each yield integer results. However, only the sign of the results are used to determine in which quadrant of the phase plane the state vector resides.

The phase plane is partitioned by the boundary conditions $e(n-1)$ and *sw* and has four regions. Negative feedback is applied in the first and third quadrants. If the trajectory is detected in the second and forth quadrants positive feedback will be activated. However, the output from ARM processor only has two states, logic "1" and "0", as the indications to switch system structures. As a result, the regions represented by the indication signal must be inspected before applying positive feedback. To uniquely identify each region on the phase plane, four pulse signals carrying diagnostic information are generated, based on the switching conditions as illustrated in step 2.5 of figure 6-19 b). The pulse width of the diagnosis signal suggests the time interval in which the phase trajectory passes through each region.

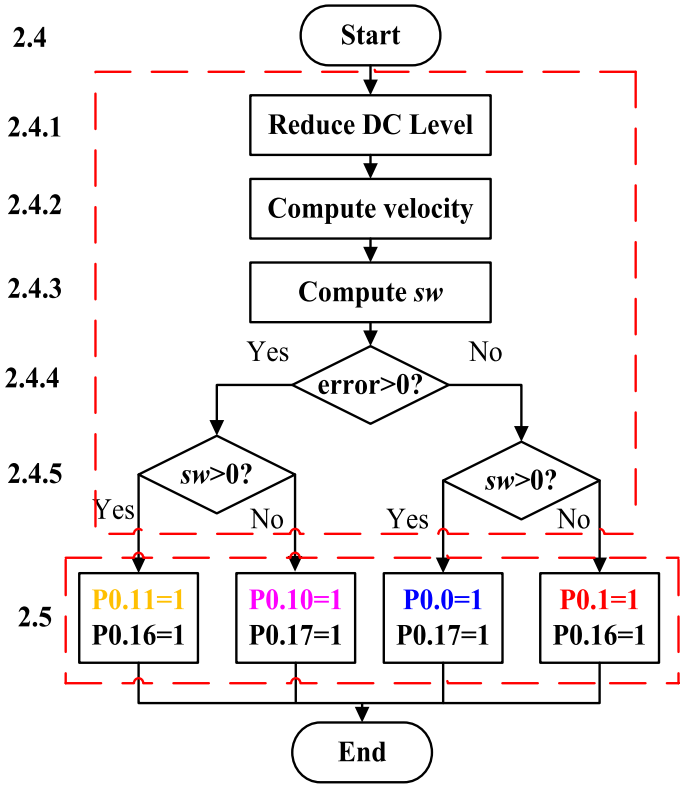

Figure 6-20: Flowchart of *sw* algorithm implementation

region1:	$e(n\text{-}1)>0$,	$sw>0$	P0.3-L15	P0.16	Negative Feedback
region2:	$e(n\text{-}1)<0$,	$sw>0$	p2.10-L12	P0.17	Positive Feedback
region3:	$e(n\text{-}1)<0$,	$sw<0$	P0.0-L13	P0.16	Negative Feedback
region4:	$e(n\text{-}1)>0$,	$sw<0$	P0.1-L14	P0.17	Positive Feedback

Table 6-7: Conditions for quadrant detection and pin assignments

Figure 6-21 demonstrates the diagnosed phase portrait and a shallow *switching line*, sw, resulting from (6.26). The output pulse signals, according to the switching conditions tabulated in table 6-7, are used to distinguish the phase trajectory into four regions by different colours. The plotted *switching line* (green dash line) is matched with the effective boundary of vertically adjacent regions. The sharp distortions of the phase trajectory crossing the *switching line* bring about considerable impact on the decision-making algorithm to identify the defined quadrants. Notably, the distortions emerge at which the discretised error signal, $e(n)$, encountered discontinuities due to real ADC conversion as seen in the blue curve of figure 6-16. Also, the error velocity signal, *ed*, is merely represented by a small number of significant bits.

The experimental result in figure 6-21 verifies that the defined regions are identifiable on the

sample phase trajectory using the quadrant detection algorithm and switching conditions. To obtain a switching input signal for the *analogue switch* used in this design, it is feasible to produce an output during the time period that both regions 1 and 3 are detected. The selection of a switching signal is dependent on the logic of the *analogue switch* defined in table 6-4.

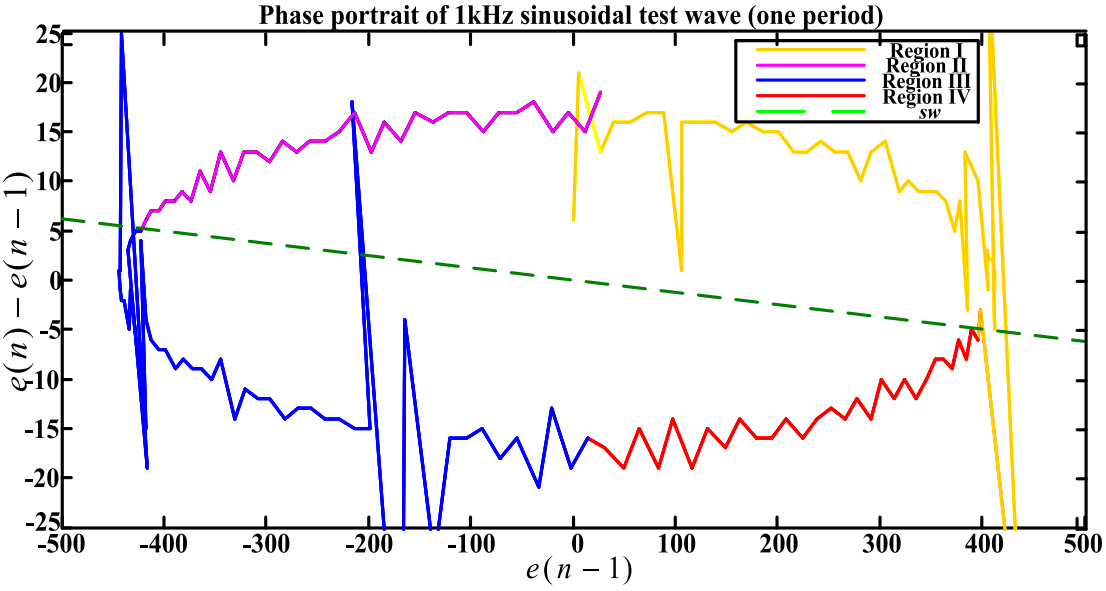

Figure 6-21: Diagnosed phase portrait with colourfully identified regions

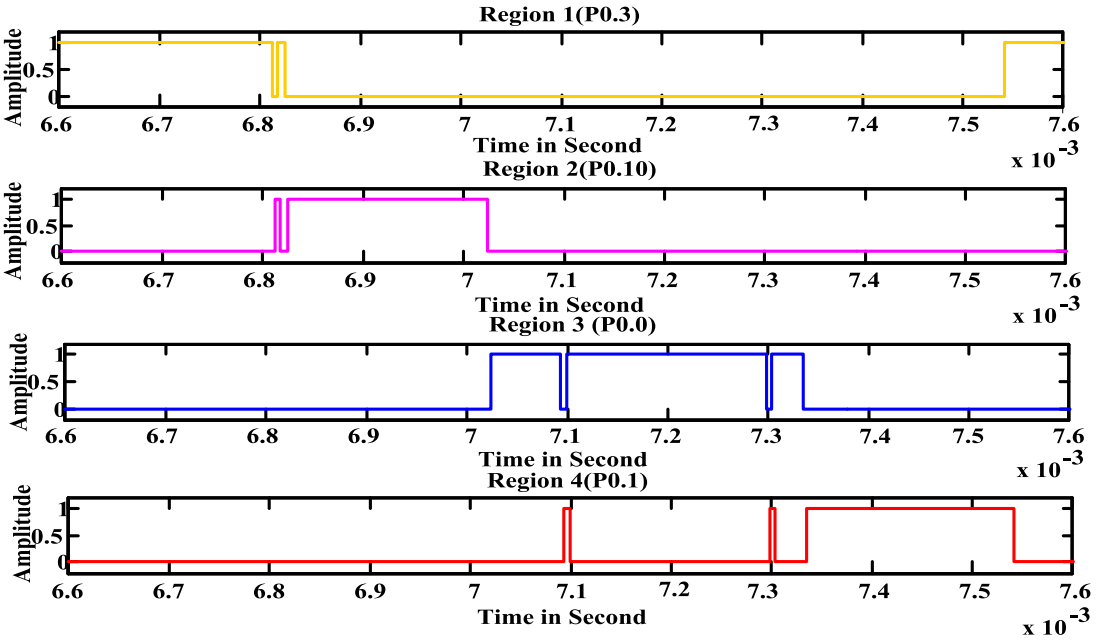

Figure 6-22: Time responses to the detected regions

6.3.7. Performance Evaluation

The performance of the hardware implemented transducer VSC compensation system will be evaluated in this section. Before presenting the measured responses, the general testing conditions and parameters used in this experiment are summarised in table 6-8.

Carrier frequency	Modulation signal frequency
1.75 kHz	100 Hz
System power supply range	BPSK Amplitude
± 15 V	± 0.5 V
Gain block A	Gain block B
10	40
Gain block F	Gain block H
2	135
T_{tran}	$1/(c_{tran}\Delta T)$
0.225 ms	45

Table 6-8: Constructed test bench system parameter values

The following part of this subsection will present and analyse a set of real measurements from the closed-loop system under evaluation. The first and third rows of figure 6-23 are the BPSK reference input *r* and resulting transducer output response *y* compensated by switching control. The middle frame of figure 6-23 is the system error transient *e* indicating the phase difference between *r* and *y*. The captured waveforms contain two phase reversals. Both require a duration of approximately $T_{tran} \approx 0.225$ ms for the error transient to become nearly stationary. The observed output signal waveform is inverted and compared to the reference input *r*. This inversion is due to the sign assignment explained in the Subsection 6.3.5. The measured output responses demonstrate that the error transient duration of the transducer system can be shortened around the anticipated transient time.

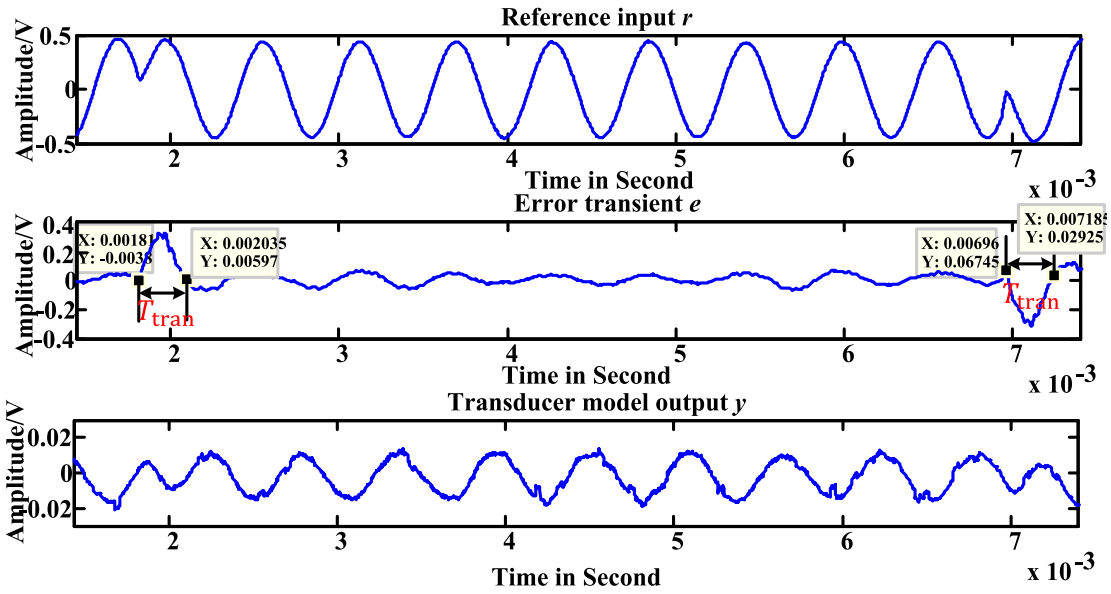

Figure 6-23: Illustrations of measured transducer VSC system responses

The system dynamical behaviours during the transitions of two carrier phase changes are depicted in figure 6-24. The square markers represent the sample points on the discrete phase plane. These samples are connected with straight lines as a representation of phase trajectory. Different colours are used to classify the samples in corresponding regions by the defined quadrant boundary conditions according to table 6-7.

It can be seen that the distorted phase trajectory is strongly affected by the quantisation effect. The small amount of change in error magnitude merely leads to limited number of significant bits (4 or 5 bits) causing irregular velocity estimates. In spite of constrained numerical resolution, the phase trajectory of the error still demonstrates switching activities (traces with red and purple markers) surrounding the *switching line*, *sw*, for both phase changes.

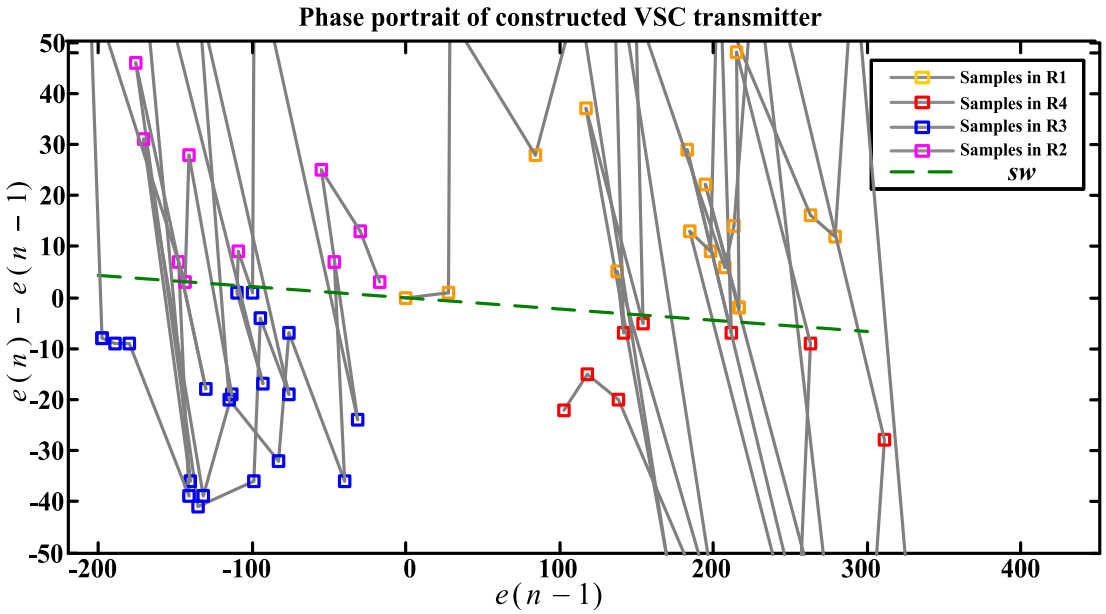

Figure 6-24: Phase portrait plots of the two phase transitions

In fact, reduced resolution in the phase domain brings about coarse granularity of the velocity estimation during the entire phase transitions. The VSC system is designed to calibrate whenever the phase error is unsatisfactory to the boundary conditions as can be seen in traces with blue and yellow square markers in figure 6-24.

The measured results above verify that the transducer model can manage to generate the output response with a more visible and faster transient due to VSC compensation. The system error dynamic response magnitude can be reduced to a tolerable level within approximately the expected transient time. Whereas the phase plane illustration indicates the VSC compensator is busy rectifying unacceptable transient responses, the resolution capacity on the velocity axis is severely limited by the number of significant bits representing quantised data.

To observe the consequences to the nature of the drive signal, due to the switching approach, two sets of time domain measures are demonstrated to yield comparisons between r and y in figures 6-25 a) and 6-25 b). The impact of velocity estimation with low resolution on the transducer output occurs not only during the phase transitions, but when the response is in steady-state. The glitches on the drive signal are tidying up the shape of the sine wave where the dynamic is not consistent with expectation. This result implicitly shows that the VSC compensator is monitoring the system dynamic and can be instantaneously activated to fix every

unacceptable bit in the curve.

Furthermore, the chattering behaviour observed in the drive signal takes a finite time to switch. The switching speed between the two feedback structures is determined by the *Slew Rate* (S_R) of the driver amplifier. Essentially, when a sample that crosses *sw* is identified, a pulse signal is produced to switch the feedback system structures.

The variations of system structures can possibly lead the driver amplifier to saturation distortions. Consequently, the instantaneous response of the driver may not be capable of following the changes in the input signal.

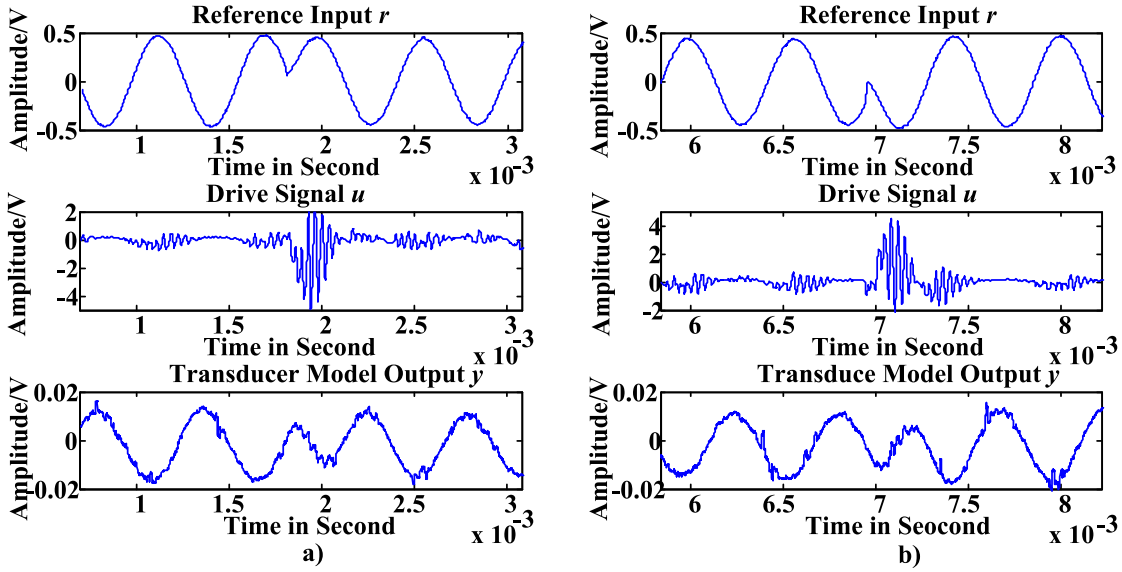

Figure 6-25: Temporal waveforms of the driver outputs compared with *r* and *y*

6.4. Summary

A hardware 1.75 kHz phase-modulated (PM) transmission system with Variable Structure Control (VSC) transient compensation was studied in this chapter. The measured performance of the real system indicates the phase error transient between the system reference input and measured response can be minimised to half of a carrier wavelength. Constraints using an analogue computer to emulate the analogue paths and digital processor to realise *switching line* (*sw*) algorithm are investigated through practical experiments under non-idealised test conditions. This investigation can be separated into two sections. The first part analysed the composition of analogue circuits in the control loops. The realisation of the transducer output

sensory unit proposed in Chapter 4 is of interest. The DC offset and phase shifts in output measure unit must be eliminated. The second part covers the consequences of quantisation to the error signal and *sw* algorithm. The number of significant bits provided by the ADC is considered as a critical parameter determining the resolution of error velocity estimation. Also, imperfectly quantised signals can possibly produce considerable numerical error in the reconstruction of the error gradient. However, a satisfactory transient response that is affected less dependently on the above constraints is still obtainable unless the noise and non-linearity reach intolerable levels.

Chapter 7.

Conclusions and Further Work

This chapter is devoted to summarising all the investigations presented in this study and recommendations will be given to guide further research within and beyond the studied area.

7.1. Conclusions

In phase modulation (PM) based ultrasonic (US) communications in air, inertia in the transmitter and receiver transducers causes a delayed response to a phase change of the drive signal. It was found that, for a 40 kHz *piezoelectric* transducer, this delay (up to a dozen carrier cycles) is closely associated with the resonant properties of both transmitting and receiving transducers. The longer the delay, the slower symbols can be transmitted. Consequently, the system capacity is significantly reduced to a data rate of 1 or 2 kilo bits per second (kbps). Although the resonant dynamic of individual transducers can be compensated using control technologies, it is difficult to observe the compensated results since both transmitting and receiving transducers are resonators. Therefore the design of dynamic compensation needs to be separately considered for each transducer.

Chapter 3 thoroughly evaluates the transient responses of the US transducers by experimental determination of the transducer output to a pulsed excitation. A transducer data sheet describing the transducer lumped parametric models and the corresponding parameter data was found. Computer simulations using the selected transducer model were conducted to predict the output responses of individual transducers. Physical transducer output responses were measured with basic circuit configurations. The results presented demonstrate that the predicted responses of the chosen transducer lumped-parameter models, using parameters estimated from the data sheet, are consistent with those from the physical transducers. Therefore, one can be assured that the lumped parameter model representation is sufficient to simulate the behaviour of the real transducers.

Also, a communication channel was established to assess how the delayed response influences

the decoding process. It was found that the phase separation of each transmitted symbol is vague and difficult to detect due to the long transient period. Thus, the uncompensated transducer response requires long symbol periods to allow symbol decoding. The constructed platform attempted to demodulate the transmitted symbol with shifted phase switching, using a Phase-Locked Loop (PLL)-based demodulation system. However, the observations showed that incorrect codes frequently appeared in the de-modulated results. This result suggests that the adopted PLL system cannot help reduce the transient duration, which means the implemented open-loop system is still vulnerable to the phase detection errors in the phase change of the carrier wave.

The experimental results in Chapter 3 illustrated that there is the opportunity to increase the capacity of the acoustic communication system if the transient time of the transducers can be reduced. A control system can be applied to minimise the transient period. Intensive research has been presented in the vibration control of dynamic processes, but little work has been reported on methods of controlling the vibration of US air transducers. It has been attempted by other researchers [29] using the specified pulse-amplitude modulated drive signals to stimulate the transducer. However, the damping of the resonance depends entirely on the transducer dynamical properties and is susceptible to parametric variations, both between transducers and over time.

In this thesis, Variable Structure Control (VSC) is used to control the transient of US transducers. It has been demonstrated that standard US transducers under control of a VSC can reduce the transient of the transmitter and the receiver systems. The transient responses of transmitting and the receiving US transducers can be tailored to their functions. The length of the transient is determined by the *switching line* of the VSC. Chapter 4 explores the construction of VSC compensation for transmitting transducer. It was shown in the simulated results in Chapter 4 that VSC compensation can be applied to any transducer provided the required feedback configurations can be achieved i.e. a *stable-focus* phase portrait for one switching condition and a *saddle point* for the other. It was also found that a system structure consisting of one positive and one negative feedback path is not the only choice to realise the required two feedback

configurations. Two positive feedbacks with different amounts of gain can also exhibit similar transient reduction, but yielding an inverted output waveform.

The application of the VSC transient compensation in US receiver design was first proposed in Chapter 5. Reducing the transient time of the receiving transducer enables the US receiver system to decode high data rate signals emitted from the US VSC transmitter. An US receiver was presented using a similar architecture to the VSC transmitter to achieve the same transient compensation. The proposed receiver is capable of collapsing the resonance within the receiving transducer sharply but at the expense of losing received signal gain. It was found that the driver output impedance allows the balance between the strength of transient compensation and receiver sensory output magnitude to be adjusted. The simulation results illustrated the controlled transducer dynamic can be captured and held on the *switching line (sw)* transient, demonstrating chattering dynamics around the *switching line*. Chatter is a typical characteristic of a discrete VSC system. The chattering magnitude is primarily limited by the sampling rate, as illustrated through a series of simulated phase diagrams in both Chapters 4 and 5.

As a feasibility study, the proposed transient compensation system was applied to a 1.75 kHz transducer system and presented in Chapter 6. This test bench was used to investigate the practicalities of implementation of a transmitting and receiving system. It was observed that a simple microprocessor with analogue feedback branches was sufficient to establish an output response with reduced transient duration. Nevertheless, the delays generated in both analogue and digital subsystems are critical to control system capacity.

In the discrete VSC system, a fast switching speed is necessary to constrain the motion of the system dynamic to closely follow the *sw* transient [109]. Investigation through the hardware platform indicated that to achieve a fast switching rate, required not just a high-sampling frequency, but also high precision representation of the quantised error signal. The error velocity estimation used in the *sw* computation is obtained through subtracting two consecutive samples. The amount of change between two samples is limited by the resolution of the Analogue-to-Digital Converter (ADC). The greater the number of significant bits the ADC possesses, the higher the resolution of the velocity measure. However, varying the sampling rate

will lead to different consequences that affect the precision of the switching control. A high-sampling frequency may result in the reduction of the bit change between two samples, which yields in a limited dynamic range in the estimated velocity signal. Sampling at a low frequency can provide larger variation between samples but will slow down the switching speed. A high sampling frequency is necessary to avoid delay in switching between the two feedbacks. Therefore, the dynamic range of the error velocity signal can be expanded by choosing an ADC with high resolution so that the difference between two error samples can be represented by a greater number of significant bits.

Two remaining problems have been identified, associated with the capacity of the ADC. One is that the noise in the ADC can corrupt the computed velocity signal causing it to leap around in the phase plane. If it leaps cross the boundary of the defined regions, the feedback will be switched over at the wrong time. The other is when an ADC with large word length is used; the conversion times tend to be slower.

Finally, in order to achieve the required transient response, the transducer VSC system demands very high instantaneous power as it applies dynamical compensation. Figure 7-1 is a set of simulation results to compare the instantaneous power of the VSC strategy and linear drive. The gain factors for both types of driver amplifiers are listed in table 7-1, where $A_{non-VSC}$ is the gain of standard linear *inverting amplifier* and A_{VSC} and B_{VSC} are the negative and positive gains of VSC drive. Noticeably, the result also shows that the VSC driver consumes little power when the phase difference is small. Nevertheless, the VSC driver output power experiences a sharp transient dynamic with the peak value almost 7 times higher than that of linear driver output power when a phase change is required.

A_{VSC}	B_{VSC}	$A_{non-VSC}$
100	100	15

Table 7-1: Driver gain values used for power consumptions comparison

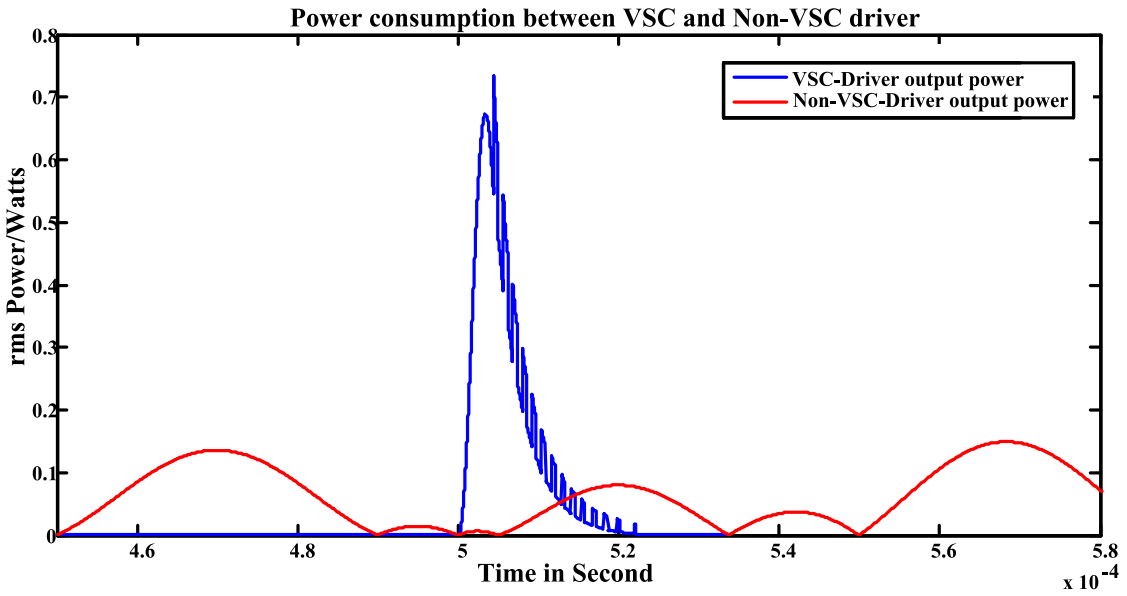

Figure 7-1: Instantaneous power comparison between VSC and non-VSC driver

7.2. Further Work

The following aspects represent the anticipated further research required to increase US communication system capacity.

7.2.1. Real Transducer Validation

The highest priority is to investigate the full performance of the designed VSC transient compensation prototype system with real transducers. This experiment demands a pair of transient compensation systems for transmitting and receiving transducer respectively. The constructed prototype platform has demonstrated a transducer circuit model resonating at an audible frequency can be effectively compensated using the VSC approach. Therefore, the platform hardware will be upgraded to operate at the US transducer resonant frequency of 40 kHz. The circuit models will be replaced with real US *piezoelectric* transducers. The open-loop tests conducted in Section 3.1 should be repeated to experimentally determine transducer intrinsic frequency and to confirm the narrow bandwidth properties of the transducers. However, an effective gain control strategy must be implemented before the closed-loop test to strictly prevent sound emission beyond the safety level.

7.2.2. Application Specific Transient Compensation System

The VSC-based transient compensation approach investigated in this research delivers a controlled transducer dynamic response. This distinct feature can then provide faster symbol transmission for US communication systems, more precise ranging using pulse measurement and better Doppler analysis for sodar systems surveyed in Chapter 2. Each of those application areas has potential for future work.

The natural next step is to customise the proposed compensation system into Application Specific Integrated Circuits (ASICs) for the control of typical US transducers. Because the compensator prototype demonstrated in Chapter 6 uses a mixed signal representation, the customised chip can retain the same structure. Programmable logic can be used to calculate the *switching line* equation. High speed Field Effect Transistor (FET) amplifiers realise the functions of signal conditioning and dual branch driver configuration as shown in Section 6.1. A fast sampling ADC is required for higher frequency transducer applications, but the resolution of Analogue-to-Digital conversion is entirely dependent on the required precision of transient control. As discussed in Chapter 6, although it is helpful to have a greater number of significant bits to represent the digitised error signal, to expand the dynamic range of the error velocity, it may also increase cost and slow down the conversion. This may involve a series of optimisations to the existing electronic compensation system hardware based on the particular requirements from real applications. Implementing the transient compensator using either entirely digital or analogue system is another potential research area to explore. A full analogue version will replace the digital approximation used in this design with analogue differentiator circuit that can, in theory, provide better resolution on velocity axis. However, it may introduce other problems. For instance, the dynamic range of the signal is really sensitive to noise. Also, an analogue differentiator that is physically band-limited is no longer a differentiator at high frequency. An entire digital implementation has the flexibility that it can be adapted when parameters in the system need to be varied. The limitations of discrete VSC system are due to the need for sufficient samples to represent the error transient convergence discussed in Subsection 6.3.4.

7.2.3. Maximum Capacity of the BPSK US Communication Systems

The information capacity of a communication system using phase modulation can be measured through symbol (or bit) transmission rate. For the BPSK modulation explored in this project, one symbol carries one bit of information. Increasing the number of amplitudes or and phases that can be resolved during each symbol period allows higher order modulation schemes to be used, such as QPSK or QAM, and more information transmitted during each symbol period. Chapter 3 showed the BPSK symbol of a 40 kHz US system is subject to a delayed phase switching. The simulated and measured results indicated the system barely managed to achieve a bit rate of 2 kbps. Results in Chapters 4 and 5 respectively illustrated the VSC transducer system is capable of producing much faster phase switching, in a period as short as half a carrier cycle. This suggests for a VSC-based US data communication system, the symbol rate is limited to half the carrier frequency. Accordingly, a theoretical maximum BPSK capacity (assuming a 40 kHz US transducer) can be speculated to be 20 kbps. A longer period would be required to resolve the phase when using a higher order modulation scheme and the trade-off between symbol period and information per symbol may or may not yield higher capacity. For instance, if it took one carrier period to resolve the phase to a quadrant then the use of QPSK would not increase capacity. The number of resolvable amplitudes depends upon the signal-to-noise ratio at the receiver output and will be affected by the environment and interference by other US sources.

The precision of US range measurements is also limited by the bandwidth. For 40 kHz transducer system, increasing the bandwidth by a factor of ten should yield a similar increase in range estimation precision i.e. typical range error could be reduced from 17 cm to 17 mm.

7.2.4. Increasing Capacity of Acoustic Rain Sodar

Paulson *et al.* [110] has proposed research based on the evaluated results to develop a novel vertical pointing Doppler sodar, operating at 40 kHz. This design intends to create an acoustic equivalence to the commercial radio meteorological sensing equipment e.g. the Metek Micro Rain Radar. However, the proposed system will model and estimate the Drop Size Distribution

(DSD) of rain based on measured drop density at a lower altitudes (about 60 m above the ground) using much lower frequencies than the Metek microwave system. An US system would be considerably cheaper and would not require an annual spectrum license to operate. Continuous Wave (CW) transmission is chosen to yield greater received signal strength against noise at receiver. This ensures the transmission power is under safe thresholds. Advanced signal processing techniques can be applied to compensate echo signal energy losses resulting from atmospheric perturbations and various meteorological effects e.g. Doppler shift, target range and radial wind velocity may be derived through the measured acoustic echo. The increased US transducer bandwidth demonstrated by this project, is necessary to make an US equivalent to the microwave system. So far simulations and experimentations for the construction of proposed instrument are in progress.

Chapter 8.

Concluding Remarks

The intrinsic contributions presented in the research works are:

- In this research, the Variable Structure Control was first proposed in the applications of ultrasonic (US) transducer transient control.

- The feasibility study through simulation and system physical implementation has firmly validated the effectiveness of the proposed approach.

- The improved system performance redefines the maximum data transmission and ranging capacity at much higher level. This enables other US systems based on similar operating principle to perform with an increased capacity.

- The hardware system implementation of the transient compensation approach is a useful problem-solving demonstration to the other dynamic processes with similar phenomenon which needs be removed.

Chapter 9.

Appendices

The following sections are the corresponding appendices used in Chapters 3, 4, 5 and 6. Sections 9.1 and 9.2 are the detailed derivation of transducer transfer functions. Section 9.3 is a set of simulation results of Variable Structure Control (VSC) transmitter using alternative parameters. Section 9.4 contains the captures of ARM microprocessor peripheral clock frequency settings. Sections 9.5 and 9.6 are the schematics of constructed physical transducer systems.

9.1. Transmitting Transducer Transfer Function Derivation

Subsections 9.1 and 9.2 derive the transfer functions of transducer circuit models used in Chapters 3, 4 and 5. The first two subsections deal with the transfer functions of the original circuit models used to characterise transmitting and receiving transducers. The transfer function of the circuit models used in transducer VSC compensation are deduced in subsections 9.2.1 and 9.2.2. The circuit model as shown in figure 4-3 is configured for transfer function analysis in this subsection.

9.1.1. Transmitting Transducer Transfer Function regarding V_{rd} as Output

The output impedance of previous drive stage is modelled by a series resistor, R_{m4}. The following derivations to the transducer circuit model transfer functions will use the parameters listed in table 9-1.

C_p	L_s	C_s	R_s
2100 pF	110 mH	130 pF	600 Ω
R_{m1}	R_{m2}	R_{m4}	R_d
10 Ω	10 Ω	10 kΩ	600 Ω

Table 9-1: Parameters used in receiving transducer transfer function derivation

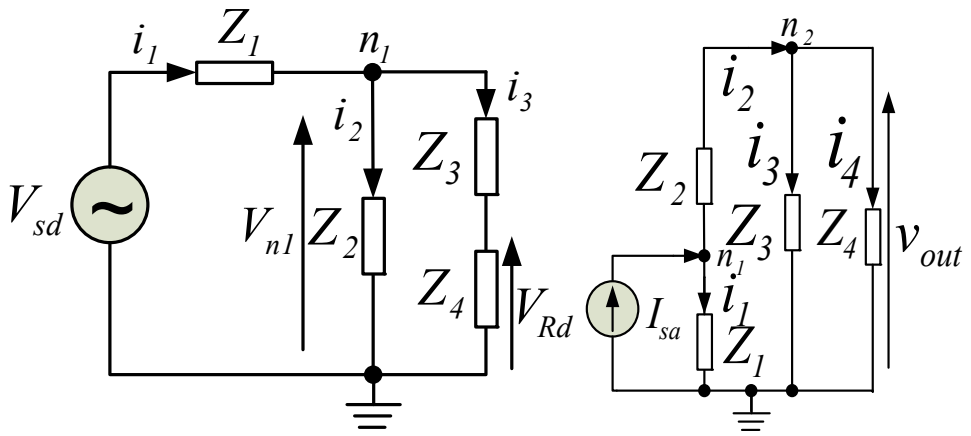

Figure 9-1: a) Transmitting transducer model b) Receiving transducer model

Figure 9-1 a) is the equivalence of figure 4-3 with generalised impedances as defined in (9.1-9.4).

$$Z_1 = R_{m4}, Z_2 = \frac{1}{C_p s}. \tag{9.1,9.2}$$

$$Z_3 = R_d, Z_4 = L_s s + \frac{1}{C_s s} + R_s + R_d. \tag{9.3,9.4}$$

According to nodal potential method, the node equation is given in (9.5)

$$i_2 + i_3 - i_1 = 0. \tag{9.5}$$

Where branch currents i_1, i_2 and i_3, can be found in (9.6-9.8)

$$i_1 = \frac{V_{sd} - V_{n1}}{Z_1}, i_2 = \frac{V_{n1}}{Z_2}, i_3 = \frac{V_{n1}}{Z_3 + Z_4}. \tag{9.6,9.7 ,9.8}$$

It can be seen that V_{n1} is a portion of the drive signal V_{sd}.

$$V_{n1} = \frac{V_{sd}(C_s L_s s^2 + (R_d C_s + R_s C_s)s + 1)}{C_p R_{m4} L_s C_s s^3 + (C_p R_{m4} R_d C_s + L_s C_s + C_p R_{m4} R_s C_s)s^2 + (C_p R_{m4} + C_s R_{m4} + R_d C_s + R_s C_s)s + 1}. \tag{9.9}$$

The Voltage on R_d refers to the nodal voltage V_{n1}.

$$V_{Rd} = \frac{V_{n1} R_d}{(L_s s + \frac{1}{C_s s} + R_s + R_d)}. \tag{9.10}$$

Substituting (9.9) into (9.10) yields the expression that V_{Rd} is related to V_{sd}:

$$V_{Rd} = \frac{V_{sd} R_d C_s s}{C_p R_{m4} L_s C_s s^3 + (L_s C_s + C_p R_{m4} R_d C_s + C_p R_{m4} R_s C_s)s^2 + (C_p R_{m4} + C_s R_{m4} + R_d C_s + R_s C_s)s + 1}. \tag{9.11}$$

Dividing both sides of (9.11) by V_{sd} and bringing all circuit component values into (9.12), the transfer characteristic of transmitting transducer G_{aTx} is obtained as expressed in (9.13).

$$G_{aTx} = \frac{V_{Rd}}{V_{sd}}. \tag{9.12}$$

$$\mathrm{G}_{aTx} = \frac{.7800000000e14\ s}{3003\ s^3 + .1433822000\ e^{11}s^2 + .4050000000e^{15}s + .1000000000\ e^{22}}. \tag{9.13}$$

9.1.2. Receiving Transducer Transfer Function regarding V_{out} as Output

The transfer function of receiving transducer circuit model is deduced in the following part. The generalisation of circuit elements refers to figure 9-1 b).

$$Z_1 = R_d, Z_2 = L_s s + \frac{1}{C_s s} + R_s. \tag{9.14,9.15}$$

$$Z_3 = \frac{1}{C_p s}, Z_4 = R_{m3}. \tag{9.16,9.17}$$

According to nodal potential method, the node equation is given in (9.18, 9.19).

$$\begin{cases} i_1 + i_2 = 0, \\ i_2 - i_3 - i_4 = 0. \end{cases} \tag{9.18,9.19}$$

Where V_{n1} and V_{n2} are the corresponding voltages on nodes 1 and 2. The branch currents in (9.18, 9.19) are defined as (9.20-9.23)

$$i_1 = \frac{V_{n1}}{Z_1 - I_{sa}}, i_2 = \frac{V_{n1} - V_{n2}}{Z_2}. \tag{9.20,9.21}$$

$$i_3 = \frac{V_{n2}}{Z_3}, i_4 = \frac{V_{n2}}{Z_4}. \tag{9.22,9.23}$$

Solving simultaneous equations (9.18, 9.19) gives:

$$V_{n1} = \frac{600 I_{sa}(.1263000000e^{-6}s + .3549000000e^{-18}s^3 + 1 + .1690218400e^{-10}s^2)}{.1690382200e^{-10}s^2 + .2043000000e^{-6}s + .3549000000e^{-18}s^3 + 1}. \tag{9.24}$$

$$V_{n2} = \frac{39 I_{sa} s}{.1774500000e^{-10}s^3 + .8451911000e^{-3}s^2 + 50000000. + 10.21500000s}. \tag{9.25}$$

Dividing both sides of (9.25) by V_{sd} and bringing all circuit component values into (9.26), the transfer characteristic of transmitting transducer G_{aRx} is obtained as expressed in (9.27).

$$G_{aRx} = \frac{V_{n2}}{I_{sa}}. \tag{9.26}$$

$$\mathrm{G}_{aRx} = \frac{39s}{(.1774500000e^{-10}s^3 + .8451911000e^{-3}s^2 + 50000000. + 10.21500000s)}. \tag{9.27}$$

9.2. VSC Transducer System Transfer Function Derivation

Transducer transfer function for VSC transmitter and receiver will be deduced in the following two subsections.

9.2.1. Transmitting Transducer Transfer Function regarding V_e as Output

The VSC transient control system relies on the transducer output feedback signal to form system error. This could be realised either using transducer acoustic output (modelled by V_{rd}) or an electrical equivalence V_e.

The US transmitting transducer circuit model with impedance matching branch is shown as in figure 9-2 a). The input of transducer system, V_{sd}, is the voltage across the entire transducer branch including R_{m4}. The selected output in the configuration shown in figure 4-8 is the difference between the currents in transducer branch and added branch. This output can be obtained by the voltage difference between measurement resistors R_{m2} and R_{m1}.

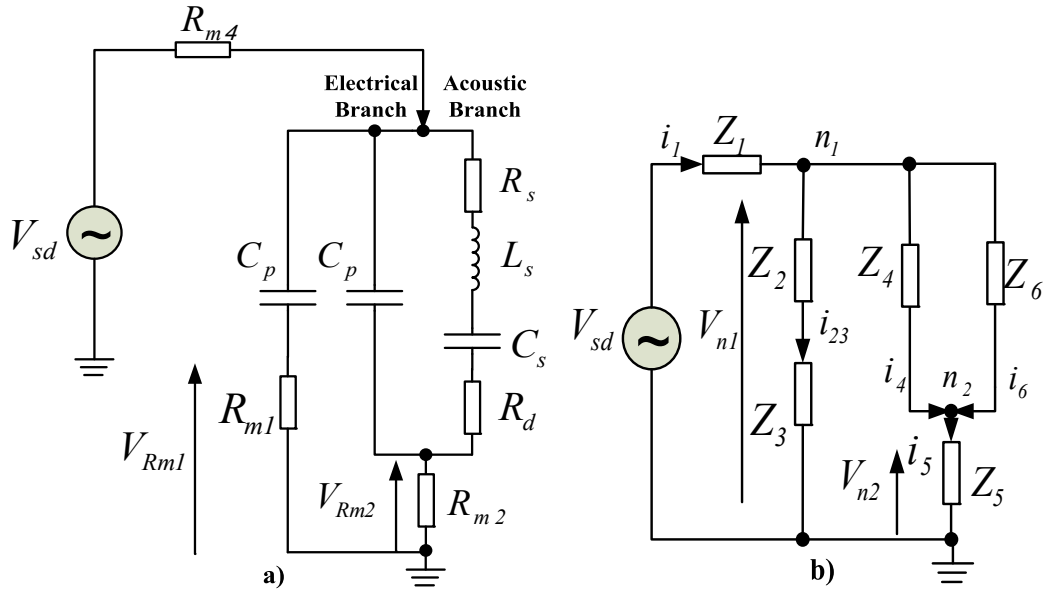

Figure 9-2: a) Transducer circuit model with impedance matching branch b) Equivalent circuit network of transducer circuit model

Figure 9-2 b) presents a generalised form of the transducer module by replacing each element in the network with their corresponding impedances as defined by the following equations (9.28-9.33):

$$Z_1 = R_{m4}, Z_2 = \frac{1}{C_p s}, Z_3 = R_{m1}. \quad (9.28,9.29,9.30)$$

$$Z_4 = \frac{1}{C_p s}, Z_5 = R_{m2},\ Z_6 = L_s s + \frac{1}{C_s s} + R_s + R_d. \quad (9.31,9.32,9.33)$$

Branch currents are expressed using related nodal voltages as follows:

$$i_1 = \frac{V_{sd} - V_{n1}}{Z_1}, i_2 = \frac{V_{n1}}{Z_2 + Z_3}. \quad (9.34,9.35)$$

$$i_4 = \frac{V_{n1} - V_{n2}}{Z_4}, i_5 = \frac{V_{n1} - V_{n2}}{Z_5}, i_6 = \frac{V_{n2}}{Z_6}. \quad (9.36,9.37,9.38)$$

Applying KCL to nodes 1 and 2, we have:

$$\begin{cases} i_1 - i_{23} - i_4 - i_5 = 0, \\ i_4 + i_5 - i_6 = 0. \end{cases} \quad (9.39)$$

Bringing the branch currents into above equations and re-arranging:

$$V_{n1} = \frac{2380952381.+50.s)*V_{sd}*(3003.s^3+.2043000000e^{16}s+.1430382200e^{12}s^2+.1000000000e^{23})}{(3153150.s^4+.1573401310e15s^3+.3427123405e^{21}s^2+.1567380952e^{26}s+.2380952381e^{32})}. \quad (9.40)$$

$$V_{n2} = \frac{V_{sd}s(150150.s^3+.7151911000e^{13}*s^2+.1021500000e18s+.5309523810e^{24})}{(3153150.s^4+.1573401310e15s^3+.3427123405e^{21}s^2+.1567380952e^{26}s+.2380952381e^{32})}. \quad (9.41)$$

Applying potential division rule, the voltage across Z_3 can be solved through equation below:

$$V_3 = \frac{V_{n1}Z_3}{Z_2+Z_3}. \quad (9.42)$$

The difference between V_{n2} and V_3 is the system feedback output expressed in (9.43) and is a function of drive voltage V_{sd}.

$$V_e = V_{n2} - V_3. \quad (9.43)$$

$$V_e = \frac{.6190476200e21V_{sd}s}{(63063.s^4+.3146802620e^{13}s^3+.6854246810e^{19}s^2+.3134761904e^{24}s+.4761904762e^{30})}. \quad (9.44)$$

Dividing both sides of (9.19) with V_{sd} the right hand side becomes:

$$G_{eTx} = \frac{V_e}{V_{sd}}. \quad (9.45)$$

$$G_{eTx} = \frac{.6190476200e21s}{(63063.s^4+.3146802620e^{13}s^3+.6854246810e^{19}s^2+.3134761904e^{24}s+.4761904762e^{30})}. \quad (9.46)$$

9.2.2. Receiving Transducer Transfer Function regarding V_e as Output

The receiving transducer circuit model configured as shown in figure 9-3 contains has two inputs.

One is the acoustic input modelled as current source; the other is control input providing different feedback signals and also modelled as voltage source.

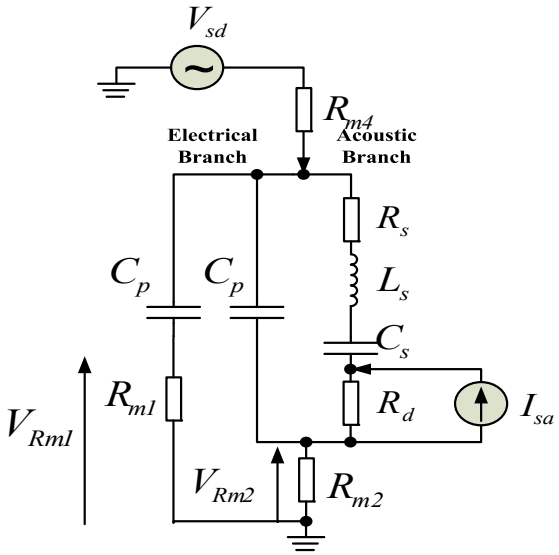

Figure 9-3: Receiving transducer circuit model configuration

Referring to *Thevenin's* Theorem, the acoustic input terminal is open when the *Thevenin* equivalent circuit regarding V_{sd} as input is analysed. When simplifying the transducer model circuit driven by acoustic signal, the electrical drive port should be grounded. The *Thevenin* equivalent circuit with V_{sd} as input has been analysed in Section 9.1.3. This section will consider the network with current input. The circuit configuration is given in figure 9-4. The difference between the currents flowing through R_{m1} and R_{m2} is regarded as the output of VSC-based US receiver.

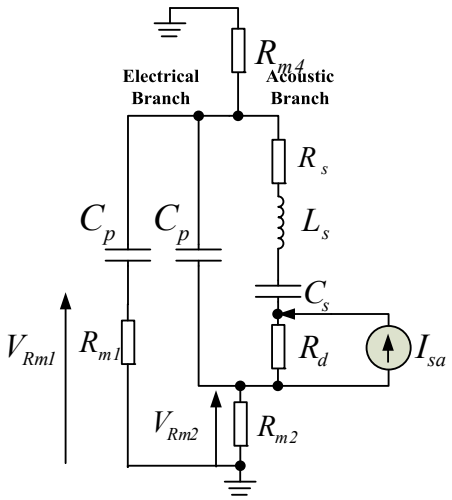

Figure 9-4: Equivalent circuit with R_{m4} grounded

Figure 9-5 a) is the circuit representing the situation when the transducer is in receiving mode and

not driven by the electrical signal.

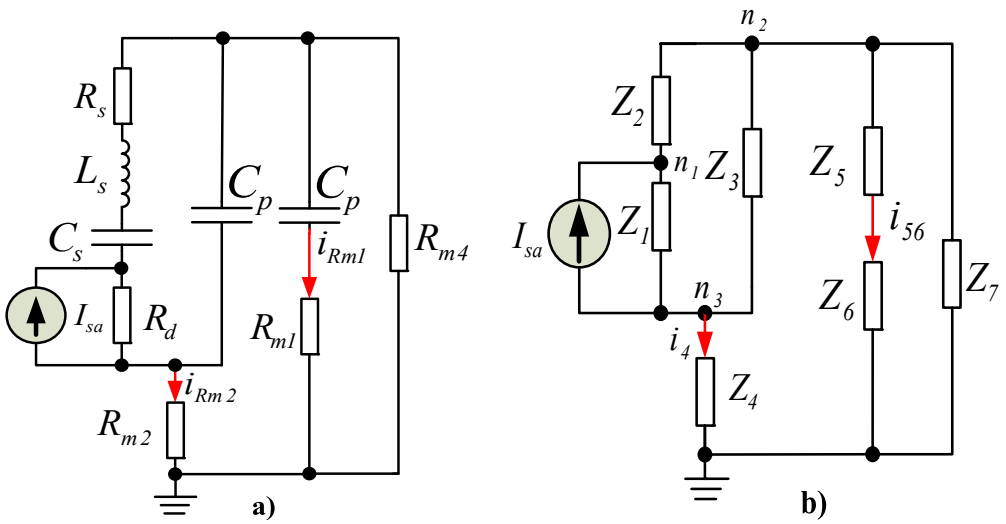

Figure 9-5: a) Network considering i_{sa} as input b) Generalised impedance network

Each element in figure 9-5 b) is replaced with (9.47-9.48).

$$Z_1 = R_d, Z_2 = L_s s + \frac{1}{C_s s} + R_s. \quad (9.47,9.48)$$

$$Z_3 = \frac{1}{C_p s}, Z_4 = R_{m3}. \quad (9.49,9.50)$$

$$Z_5 = \frac{1}{C_p s}, Z_6 = R_{m1}, Z_7 = R_{m4}. \quad (9.51,9.52,9.53)$$

Branch currents are expressed as in (9.54-9.59):

$$i_1 = \frac{V_{n1}-V_{n3}}{Z_1} - I_{sa}, i_2 = \frac{V_{n1}-V_{n3}}{Z_2}, i_3 = \frac{V_{n1}-V_{n3}}{Z_3}. \quad (9.54,9.55,9.56)$$

$$i_4 = \frac{V_{n3}}{Z_4}, i_{56} = \frac{V_{n2}}{Z_5+Z_6}, i_7 = \frac{V_{n2}}{Z_7}. \quad (9.57,9.58,9.59)$$

Substituting circuit component values and rearranging:

$$V_{n1} = \frac{600(300450150.s^4+.1431648509e^{17}s^3+.4662406905e^{21}s^2+.1034428571e^{28}s+.2380952381e^{32})I_{sa}}{(300450150.s^4+.1431812391e^{17}s^3+.5449693405e^{21}s^2+.1036316667e^{28}s+.2380952381e^{32})}. \quad (9.60)$$

$$V_{n2} = \frac{.7800000000\, e^{19} I_{sa}\, s(2380952381+50.*s)}{300450150.s^4+.1431812391e^{17}s^3+.5449693405e^{21}s^2+.1036316667e^{28}s+.2380952381e^{32}}. \quad (9.61)$$

$$V_{n3} = \frac{-.7800000000\, e16\, I_{sa}\, s(50050\, s+2380952381)}{300450150\, s^4+.1431812391e^{17}s^3+.5449693405e^{21}s^2+.1036316667e^{28}s+.2380952381e^{32}}. \quad (9.62)$$

Applying potential division method, the voltage on R_{m1} can be determined in (9.63).

$$V_6 = \frac{V_{n2} Z_6}{Z_5 + Z_6}. \tag{9.63}$$

The network voltage output, V_e ,can be found by the subtraction between V_{n3} and V_6:

$$V_e = V_{n3} - V_6. \tag{9.64}$$

$$V_e = \frac{-(.1560780000 e^{20} I_{sa}\, s^2 + .3714285714\, e^{24}\, I_{sa}\, s)}{6009003\, s^4 + .2863624782 e^{15} s^3 + .1089938681 e^{20} s^2 + .2072633334\, e^{26} s + .4761904762 e^{30}}. \tag{9.65}$$

A trans-impedance transfer function, G_I, can be derived via dividing (9.65) I_{sa}

$$G_I = \frac{V_e}{I_{sa}}. \tag{9.66}$$

$$G_I = \frac{-(.1560780000 e^{20}\, s^2 + .3714285714\, e^{24}\, s)}{6009003\, s^4 + .2863624782\, 10^{15} s^3 + .1089938681\, 10^{20} s^2 + .2072633334\, 10^{26} s + .476190476210^{30}}. \tag{9.67}$$

The transfer function of receiving transducer circuit model,G_C, can be derived based on the same principle introduced in Subsection 9.1.3 and is expressed as in (9.69).

$$G_C = \frac{V_e}{V_{sd}}. \tag{9.68}$$

$$G_C = \frac{.619047620010^{20}\ s}{6009003\, s^4 + .2863624782\, 10^{15} s^3 + .1089938681\, 10^{20} s^2 + .2072633334\, 10^{26} s + .4761904762\, 10^{30}}. \tag{9.69}$$

9.3. ARM processor peripheral clock frequency configurations

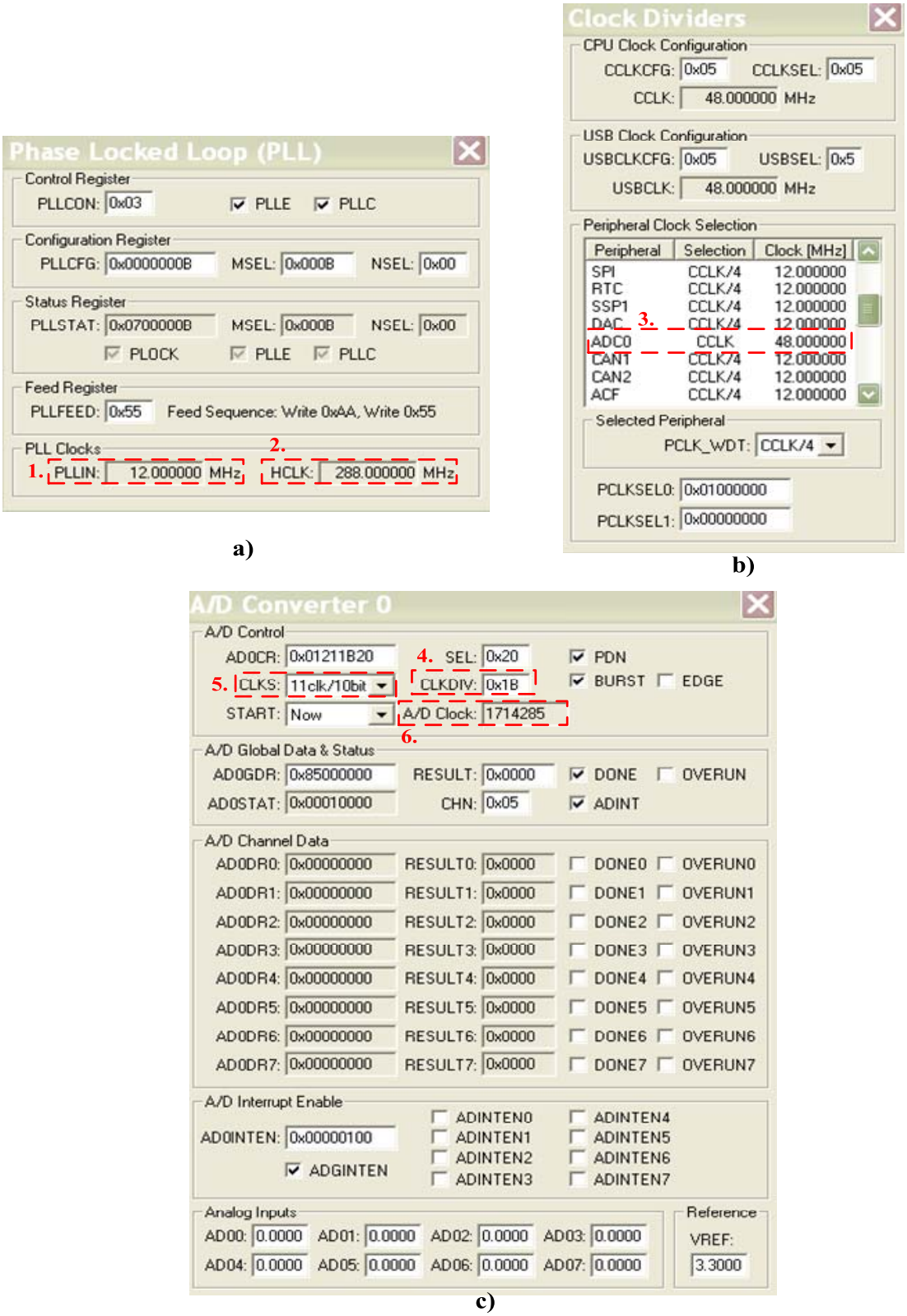

Figure 9-6: Keil complier system parameter configurations a) 1. PLL frequency 2. PLL output frequency b) 3. ADC peripheral frequency c) 4. Frequency divider value of ADC clock 5. Bits conversion selection 6. ADC clock frequency

9.4. Schematic of the Ultrasonic Transducer System

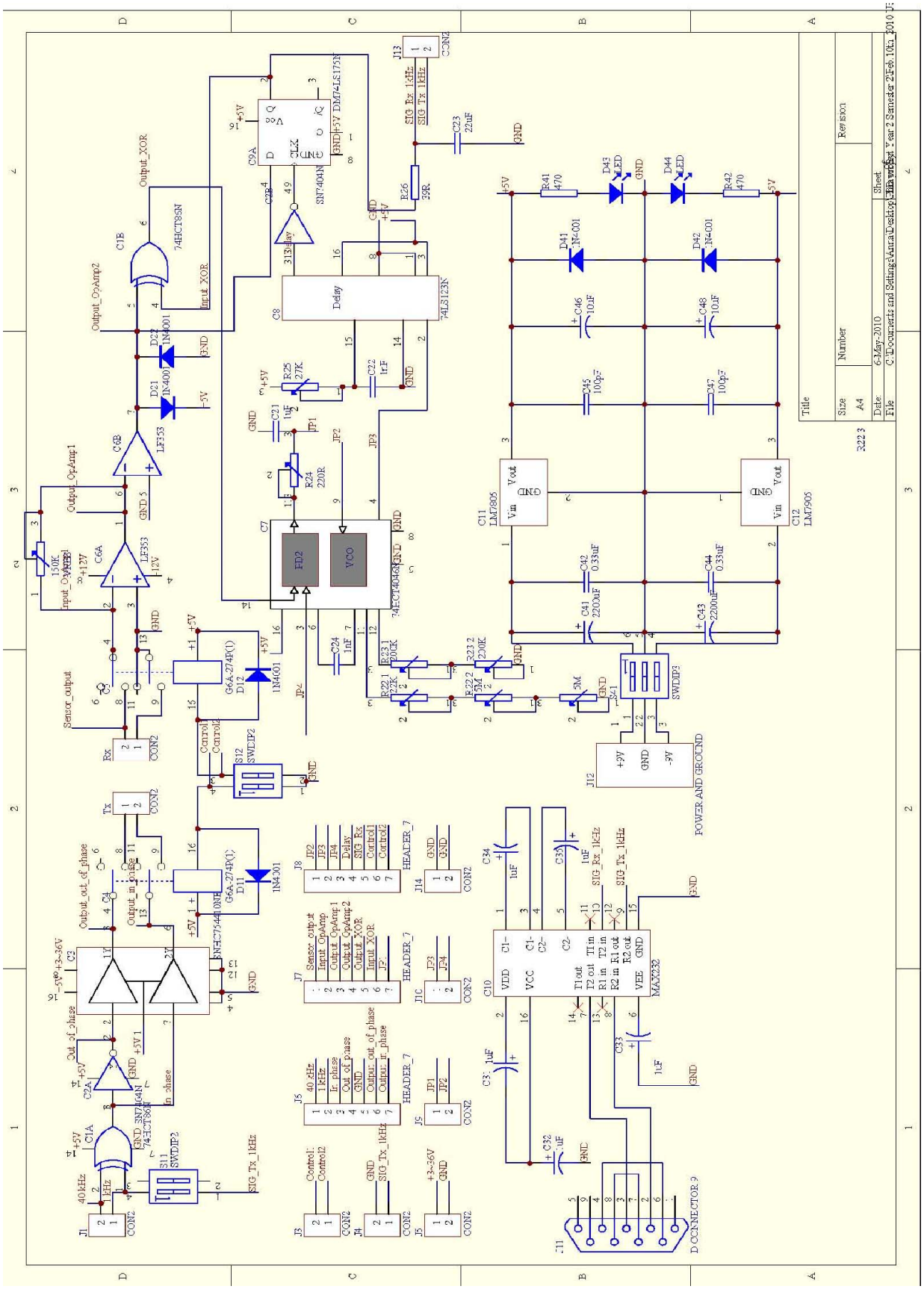

Figure 9-7: Phase modulation-based US communication system schematic

9.5. Schematic of VSC Ultrasonic Transmitting System

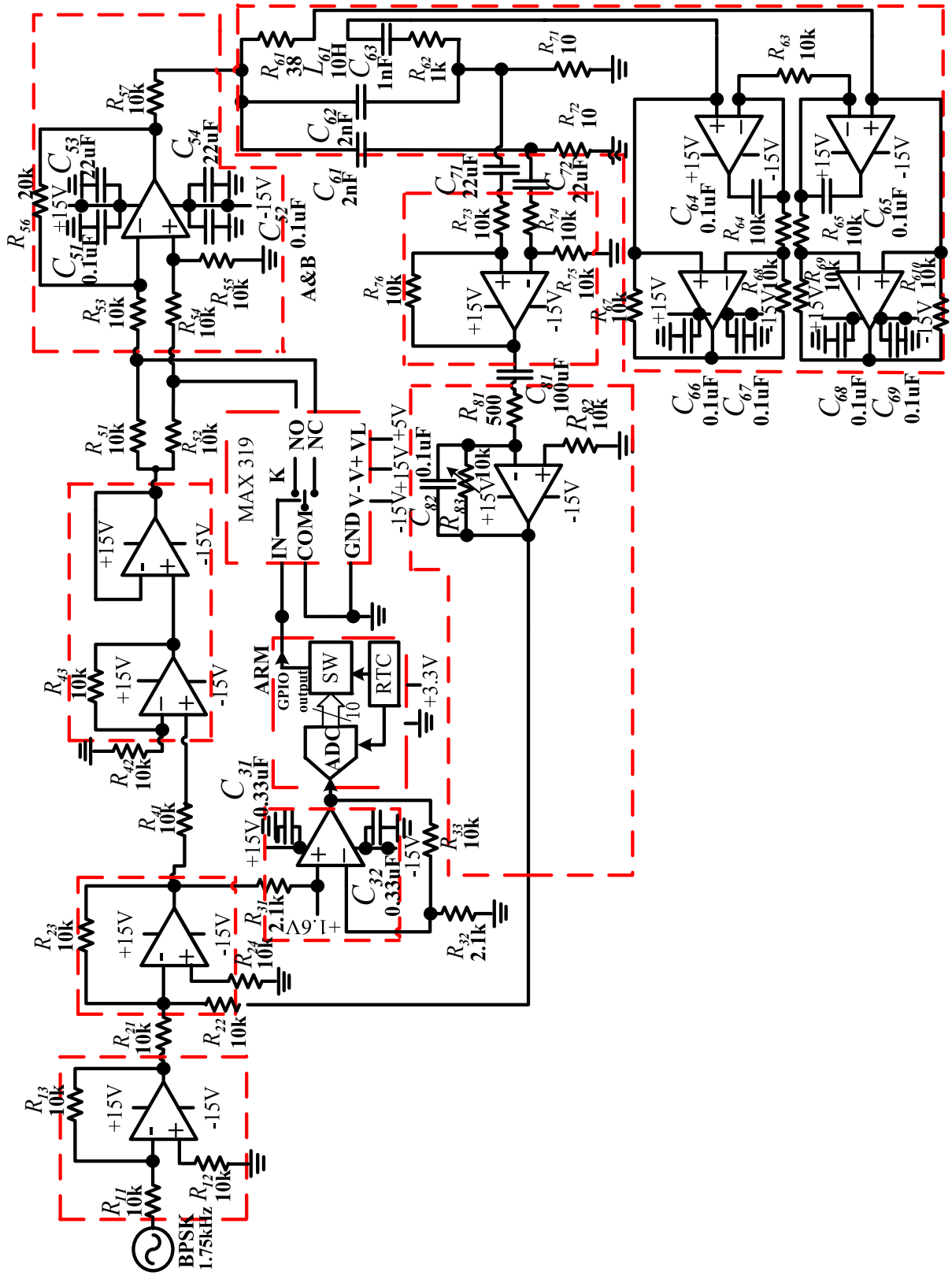

Figure 9-8: Transducer transient compensation system prototype schematic

9.6. List of Publications

[1] S. Ma, A. J. Wilkinson, K. S. Paulson, "A phase modulation-based ultrasonic communication system using Variable Structure Control," presented at the 12th IEEE International Conference on Communication Technology, 2010, pp. 857-860. (**Awarded as best student paper**)

[2] S. Ma, A. J. Wilkinson, K. S. Paulson, "Performance analysis of a phase modulation-based ultrasonic receiver using Variable Structure Control," presented at the 13th IEEE International Conference on Communication Technology, 2011, pp. 776-779.

References

[1] R. Eckhoff and O. Thomassen, "Possible sources of ignition of potential explosive gas atmospheres on offshore process installations," *Journal of Loss Prevention in the Process Industries,* **vol. 7**, pp. 281-294, 1994.

[2] A. Gachagan*, et al.*, "Characterization of air-coupled transducers," *IEEE Transactions on Ultrasonics, Ferroelectrics and Frequency Control,* **vol. 43**, pp. 678-689, 1996.

[3] A. A. Vives, *Piezoelectric Transducers and Applications* 2nd ed. New York: Springer, 2008.

[4] G. Gautschi, *Piezoelectric sensorics*, 1st ed. New York: Springer-Verlag Berlin HeidelBerg, 2002.

[5] L. Lynnworth and J. Bradshaw, "Magnetostriction transducers of acoustic emission, impulse, vibration, and noise analysis," *Materials Research and Standards,* **vol. 11**, pp. 33-35, 1971.

[6] S. Holm, "Airborne ultrasound data communications: the core of an indoor positioning system," presented at the IEEE Ultrasonics Symposium, 2005, pp. 1801-1804.

[7] S. Holm*, et al.*, "Indoors data communications using airborne ultrasound," presented at the IEEE International Conference on Acoustics, Speech, and Signal Processing Proceedings. (ICASSP '05), 2005, pp. 957-960

[8] C. Li*, et al.*, "Short-range ultrasonic digital communications in air," *IEEE Transactions on Ultrasonics, Ferroelectrics and Frequency Control,* **vol. 55**, pp. 908-918, 2008.

[9] R. Adler*, et al.*, "An ultrasonic remote control for home receivers," *IRE Transactions on Broadcast and Television Receivers,* **vol. BTR-3**, pp. 8-13, 1957.

[10] P. Alfke*, et al.*, "An approach to ultrasonic remote control systems," *IEEE Transactions on Broadcast and Television Receivers,* **vol. BTR-19**, pp. 256-262, 1973.

[11] R. Noffke and R. Kramer, "TV remote control analog to digital ultrasonic receivers,"

IEEE Transactions on Broadcast and Television Receiver, **vol. BTR-15**, pp. 261-266, 1969.

[12] L. F. Brown and D. L. Carlson, "Ultrasound transducer models for piezoelectric polymer films," *IEEE Transactions on Ultrasonics, Ferroelectrics and Frequency Control,* **vol. 36**, pp. 313-318, 1989.

[13] J. L. Ealo*, et al.*, "Broadband EMFi-based transducers for ultrasonic air applications," *IEEE Transactions on Ultrasonics, Ferroelectrics and Frequency Control,* **vol. 55**, pp. 919-929, 2008.

[14] M. I. Haller and B. T. Khuri-Yakub, "A surface micromachined electrostatic ultrasonic air transducer," *IEEE Transactions on Ultrasonics, Ferroelectrics and Frequency Control,* **vol. 43**, pp. 1-6, 1996.

[15] L. Chuan*, et al.*, "Short-range ultrasonic communications in air using quadrature modulation," *IEEE Transactions on Ultrasonics, Ferroelectrics and Frequency Control,* **vol. 56**, pp. 2060-2072, 2009.

[16] H. Yu-Ting*, et al.*, "Applications of time-gating method to improve the measurement accuracy of antenna radiation inside an anechoic chamber," presented at the IEEE Antennas and Propagation Society International Symposium, 2003, pp. 794-797.

[17] T. O. Pedersen and N. Karlsson, "Time-of-Flight Ultrasonic Displacement Sensors," *The measurement, instrumentation, and sensors handbook,* p. 92, 1999.

[18] K. Conrad and L. Lynnworth, "Fundamentals of Ultrasonic Flow Meters," *American School of Gas Measurement Technology,* **vol. 1**, pp. 52-61, 2002.

[19] A. Carullo and M. Parvis, "An ultrasonic sensor for distance measurement in automotive applications," *IEEE Sensors Journal,* **vol. 1**, pp. 143-147, 2001.

[20] A. Gillespie*, et al.*, "A new ultrasonic technique for the measurement of liquid level," *Ultrasonics,* **vol. 20**, pp. 13-17, 1982.

[21] S. Hünerbein and H. Richner, "A doppler sodar case study of top-down convection and convective dissipation of stratus," *J. Atmos. Oceanic Technol,* **vol. 19**, pp. 1170–1180,

September 26 2002.

[22] J. J. Leonard and H. F. Durrant-Whyte, "Mobile robot localization by tracking geometric beacons," *IEEE Transactions on Robotics and Automation,* **vol. 7**, pp. 376-382, 1991.

[23] D. Marioli*, et al.*, "Digital time-of-flight measurement for ultrasonic sensors," *IEEE Transactions on Instrumentation and Measurement,* **vol. 41**, pp. 93-97, 1992.

[24] H. Eriksson*, et al.*, "A robust correlation receiver for distance estimation," *IEEE Transactions on Ultrasonics, Ferroelectrics and Frequency Control,* **vol. 41**, pp. 596-603, 1994.

[25] P. Horsky*, et al.*, "Acoustic Distance Measurement System Having Cross Talk Immunity," US Patent 20,110,267,924, Nov. 3rd 2011.

[26] L. Angrisani*, et al.*, "Ultrasonic-Based Distance Measurement Through Discrete Extended Kalman Filter," in *Kalman Filter Recent Advances and Applications* V. M. M. a. A. Pigazo, 1st ed. Italy: InTech, 2009, pp. 269-296.

[27] L. Angrisani*, et al.*, "A measurement method based on Kalman filtering for ultrasonic time-of-flight estimation," *IEEE Transactions on Instrumentation and Measurement,* **vol. 55**, pp. 442-448, 2006.

[28] L. Angrisani*, et al.*, "Ultrasonic time-of-flight estimation through unscented Kalman filter," *IEEE Transactions on Instrumentation and Measurement* **vol. 55**, pp. 1077-1084, 2006.

[29] X. Wang and Z. Tang, "A novel method for digital ultrasonic time-of-flight measurement," *Review of Scientific Instruments,* **vol. 81**, pp. 105-112, 2010.

[30] J. Hightower and G. Borriello, "Location sensing techniques," *IEEE Computer,* **vol. 34**, pp. 57-66, 2001.

[31] S. Huang*, et al.*, "A high accuracy ultrasonic distance measurement system using binary frequency shift-keyed signal and phase detection," *Review of Scientific Instruments,* **vol. 73**, pp. 3671-3677, 2002.

[32] F. E. Gueuning, *et al.*, "Accurate distance measurement by an autonomous ultrasonic system combining time-of-flight and phase-shift methods," *IEEE Transactions on Instrumentation and Measurement,* **vol. 46**, pp. 1236-1240, 1997.

[33] F. Figueroa and E. Barbieri, "An ultrasonic ranging system for structural vibration measurements," *IEEE Transactions on Instrumentation and Measurement,* **vol. 40**, pp. 764-769, 1991.

[34] E. Ersagun and A. O. Yilmaz, "Ultrasonic communication in wireless sensor networks," presented at the IEEE 16th Signal Processing, Communication and Applications Conference, 2008, pp. 1-4.

[35] K. W. Kolodziej, *Local positioning systems: LBS applications and services*, 1st ed. Boca raton, Florida: CRC press, 2006.

[36] Z. Xiang, *et al.*, "A wireless LAN-based indoor positioning technology," *IBM Journal of Research and Development,* **vol. 48**, pp. 617-626, 2004.

[37] D. Mountain and J. Raper, "Positioning techniques for location-based services (LBS): characteristics and limitations of proposed solutions," presented at the Aslib Conference, 2001, pp. 404-412.

[38] K. Barrow, (2009, 2009), *Most Hospital Patients Unable to Identify Their Physicians* [Report]. Available: <http://www.nytimes.com/2009/01/30/health/30patients.html>

[39] E. Ersagun and A. Yilmaz, "Ultrasonic communication in wireless sensor networks," 2008, pp. 1-4.

[40] J. Juell and H. Westerberg, "An ultrasonic telemetric system for automatic positioning of individual fish used to track Atlantic salmon (Salmo salar L.) in a sea cage," *Aquacultural Engineering,* **vol. 12**, pp. 1-18, 1993.

[41] S. L. Wang FB, Ren FY 2005, *Self-Localization systems and algorithms for wireless sensor networks*. *Journal of Software 16(5),* 857−868.

[42] T. S. Rappaport, *Wireless Communications: Principles and Practice*, 2nd ed. New Jersey: Prentice Hall, 2002.

[43] M. P. Wylie and J. Holtzman, "The non-line of sight problem in mobile location estimation," presented at the The 5th IEEE International Conference on Universal Personal Communications, 1996, pp. 827 - 831.

[44] F. van der Heijden*, et al.*, "Acoustic time-of-flight measurements in a reflective room," presented at the Proceeding16th IMEKO World Congress Proceeding, 2003, pp. 1176-1180.

[45] M. Alloulah and M. Hazas, "An efficient CDMA core for indoor acoustic position sensing," presented at the International Conference on Indoor Positioning and Indoor Navigation (IPIN), 2010, pp. 1-5.

[46] H. Koyuncu and S. H. Yang, "A survey of indoor positioning and object locating systems," *International Journal of Computer Science and Network Security,* **vol. 10**, pp. 121-128, 2010.

[47] G. Borriello and J. Hightower, "A survey and taxonomy of location systems for ubiquitous computing," *IEEE Computer,* **vol. 34**, pp. 407–416, 2001.

[48] H. Liu*, et al.*, "Survey of wireless indoor positioning techniques and systems," *IEEE Transactions on Systems, Man, and Cybernetics, Part C: Applications and Reviews,* **vol. 37**, pp. 1067-1080, 2007.

[49] A. Küpper, *Location-based services*: Wiley Online Library, 2005.

[50] R. Mautz, "Overview of current indoor positioning systems," *Geodesy and Cartography,* **vol. 35**, pp. 18-22, 2009.

[51] Y. Gu*, et al.*, "A survey of indoor positioning systems for wireless personal networks," *IEEE Communications Surveys & Tutorials,* **vol. 11**, pp. 13-32, 2009.

[52] H. Kim, Park, Y. , "Preliminary study of time-of-flight measurement for 3D position sensing system based on acoustic signals " presented at the International Conference on Control, Automation and Systems(ICCAS), 2002.

[53] F. G. a. F. Gunnarsson, "Positioning using time-difference of arrival measurements," presented at the IEEE International Conference on Acoustics, Speech, and Signal

Processing Acoustics, Speech, and Signal Processing Proceedings. (ICASSP '03), 2003, pp. 553-556.

[54] J. Schiller, *Mobile Communication*, 2nd ed. Essex: Pearson Education Limited, 2003.

[55] N. B. Priyantha*, et al.*, "The cricket location-support system," presented at the The 6th ACM International Conference on Mobile Computing and Networking (MOBICOM), 2000, pp. 32-43.

[56] N. B. Priyantha*, et al.*, "The cricket location-support system," 2000, pp. 32-43.

[57] A. M. R. Ward, "Sensor Driven Computing," doctoral dissertation, University of Cambridge, Cambridge, 1998.

[58] Y. Fukuju*, et al.*, "DOLPHIN: an autonomous indoor positioning system in ubiquitous computing environment," presented at the IEEE Workshop on Software Technologies for Future Embedded Systems, 2003, pp. 53-56.

[59] P. Rong and M. L. Sichitiu, "Angle of arrival localization for wireless sensor networks," presented at the The 3rd Annual IEEE Communications Society on Sensor and Ad Hoc Communications and Networks (SECON '06), 2006, pp. 374-382.

[60] N. B. Priyantha*, et al.*, "The cricket compass for context-aware mobile applications," presented at the The 7th Annual ACM/IEEE International Conference on Mobile Computing and Networking Proceedings (Mobicom 2001), 2001, pp. 1-14.

[61] F. Tong*, et al.*, "A high precision ultrasonic docking system used for automatic guided vehicle," *Sensors and Actuators A: Physical,* **vol. 118**, pp. 183-189, 2005.

[62] M. Hazas and A. Hopper, "Broadband ultrasonic location systems for improved indoor positioning," *IEEE Transactions on Mobile Computing,* pp. 536-547, 2006.

[63] M. Hazas and A. Hopper, "Broadband ultrasonic location systems for improved indoor positioning," *IEEE Transactions on Mobile Computing,* **vol. 5**, pp. 536-547, 2006.

[64] H. Hashizume*, et al.*, "Fast and Accurate Positioning Technique Using Ultrasonic Phase Accordance Method," presented at the IEEE Region 10 International Technical

Conference, 2005, pp. 1-6.

[65] T. Sato*, et al.*, "Extended phase accordance method: A real-time and accurate technique for estimating position and velocity of moving objects using ultrasonic communication," *Sensors & Transducers Journal,* **vol. 9**, pp. 56–70, 2010.

[66] J. N. Ash and L. C. Potter, "Sensor Network Localization via Received Signal Strength Measurements with Directional Antennas," presented at the the 42nd Annual Allerton Conference on Communication, Control, and Computing, 2004, pp. 1861-1870.

[67] A. S. Krishnakumar and P. Krishnan, "The theory and practice of signal strength-based location estimation," presented at the IEEE International Conference on Collaborative Computing: Networking, Applications and Worksharing, 2005, p. 10.

[68] B. Li*, et al.*, "Indoor positioning techniques based on wireless LAN," presented at the The 1st IEEE International Conference on Wireless Broadband and Ultras Wideband Communications, 2006, pp. 13-16.

[69] D. Wratt, "Air pollution meteorology and acoustic sounding," presented at the The 5th International Society for Acoustic Remote Sensing of the Atmosphere and Oceans and Associated Techniques Symposium (ISARS) Proceedings, 1990, pp. 443–452.

[70] B. Gera and S. Singal, "Sodar in air pollution meteorology," *Atmospheric Environment. Part A. General Topics,* **vol. 24**, pp. 2003-2009, 1990.

[71] W. D. Neff and R. L. Coulter, "Acoustic remote sensing," in *Probing the atmospheric boundary layer*, D. H. Lenschow, 1st ed.: American Meteorological Society, 1986, pp. 201-239.

[72] E. H. Brown and F. F. Hall Jr, "Advances in atmospheric acoustics," *Reviews of Geophysics,* **vol. 16**, pp. 47-110, 1978.

[73] R. Sivacoumar*, et al.*, "Air pollution modeling for an industrial complex and model performance evaluation," *Environmental Pollution,* **vol. 111**, pp. 471-477, 2001.

[74] S. Bradley*, et al.*, "SODAR measurements of wing vortex strength and position," *Journal of Atmospheric and Oceanic Technology,* **vol. 24**, pp. 141-155, 2007.

[75] T. Gerz*, et al.*, "Commercial aircraft wake vortices," *Progress in Aerospace Sciences,* **vol. 38**, pp. 181-208, 2002.

[76] S. Bradley and T. Webb, "Use of an ultrasonic sodar to sense raindrop size distributions," *Journal of Atmospheric and Oceanic Technology,* **vol. 19**, pp. 1203-1207, 2002.

[77] S. Bradley, "Acoustic radar studies of rain microphysics," *Journal of Atmospheric and Oceanic Technology,* **vol. 14**, pp. 547-553, 1997.

[78] S. V. Shamanaev, "Acoustic sounding of raindrop size distribution," *Journal of Atmospheric and Oceanic Technology,* **vol. 20**, pp. 152-158, 2003.

[79] R. Pinkel and J. Smith, "Repeat-sequence coding for improved precision of Doppler sonar and sodar," *Journal of Atmospheric and Oceanic Technology,* **vol. 9**, pp. 149-163, 1992.

[80] A. Ballato, "Resonance in piezoelectric vibrators," *Proceedings of the IEEE,* **vol. 58**, pp. 149-151, 1970.

[81] A. S. W. Alan V. Oppenheim, S. Hamid, *Signals and Systems* 2nd ed. Essex: Pearson Education, 1996.

[82] H. F. Olson, *Dynamical analogies*, 2nd ed. New Jersey: Princeton, N.J., Van Nostrand, 1958.

[83] J. Bentley, "Ultrasonic measurement systems," in *Principles of measurement systems*, 4th ed. Essex: Pearson Education, 2005, pp. 343-385.

[84] W. Mason, "Electrical and mechanical analogies," *Bell System Technical Journal,* **vol. 20**, pp. 404-14, 1941.

[85] D. Ma, *Fundamentals of Modern Acoustics Theory*: Scentific House, 2006.

[86] C. H. Park, "On the circuit model of piezoceramics," *Journal of Intelligent Material Systems and Structures,* **vol. 12**, pp. 515-522, 2001.

[87] M. Guan and W. Liao, "On the equivalent circuit models of piezoelectric ceramics," *Ferroelectrics,* **vol. 386**, pp. 77-87, 2009.

[88] N. C. contributors, *Air Transmission Ultrasonic Sensor*. Available: http://product.icI14.comlPDFITIT40-16PR40-16P.pdf

[89] L. Svilainis and G. Motiejūnas, "Power amplifier for ultrasonic transducer excitation," *Ultragarsas (Ultrasound). Kaunas: Technologija,* **vol. 58**, pp. 30-36, 2006.

[90] B. H. Kamens, "Capacitive charge pump driver circuit for piezoelectric alarm," US Patent 5,493,543, Feb. 20th 1996.

[91] F. J. Pompei and J. C. Olsson, "Power efficient capacitive load driving device," US Patent 6,661,285 B1, Dec. 9 2003.

[92] D. S. McCarren, "BPSK demodulator with D type flip/flop," US Patent 4,744,094, May 10th 1988.

[93] M. Contributors, (2011, Dec.4th), *Demo: Phase Locked Loop*. Available: http://www.mathworks.com/matlabcentral/fx_files/14868/1/content/html/plldemo.html

[94] M. Jafaripanah*, et al.*, "Application of analog adaptive filters for dynamic sensor compensation," *IEEE Transactions on Instrumentation and Measurement,* **vol. 54**, pp. 245-251, 2005.

[95] J. Piskorowski and T. Barcinski, "Dynamic compensation of load cell response: A time-varying approach," *Mechanical Systems and Signal Processing,* **vol. 22**, pp. 1694-1704, 2008.

[96] Y. Xiyun and L. Xinran, "Integral variable structure fuzzy adaptive control for variable speed wind power system," presented at the International Conference on Logistics Systems and Intelligent Management, 2010, pp. 1247-1250.

[97] G. Joos*, et al.*, "Closed-loop state variable control of dynamic voltage restorers with fast compensation characteristics," presented at the IEEE 39th Industry Applications Conference, 2004, pp. 2252-2258

[98] V. Utkin, "Variable structure systems with sliding modes," *IEEE Transactions on Automatic Control,* **vol. 22**, pp. 212-222, 1977.

[99] A. Parvinmehr*, et al.*, "Design of discrete-time adaptive optimal variable structure controllers," presented at the The 5th International Conference on Control Theory Proceedings, 1992, pp. 199-199.

[100] H. Marquez, *Nonlinear control systems: analysis and design*, 1st ed. New Jersey: Wiley-Interscience Hoboken, 2003.

[101] S. Ma*, et al.*, "A phase modulation-based ultrasonic communication system using Variable Structure Control," presented at the 12th IEEE International Conference on Communication Technology (ICCT), 2010, pp. 857-860.

[102] K. D. Young*, et al.*, "A control engineer's guide to sliding mode control," *IEEE Transactions on Control Systems Technology,* **vol. 7**, pp. 328-342, 1999.

[103] A. Antoniou and K. Naidu, "Modeling of a gyrator circuit," *IEEE Transactions on Circuit Theory,* **vol. 20**, pp. 533-540, 1973.

[104] G. Flachenecker and A. Sauerborn, "Gyrator-type equivalent circuit for piezoelectric transducers," presented at the IEEE Ultrasonics Symposium Proceedings, 1988, pp. 403-406

[105] J. Edwin C. Jones, Harry W. Hale, "Active filters," in *Standard Handbook for Electrical Engineers* H. W. F. Beaty, Donald G., 5th ed. New York: McGraw-Hill 2004, pp. 10.43-10.56.

[106] U. Kumar*, et al.*, "Analytical Study of Inductor Simulation Circuits," *Active and Passive Electronic Components,* **vol. 13**, pp. 211-227, 1989.

[107] M. Contributors, "MAX317/MAX318/MAX319 Precision, CMOS Analog Switches," 1st ed, 1994.

[108] N. Semiconductors, "LPC23xx user manual," 1st ed. Netherlands: NXP Semiconductors, 2011.

[109] A. Zinober, "An introduction to sliding mode variable structure control," *Variable Structure and Lyapunov Control,* pp. 1-22, 1994.

[110] K. S. Paulson. 2011, A SODAR Rain Disdrometer. unpublished.